MULTIPLE TIME SCALE DYNAMICS OF CHEMICAL OSCILLATORS

A Dissertation

Presented to the Faculty of the Graduate School

of Cornell University

in Partial Fulfillment of the Requirements for the Degree of

Doctor of Philosophy

by

Christopher J. Scheper

August 2011

MULTIPLE TIME SCALE DYNAMICS OF CHEMICAL OSCILLATORS

Christopher J. Scheper, Ph.D.

Cornell University 2011

In this thesis, we analyze the multiple time scale dynamics of two chemical oscillator models: the "autocatalator," a three-dimensional, two time scale vector field that satisfies the the law of mass action for an autocatalytic chemical reaction, and a four-dimensional model of the Belousov-Zhabotinskii (BZ) reaction taking place in a continuous-flow stirred tank called Model D. For each model, we concentrate on the multiple time scale nature of the reaction and the mechanisms that create mixed-mode oscillations (MMOs) in the models.

In the analysis of the autocatalator, we show that a Poincaré return map simultaneously exhibits full rank and rank deficient behavior for different regions of phase space. Canard trajectories that follow a two-dimensional repelling slow manifold separate these regions. This allows us to compute a one-dimensional induced map from approximations of the return maps. The bifurcations of these induced maps are used to characterize the bifurcations of the mixed mode oscillations of the full three-dimensional system.

We also analyze a four-dimensional model of the BZ reaction called Model D, first proposed by L. Györgyi and R. Field. Using experimental parameters as model parameters, we investigate the dynamic mechanisms shaping behavior in the low flow rate and high flow rate complexity regimes. We use geometric singular perturbation theory to interpret the behavior of the system in regions of phase space with a clear separation of time scales. At low flow rates, we show that a dynamic Hopf bifurcation is responsible for the creation of the small am-

plitude oscillations of the MMOs. At high flow rates, the dynamics are shaped by interactions with an equilibrium point. Finally, we show that Model D is capable of replicating experimentally observed behaviors.

BIOGRAPHICAL SKETCH

Chris Scheper was born in Cincinnati, Ohio in 1982. After moving to southeast Indiana during his elementary school years, he attended East Central High School and pursued degrees in mathematics and applied physics at Purdue University. After the conferral of his baccalaureate degrees in 2005, he continued his studies in the Center for Applied Mathematics at Cornell University. At Cornell, Chris studied applied dynamical systems with an interest in multiple time scale dynamics under the guidance of Dr. John Guckenheimer. After receiving his master's degree in Applied Mathematics in October 2008, Chris completed his doctoral work during the summer of 2011. He looks forward to extending his mathematical breadth while working for the consulting and analytics firm Opera Solutions, LLC in San Diego, California.

To Jennifer, for her endless support.

ACKNOWLEDGEMENTS

First and foremost, I would like to thank my advisor John Guckenheimer for his guidance, support, and incredible patience. His ability to read and edit rough drafts in a timely fashion is nothing short of astonishing. I also extend my sincerest gratitude to the other two members of my committee, Dr. Richard Rand and Dr. John Smillie.

I owe many thanks to my parents, Mark and Terri Scheper, without whose love and support I would not be writing this thesis today. They encouraged me to be independent and confident, and to never be discouraged at failure. I am also blessed to have been bestowed such wonderful siblings, Jason and Laura, who are a source of support and inspiration. The immense fun and laughter we have at family gatherings make up for the decreasing rate at which they occur.

The friends and colleagues I have met at Cornell have made Ithaca a great home over the past six years. I cherish the time spent with many CAMsters, including the *vagabundus* Lauren Childs, the alpha male Erik Sherwood, the grammatical perfectionist Mateo Restrepo, and finally with Stephen Moseley and Stefan Ragnarsson, with whom I've spent many hours in Teagle downstairs preparing for spring runs on Libe Slope. I also owe many thanks to the Sunday (and sometimes Monday) football crew, which includes Meredith Graham, whose life trajectory I have had the privilege to share over the last nine years, Peter Luthy, whose ambivalence toward Tom Brady makes him my favorite Patriots fan, and Greg Muller, whose constant source of nerdiness and sarcastic wit often left us laughing to the point of tears. I also wish to thank Jason Anema, Margaret Bruns, Diarmuid Calahane, Michael Cortez, Denise Dawson, Matt Holden, Marisa Hughes, Paul Hurtado, Sarah Iams, Kristine Jones, Nathan Karst, Ben and Helen Lundell, Christian Kühn, Andrew Mar-

shall, Philipp Meerkamp, Tim Novikoff, Rocío Ruelas, Anthony Sabelli, Peter Samuelson, David Slater, Anael Verdugo, and Gwyn Whieldon for their friendship and lively discussion and debate.

Finally, I owe the most thanks to my wife Jennifer, who is a constant source of support. Her presence in my life has brought me unimaginable happiness. This work is dedicated to her, and serves as a reminder that through dedication, hard work, and persistence through tough times, together we can overcome seemingly insurmountable obstacles.

TABLE OF CONTENTS

LIST OF TABLES

LIST OF FIGURES

CHAPTER 1

INTRODUCTION

1.1 Oscillations in chemical systems

Although the first liquid-phase chemical oscillator was discovered by Bray in 1921 [17], the modern study of chemical oscillators is based on the pioneering work of B. P. Belousov [9] in 1951, who discovered oscillations in the concentrations of the catalyst in a Cerium-ion catalyzed oxidation of citric acid by bromate ions. A. M. Zhabotinskii [125] perfected Belousov's recipe and introduced the reaction to Western scientists in 1968. The family of metal-ion catalyzed oxidations of organic substrates by bromate ions is now referred to as the Belousov-Zhabotinskii reaction, or BZ reaction. The BZ reaction displays a stunning variety of behavior, including including steady state, simple periodic orbits, mixed-mode oscillations (MMOs), alternating periodic and aperiodic sequences, excitability, invariant tori, bistability, intermittency, crisis bifurcations, and several well-known routes-to-chaos. The details of the reactions are highly complex, involving up to 80–100 reactions and 20–30 intermediate chemical species. As experimental techniques improved, so did the understanding of the chemical mechanisms generating the oscillations. However, the exact details of the reaction are unknown, and even today are the subject of much debate.

Increasingly, chemists looked to dynamical systems theory to understand the mechanisms generating complex oscillations. Dynamical systems theory played a key role in the history of the BZ reaction, particularly in the mathematical analysis of models of the reaction, and the application of dynamical systems techniques to experimental time series. The latter was pivotal in establishing the

existence of chaos in the reaction at low flow rates. The possibility of chaos in the reaction had two important consequences: i) carefully designed experiments investigating aperiodic time series were performed, and ii) many mathematical models were proposed to describe the reaction. In particular, comprehensive models of the entire reaction were proposed, as well as simple toy models designed to investigate whether chaos can occur in equations derived from the law of mass action.

Individual reactions in chemical systems often occur at rates that differ by several orders of magnitude. As a result, there is a natural slow-fast structure of the reaction models. One of the most effective tools in analyzing the slow and fast reactions is geometric singular perturbation theory (GSPT) [29, 67]. We begin the next section with a short introduction to the main concepts of GSPT.

1.2 Multiple time scale dynamical systems

1.2.1 Basic framework

Slow-fast differential equations with two time scales can be written in the form

$$\begin{aligned} x' &= f(x, y, \lambda, \epsilon), \\ y' &= \epsilon g(x, y, \lambda, \epsilon), \end{aligned} \tag{1.1}$$

where $' = \frac{d}{dt}$, $x \in \mathbb{R}^n$ are the fast variables, $y \in \mathbb{R}^m$ are the slow variables, $\lambda \in \mathbb{R}^p$ are the system parameters, and $0 < \epsilon \ll 1$ is a small positive parameter that represents the ratio of the time scales of the two variables [29, 67]. The functions $f : \mathbb{R}^{n+m+p+1} \to \mathbb{R}^n$ and $g : \mathbb{R}^{n+m+p+1} \to \mathbb{R}^m$ are assumed to be as smooth

as necessary, usually C^∞. Equation (1.1) is a singularly perturbed differential equation and the ϵ in (1.1) indicates that y changes much more slowly than x. The time variable t is said to be fast time; this equation is sometimes called the fast system.

Time can be rescaled by $\tau = \epsilon t$ and the system can be reformulated as

$$\begin{aligned} \epsilon \dot{x} &= f(x, y, \lambda, \epsilon), \\ \dot{y} &= g(x, y, \lambda, \epsilon), \end{aligned} \tag{1.2}$$

where $\dot{} = \frac{d}{d\tau}$. The time variable τ is said to be slow time; equation (1.2) is called the slow system.

For $\epsilon \neq 0$, equations (1.1) and (1.2) are equivalent; trajectories of the two equations in phase space are identical, although time is rescaled. The analysis of slow-fast systems begins by taking the singular limit of these two systems as $\epsilon \to 0$. From (1.1), we obtain the differential equation

$$\begin{aligned} x' &= f(x, y, \lambda, 0), \\ y' &= 0. \end{aligned} \tag{1.3}$$

Equation (1.3) treats y as an m-dimensional parameter, and is called the fast subsystem or layer equation. Similarly, if we let $\epsilon \to 0$ in (1.2), we obtain the differential-algebraic equation

$$\begin{aligned} 0 &= f(x, y, \lambda, 0), \\ \dot{y} &= g(x, y, \lambda, 0). \end{aligned} \tag{1.4}$$

Equation (1.4) is called the slow flow or reduced equation. The reduced equation is constrained to the manifold given by the algebraic constraint in equation (1.4).

Trajectories of singularly perturbed differential equations of the form (1.1) or (1.2) are characterized by the alternation of fast and slow epochs, with each time scale dominating particular regions of phase space. As $\epsilon \to 0$, a fast epoch of a trajectory converges to trajectories of the fast subsystem (1.3), and slow epochs converge to trajectories of the slow subsystem (1.4). Trajectories of the full system track invariant objects of the fast subsystem. Bifurcations of the fast subsystem can create, destroy and change the stability of these objects. This may cause rapid switching between attractors in the full system. The goal of GSPT is to use the lower dimensional fast subsystem and slow flow in order to understand the dynamics of the full system.

The algebraic constraint in (1.4) defines the critical manifold

$$\mathcal{S} = \{(x, y) \in \mathbb{R}^n \times \mathbb{R}^m \mid f(x, y, \lambda, 0) = 0\}, \tag{1.5}$$

which is also the set of the equilibria of the layer equation. Let $M \subset \mathcal{S}$, then M is called normally hyperbolic if $(D_x f)(p)$ is nonsingular for all $p \in M \subset \mathbb{R}^n \times \mathbb{R}^m$. Equivalently, M is normally hyperbolic if all equilibria of the system $\dot{x} = f(x, y, \lambda, 0)$ are hyperbolic at $(x, y) \in M$. M is called attracting if all eigenvalues of $(D_x f)(p)$ have negative real part for $p \in M$. Likewise, M is called repelling if all eigenvalues have positive real part. M is said to be of saddle-type if it is neither attracting nor repelling.

Where the critical manifold is normally hyperbolic, Fenichel's theorems [29] guarantee that the dynamics of the full system behave similarly to the fast and slow subsystems. The following two theorems are basic to the subject of slow-fast systems.

Theorem 1 (Fenichel's first theorem [29, 67])**.** *Let $M_0 \subset \mathcal{S}$ be compact and normally hyperbolic, and let $f, g \in C^r$ for $r < \infty$. Then there exist $\epsilon > 0$ and a manifold M_ϵ within*

$O(\epsilon)$ distance of S, which is locally invariant under the flow (1.1)–(1.2), diffeomorphic to M_0, and is C^r for any $r < \infty$. M_ϵ is also normally hyperbolic and has the same stability as M_0. We call M_ϵ a slow manifold.

Normally hyperbolic subsets of the critical manifold also have associated stable and unstable manifolds,

$$W^s_{\text{loc}}(M_0) = \bigcup_{p \in M_0} W^s_{\text{loc}}(p), \text{ and } W^u_{\text{loc}}(M_0) = \bigcup_{p \in M_0} W^u_{\text{loc}}(p),$$

where $W^s_{\text{loc}}(p)$ and $W^u_{\text{loc}}(p)$ are the local stable and unstable manifolds of p as a hyperbolic equilibrium of the layer equation, respectively. Fenchel's second theorem guarantees their persistence in the full system as well.

Theorem 2 (Fenichel's second theorem [29, 67])**.** *Let M_0, M_ϵ be as above. Then for $\epsilon > 0$ sufficiently small, there exist stable and unstable manifolds $W^s(M_\epsilon)$ and $W^u(M_\epsilon)$ within $O(\epsilon)$ distance from and diffeomorphic to $W^s(M_0)$ and $W^u(M_0)$, respectively. $W^s(M_\epsilon)$ and $W^u(M_\epsilon)$ are also locally invariant under the flow (1.1)–(1.2).*

The loss of normal hyperbolicity near a fold allows the attracting and repelling slow manifolds to intersect. The dynamics near a fold have been described using several methods, including asymptotic techniques [27, 82], nonstandard analysis [12, 13] and the blow-up technique [].

1.2.2 Mixed-mode oscillations

Mixed-mode oscillations (MMOs) are trajectories concatenated from large amplitude oscillations and small amplitude oscillations with a distinct difference between the amplitude of small and large oscillations. MMOs are denoted by *signatures* $\{L_i^{s_i}\}_{i \geq 1}$, where each pair $L_i^{s_i}$ denotes a segment of the MMO com-

prised of L_i large oscillations followed by s_i small oscillations. MMOs have been observed in diverse physical, biological, neuronal, and chemical systems [18, 34, 106, 10, 125]. Tables in the review [25] present an extensive list of systems exhibiting MMOs.

MMOs usually occur as a trajectory transitions from a slow epoch (approximated by the reduced system) to a fast epoch (approximated by the layer equation). For $\epsilon > 0$ sufficiently small, this occurs when a trajectory passes through a region where the critical manifold loses normal hyperbolicity. Normal hyperbolicity can fail in several ways, including:

- a fold of the critical manifold, i.e. $\det(D_x f(x,y)|_S) = 0$ [109],
- a Hopf bifurcation of the layer equation, [83, 84],
- intersecting sheets of the critical manifold [69],
- and the critical manifold is asymptotically tangent to a fast direction at infinity [80, 49].

In this thesis, we focus on MMOs and complex dynamics related to the first two types of loss of normal hyperbolicity: a Hopf bifurcation that occurs near a fold in the critical manifold, called a singular Hopf bifurcation, and a Hopf bifurcation of the layer equation, called a dynamic Hopf bifurcation. We briefly outline these two phenomena.

1.2.3 Singular Hopf bifurcation

In many slow-fast systems, interesting phenomena are generated near folds of the critical manifold. As indicated above, folds occur when $\det(D_x f(x,y)|_S) = 0$.

Since equilibria of (1.1) occur at $f(x, y, \lambda, \epsilon) = 0$, these generically lie on normally hyperbolic sheets of the critical manifold. However, in generic one-parameter families of slow-fast systems of the form (1.1), equilibria may cross a fold curve of a critical manifold. A singular Hopf bifurcation is characterized by a Hopf bifurcation that occurs at a distance $O(\epsilon)$ away from the fold of $\mathcal{S}$ for any ϵ sufficiently small.

One of the simplest examples of singular Hopf bifurcation is the van der Pol oscillator with constant forcing. The slow-fast vector field is given by

$$\begin{aligned} \epsilon \dot{x} &= y - x^3/3 - x, \\ \dot{y} &= \lambda - x. \end{aligned} \tag{1.6}$$

The critical manifold is given by the cubic $y = x^3/3 - x$. For all $\epsilon > 0$, a Hopf bifurcation occurs on the fold of $\mathcal{S}$ at $(x, y) = (1, -2/3)$ as λ decreases through $\lambda = 1$. A small periodic orbit grows according to the standard square-root scaling [47] as λ is decreased. For sufficiently small values of ϵ and $\lambda \approx 1 - O(\epsilon)$, the amplitude of the periodic orbit grows exponentially over an exponentially small parameter interval. This phenomenon is called canard explosion. In canard explosion, periodic orbits grow in amplitude by following the repelling branch of the critical manifold. Any orbit that follows a repelling manifold for $O(1)$ slow time is called a canard. Canards that reach the upper critical point are called maximal canards. In general, any canard that lies in the intersection of an attracting and repelling slow manifold is a maximal canard. After the canard explosion, the system exhibits relaxation oscillations.

Guckenheimer [43] outlines three dynamical features that are associated with singular Hopf bifurcation in general slow-fast dynamical systems.

1. The Hopf bifurcation occurs at a distance that is $O(\epsilon)$ from the fold curve.

2. The periodic orbits emanating from the Hopf bifurcation undergo a canard explosion.
3. The attracting and repelling slow manifolds intersect transversally as a parameter is varied.

In systems with more than two dimensions, singular Hopf bifurcation is a mechanism that can generate MMOs in the presence of a global return mechanism. This occurs when the unstable manifold of the bifurcating equilibrium point intersects a repelling slow manifold. Figure 2.5 illustrates this phenomenon in the autocatalator [88], a three-dimensional vector field. For the following discussion, assume that our system is three-dimensional with two slow variables and one fast variable. Let q be an equilibrium point near a fold of a critical manifold, and fix $\epsilon > 0$ sufficiently small. Suppose that q undergoes a supercritical Hopf bifurcation. Immediately after the Hopf bifurcation, q has a one-dimensional stable manifold $W^s(q)$ and a two-dimensional unstable manifold $W^u(q)$ which is bounded by the family of stable limit cycles γ_λ. As λ increases, the Floquet multipliers of the limit cycle γ become complex, and the unstable manifold $W^u(q)$ begins to scroll around γ. As the unstable manifold grows, it develops intersections with the repelling slow manifold, allowing trajectories to leave the fold region.

Figures 2.5(a) and 2.5(c), found on page 27, show the two-dimensional unstable manifold of the equilibrium point $W^u(q)$ in green and the slow repelling manifold $\mathcal{S}^r_\epsilon$ in red for two parameter values. Figure 2.5(a) shows that $W^u(q)$ is bounded by γ and contained in the fold region. Figure 2.5(b) shows the intersection of $W^u(q)$ and $\mathcal{S}^r_\epsilon$ with a cross section. The intersection of γ with the cross section is indicated by a black cross. The turning point seen in $W^u(q)$ is a result

of $W^u(q)$ scrolling around the limit cycle γ_μ, indicating that the nontrivial Floquet multipliers of the cycle are complex. As λ increases, the diameter of $W^u(q)$ grows, becomes tangent to $\mathcal{S}^r_\epsilon$, and then intersects the repelling slow manifold transversally. After the intersection, some trajectories in $W^u(q)$ escape the fold region and execute large excursions. Figure 2.5(c) shows a subset of $W^u(q)$ that contains the transversal intersection of $W^u(q)$ and $\mathcal{S}^r_\epsilon$. The intersection can also be seen in the cross section in Figure 2.5(d). When paired with a global return mechanism, a singular Hopf bifurcation can generate MMOs.

1.2.4 Dynamic Hopf bifurcation

A dynamic Hopf bifurcation is a Hopf bifurcation of a fast subsystem (1.1) where the slow variable acts as a bifurcation parameter. This occurs when a pair of eigenvalues of $D_x f$ pass through the imaginary axis (with non-zero speed) on the critical manifold [120, 85]. Further discussion of the dynamic Hopf bifurcation, particularly in chemical systems, can be found in [25]. For this discussion, assume that $x \in \mathbb{R}^2$ are the fast variables and $y \in \mathbb{R}$ is a slow variable, and that a supercritical dynamic Hopf bifurcation takes place on a one-dimensional critical manifold l at l_H. For $\epsilon = 0$, the slow variable y is a fixed parameter. When $\epsilon > 0$, the slow variable y varies slowly and traverses the region near the Hopf bifurcation. The Hopf bifurcation partitions the critical manifold l into l_H, l_-, and l_+, where the $\pm$ indicates the signs of the real part of the eigenvalues on either side of l_H. As a result, l_- is attracting and l_+ is repelling. Trajectories passing through the dynamic Hopf region are attracted to and oscillate around l_-, and are repelled from l_+.

There are two phenomena associated with dynamic Hopf bifurcation: a "tourbillion" and delayed Hopf bifurcation. The difference between the two phenomena is related to the minimal distance of the trajectory to the critical manifold. In delayed Hopf bifurcation, a trajectory approaches the critical manifold l_- at a distance $O(1)$ from the Hopf bifurcation. The trajectory will become exponentially close to l_- due to its attraction. The layer equations undergo a Hopf bifurcation, but if (1.1) is analytic, the trajectory will remain near l_+ for $O(1)$ time. Regardless of the smoothness, the trajectory does not immediately follow the limit cycles of the fast subsystem. The delay occurs because the trajectory is exponentially close to l and must be repelled away before following the limit cycles of the layer equation. The delay is dependent on the smoothness of the system [83, 84]. In many cases, the SAOs of a delayed Hopf bifurcation are below a visible threshold, leading to a trajectory that is indistinguishable from the critical manifold.

A tourbillion occurs when a trajectory passes closely by a dynamic Hopf bifurcation and the small amplitude oscillations remain visible. The speed at which a trajectory traverses a dynamic Hopf region is governed by the slow time scale. As the separation of time scales increases, so does the time spent near the dynamic Hopf bifurcation. When the separation is weak, trajectories traverse the dynamic Hopf region faster and execute fewer SAOs. As a result, the oscillations remain above an observable threshold. For some systems, the amplitude of the SAOs remain nearly constant. For a fixed ϵ, the difference between the tourbillion and delayed Hopf bifurcation can be ambiguous.

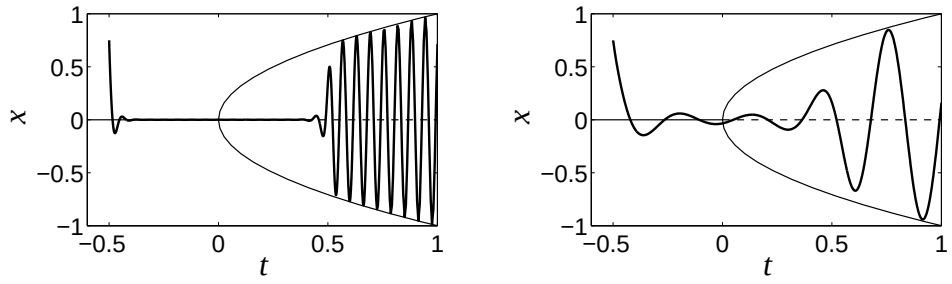

(a) $\epsilon = 0.01$. (b) $\epsilon = 0.05$.

Figure 1.1: Time series of the x-coordinate of (1.7) with an initial point: $(x, y, z) = (0.75, 0, -0.5)$. Trajectories in panels (a) and (b) have $\epsilon = 0.01$ and $\epsilon = 0.05$, respectively, and are shown on the fast time scale.

Consider the system for a dynamic Hopf bifurcation given by

$$\begin{aligned} \dot{x} &= -y + zx, \\ \dot{y} &= x + zy, \\ \dot{z} &= \epsilon. \end{aligned} \tag{1.7}$$

The z-coordinate can be decoupled from the system, and represents a scaled time coordinate $z = \epsilon t$. Using the scaled time, the first two equations can be written in polar coordinates as $\dot{r} = \epsilon t r$. A Hopf bifurcation of the fast subsystem occurs at $z = 0$. Figure 1.1 shows two trajectories of this system using an initial condition of $(x, y, z) = (0.75, 0, -0.5)$ at $\epsilon = 0.01$ and $\epsilon = 0.05$. At $\epsilon = 0.01$, Figure 1.7(a) shows that the trajectory follows the unstable branch of equilibria of the fast subsystem for a significant distance before following the limit cycles of the layer equation for $t > 0$. For $t < 0$, the amplitude of the oscillations decreases rapidly and is indistinguishable from $x = 0$. This behavior is classified as a delayed Hopf bifurcation. However, at $\epsilon = 0.05$, Figure 1.7(b) shows that the SAOs of the trajectory remain above a visible threshold throughout the entire SAO region. This is classified as a tourbillion.

1.3 Overview of the thesis

In this thesis, we use the techniques of geometric singular perturbation theory to investigate the dynamics of two chemical oscillators: a three-dimensional two time scale vector field derived from a toy chemical model called the "autocatalator," and a four-dimensional model of the BZ reaction reduced from an eleven-dimensional mass-action model. The former has an explicit time scale separation while the latter does not. In the case of the BZ reaction model, the separation of time scales can be estimated numerically so that the analysis of the system using GSPT is justified.

We analyze each model by decomposing the vector field into lower dimensional fast and slow subsystems. The dynamics of the full system are associated with the attractors of the fast subsystem. Changes in the attractors of the fast subsystem, which are constrained to the critical manifold, can radically alter the dynamics of the full system. In the case of the autocatalator, the critical manifold is two-dimensional, while the critical manifold of the BZ model is one-dimensional. Despite these differences, many of the same techniques can be used in the analysis of models.

In our analysis of the autocatalator [49], we develop a technique to calculate an induced one-dimensional map which approximates a highly dissipative two-dimensional return map. We use a combination of implicit numerical integration solvers and continuation methods [26] in order to calculate the induced maps. Using symbolic dynamics, we are able to predict admissible orbits and the bifurcations of MMOs of the full system.

For our analysis of the BZ reaction, we numerically estimate the separation

of time scales, which allows us to construct approximate fast and slow subsystems. We relate the dynamics of the full system to the bifurcations of the approximate fast subsystems. Using this technique, we show that dynamic Hopf bifurcations plays a key role in the organization of dynamics.

The remaining chapters of the thesis are organized as follows: chapter two details the analysis of the autocatalator. It is adapted from the work by Guckenheimer and Scheper [49] titled "A geometric model for mixed-mode oscillations in a chemical system," published in the SIAM Journal on Applied Dynamical System, Vol. 10, No. 1, pp. 92–128, 2011. Chapter three gives a history of the major experimental and modeling work concerning the BZ reaction. Chapter four gives the analysis of a four-dimensional model of the BZ reaction proposed by Györgyi and Field [53] called "Model D."

CHAPTER 2

ANALYSIS OF AUTOCATALATOR

2.1 Introduction

Mixed-mode oscillations (MMOs) are trajectories concatenated from large amplitude oscillations and small amplitude oscillations with a distinct difference between the amplitude of small and large oscillations (see Figure 2.1). MMOs are denoted by *signatures* $\{L_i^{s_i}\}_{i\geq 1}$, where each pair $L_i^{s_i}$ denotes a segment of the MMO comprised of L_i large oscillations followed by s_i small oscillations. MMOs have been observed in diverse physical, biological, neuronal, and chemical systems, notably including the Belousov-Zhabotinskii reaction [18, 34, 106, 10, 125]. Tables in the review [25] present an extensive list of systems exhibiting MMOs. There have been many proposed explanations for the existence of MMOs, including the break-up of an invariant torus [70], subcritical Hopf-homoclinic bifurcation [51], delayed Hopf bifurcation [71], singular Hopf bifurcation [43], and the *canard mechanism* [79, 80, 19].

This chapter presents a geometric analysis of MMOs exhibited by the autocatalator, a polynomial three-dimensional model of an isothermal chemical reaction with feedback, defined by

$$\begin{aligned} \dot{a} &= \mu(\kappa + c) - ab^2 - a, \\ \epsilon\dot{b} &= ab^2 + a - b, \\ \dot{c} &= b - c. \end{aligned} \tag{2.1}$$

The variables $a, b, c \in \mathbb{R}^+$ are concentrations of the chemical species of the model. For certain parameter values, this system exhibits MMOs. See Figure 2.1 for

a typical 1^2 MMO of (2.1). When ϵ is sufficiently small, the dynamics of the autocatalator may be partially reduced to a family of one-dimensional induced maps. We show that the induced maps give both a qualitative and a quantitative description of the bifurcations of the MMOs.

The autocatalator model was first proposed by Petrov, Scott, and Showalter [88] as a model of a prototypical chemical reaction that exhibits complex oscillations. Using extensive numerical calculations, they analyzed the bifurcations that occur between 1^n and 1^{n-1} periodic MMOs. They showed that these bifurcation sequences often begin and end with period doubling (PD) bifurcations, similar to the "period-bubbling" bifurcation [3]. They gave evidence also for two other bifurcations in the transitions: saddle-node (SN) bifurcations and crisis bifurcations. See [41] for more information on crisis bifurcations. The Petrov, Scott, and Showalter study [88] is numerical and does not address the underlying geometric structure of the attractors found in the system.

Milik and Szmolyan analyzed the autocatalator (2.1) in [79, 80] as a system with two time scales using geometric singular perturbation theory [29, 67]. They observed that the returns of a chaotic orbit to a particular cross section of this system appear to lie on a one-dimensional curve. Concluding that a one-dimensional map should be sufficient to describe the bifurcation sequences, they defined a one-dimensional return map on the intersection of the attracting slow manifold with a cross section near the fold. This return map had two critical points, so Milik and Szmolyan compared the bifurcation sequences of the autocatalator with the bimodal "Z-maps" of Ringland, Issa, and Schell [94]. They then computed examples of one-dimensional return maps that predicted stable MMOs for several parameter values.

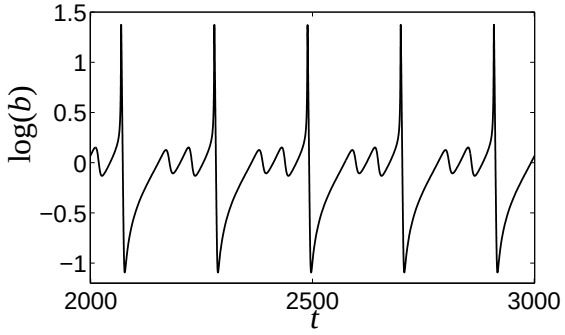

Figure 2.1: A typical MMO observed in system (2.1) for parameter values $(\epsilon, \mu) = (0.01, 0.2965)$. This a 1^2 MMO, one large relaxation-type oscillation proceeded by two small loops.

This chapter extends this analysis of the autocatalor by Petrov et. al. [88] and Milik and Szmolyan [79, 80] with a more detailed investigation into the geometric structure of the attractor. We begin our analysis by computing the location of a singular Hopf bifurcation [43] from which small amplitude oscillations of (2.1) emerge. This singular Hopf bifurcation is closely associated with the fold saddle-node, type II, bifurcation that was analyzed by Milik and Szmolyan in [80].

A key component of this work is the derivation of a family of one-dimensional maps from a three-dimensional vector field, similar to the previous investigations of Milik et. al. [79, 80], but our reduction occurs in two steps. First, a discrete time *return* map is constructed from successive intersections of trajectories with a cross section of the vector field [47]. The cross section we use passes through the equilibrium and is parallel to the one used by Milik et. al. [79]. We find that there is a region where the return map is nearly singular but also a region where this is not the case. In the second step, a one-dimensional map is constructed from the return map. One-dimensional

approximations of return maps for singularly perturbed systems have a long history that we review briefly below, where we also explain why the reduction is more complicated in our analysis of the autocatalator.

System (2.1) is an example of a slow-fast vector field. Section 2 reviews relevant theory of these systems briefly. Attracting slow manifolds are a prominent feature of slow-fast vector fields. In a three-dimensional system with two slow variables and one fast variable, an attracting slow manifold $\mathcal{S}_\epsilon$ is a surface that is highly contracting: trajectories approach $\mathcal{S}_\epsilon$ at an exponential rate on the fast time scale and then flow along $\mathcal{S}_\epsilon$ on the slow time scale. cross sections to $\mathcal{S}_\epsilon$ quickly evolve to exponentially thin strips that can be approximated by curves. (Approximate) return maps of these curves are the objects of interest. Attracting slow manifolds may end at folds where there is a tangency with the fast direction of the system (see Figure 2.3 below). The evolution of trajectories from a fold is a key aspect of the system dynamics. At most points of a fold, the trajectories "jump" along the fast direction. However, there may be points of intersection of attracting and repelling slow manifolds along a fold curve. A trajectory that contains such an intersection is called a *maximal canard*. A maximal canard evolves from the fold along the repelling slow manifold. However, nearby trajectories fly away from the repelling slow manifold along the fast direction. Transversal intersections of attracting and repelling slow manifolds therefore give rise to rapid expansion in the return maps. Trajectories that follow the maximal canard on opposite sides of the repelling slow manifold are torn apart and follow very different evolutions. See [27] for a treatment of canards using classical perturbation methods.

The scenario described in the previous paragraph is embedded in the classi-

cal work of Cartwright and Littlewood [20, 73] on the forced van der Pol equation [118] in which they give the first proof for the existence of chaotic dynamics of a dissipative dynamical system. The connection between iterations of one-dimensional maps and canards with the dynamics of the forced van der Pol equation is made explicit by Bold et. al. [15] and further analyzed by Haiduc [58]. Written as an autonomous vector field, the forced van der Pol equation is a three-dimensional slow-fast vector field whose state space is $\mathbb{R}^2 \times S^1$. Singular limits of the return maps of this system are one-dimensional maps except near maximal canards. In the parameter ranges considered, the singular limit of the system has a folded saddle point [13, 46] which gives rise to transversal intersections of attracting and repelling slow manifolds. Here the singular limit of the return maps become multivalued, reflecting the instability of trajectories flowing along the maximal canards for varying distances before they jump from the repelling slow manifold. Haiduc exhibits parameter values of the system for which he proves that the system is structurally stable and has a chaotic invariant set that is topologically equivalent to a *solenoid* [108, 58].

Folded nodes [13, 122] are a type of singularity of slow-fast systems with two slow variables that give rise to twisting of attracting and repelling slow manifolds and multiple maximal canards. The flow maps that describe how trajectories pass through a region close to a folded node can be approximated by one-dimensional maps with discontinuities at the maximal canards [45, 122]. Guckenheimer [44] gives a three-dimensional example of how this behavior can produce chaotic dynamics. Wechselberger and Weckesser [123] analyze the complex bifurcation structure of a seven-dimensional stellate cell model with a folded node. Rotstein, Wechselberger, and Kopell [97] argued that a three-dimensional slow-fast reduction of this seven-dimensional system successfully

models the dynamics of its subthreshold oscillations. Krupa, Popavić, and Kopell [68] analyze a model with three time scales that has a "slow passage through a canard explosion." They also compute a one-dimensional approximation of a return map for this system that has discontinuities along canards. In all these examples, the return map of the system has a Jacobian that is nearly singular throughout its domain.

In contrast to the examples described above, the return map of the autocatalator has mixed rank. In part of its domain, denoted Σ_1, trajectories follow an attracting slow manifold before returning to the chosen cross section, and the return map is nearly singular. However, in the region Σ_2 where there are small amplitude oscillations, the return map is regular and cannot be closely approximated by a one-dimensional map. The boundary between these regions consists of trajectories with canards that follow the repelling slow manifold for a substantial distance. For the most part, these orbits with canards do not reach the repelling slow manifold by first following the attracting slow manifold, so they do not satisfy the criteria for being maximal canards. All of the trajectories in the region we study do eventually enter the domain in which the return map is nearly singular. This allows us to define a one-dimensional *induced* map on the intersection of the attracting slow manifold with the cross section: its value is the first point that returns to the cross section along the attracting slow manifold. We could have shrunk the cross section to a region where this would be its first return, but we obtain additional insight into the dynamics of the system by investigating the dynamics near the canards originating from the common boundary of Σ_1 and Σ_2. These computations employ boundary value methods to continue highly unstable solutions of the flow. Our analysis enables us to "fill in" the discontinuities of the approximate one-dimensional induced maps

by following canard trajectories of the three-dimensional flow. We observe here for the first time that the connections on the two sides of the discontinuities have ranges that extend beyond the interval bounded by the limits on the two sides of the discontinuity.

We employ kneading theory of one-dimensional maps [23] and simulation to characterize the attractors of the induced maps. We also compare stable periodic MMOs in the three-dimensional flow with stable periodic orbits of the induced maps to relate the bifurcations of these two systems. We find that the kneading theory can be used to predict new details in the sequence of bifurcations. In particular, we use kneading theory to locate the existence of additional periodic windows of stable MMOs as a parameter of the autocatalator is varied. These results substantiate that the one-dimensional induced maps we construct give highly accurate predictions for the three-dimensional flow.

The remainder of the chapter is organized as follows. Section 2 reviews basic properties of the autocatalator model and discusses the mixed-rank behavior of its return map. Section 3 presents the main geometric objects in the cross section and explains the reduction of the system to a one-dimensional map. These interval maps are analyzed with symbolic dynamics in section 4.

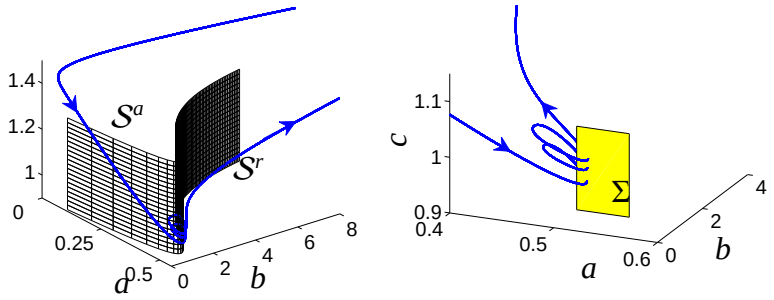

(a) MMO in phase space. (b) MMO intersecting Σ.

Figure 2.2: A 1^2 MMO at $(\epsilon, \mu) = (0.01, 0.2965)$ shown in phase space. (a) The critical manifold $\mathcal{S}$ is shown as a black mesh, with the attracting and repelling sheets S^a and S^r labeled. (b) An expanded view of the MMO near the fold. The trajectory intersects the cross section Σ, shown in yellow, three times.

2.2 The autocatalator model

2.2.1 Slow-fast calculations

The autocatalator model proposed by Petrov et. al in [88] is given by (2.1). The value of the parameter $\kappa = 2.5$ has been fixed to match the previous studies [88, 80]. System (2.1) is a slow-fast system with two slow variables and one fast variable. Setting $\epsilon = 0$ to obtain the DAE of the reduced system, the critical manifold $\mathcal{S}$ is a folded surface given by

$$\mathcal{S} = \left\{ (a, b, c) \in \mathbb{R}^3_+ \mid a = \frac{b}{b^2 + 1} \right\}. \tag{2.2}$$

Discussion of the reduced system can be found in [80].

The critical manifold $\mathcal{S}$ has two branches, separated by the fold curve given by $\mathcal{F} = \mathcal{S} \cap \{b = 1\}$. The stability of the branches can be found by taking a partial

derivative with respect to b,

$$\left.\frac{\partial(ab^2 + a - b)}{\partial b}\right|_{\mathcal{S}} = (2ab - 1)|_{\mathcal{S}} = \frac{b^2 - 1}{b^2 + 1}.$$

Let $\mathcal{S}^a$ denote the attracting branch of the critical manifold given by $\mathcal{S} \cap \{b < 1\}$, and let $\mathcal{S}^r$ denote the repelling branch defined by $\mathcal{S} \cap \{b > 1\}$. Figure 2.2 shows two views of the 1^2 MMO for the parameter values $(\epsilon, \mu) = (0.01, 0.2965)$. Figure 2.2(a) shows the critical manifold; its two branches are labeled $\mathcal{S}^a$ and $\mathcal{S}^r$. Figure 2.2(b) shows the intersections of the MMO with a cross section near the fold. Theorem 2 implies the existence of smooth, locally invariant slow manifolds $\mathcal{S}^a_\epsilon$ and $\mathcal{S}^r_\epsilon$ lying $O(\epsilon)$ from the attracting and repelling branches $\mathcal{S}^a$ and $\mathcal{S}^r$ of the critical manifold. For parameter values $(\epsilon, \mu) = (0.01, 0.2965)$, Figure 2.3(a) shows the slow manifolds $\mathcal{S}^a_\epsilon$ and $\mathcal{S}^r_\epsilon$ in blue and red, respectively. The critical manifold $\mathcal{S}$ is shown in gray. Figure 2.3(b) shows the intersections of the slow manifolds with a cross section near the fold, which illustrates that the slow manifolds intersect at an angle of order $O(\epsilon)$.

The geometry of the critical manifold, shown in Figure 2.4, is key to our analysis. Trajectories that make large excursions in the b-coordinate must cross the repelling sheet of the critical manifold before returning to the fold via the slow attracting manifold. They cross in a region where the angle between the critical manifold and the fast direction has become small, so that Theorem 2 fails to imply the existence of a nearby invariant slow manifold. Figure 2.4 shows the projection of both a 1^1 MMO at $(\mu, \epsilon) = (0.01, 0.298)$, shown in blue, and the critical manifold, shown in black, onto the ab-plane. The MMO crosses the critical manifold near $b \approx 23$, where the angle between the fast direction, indicated by black arrows, and the critical manifold is small. This loss of normal hyperbolicity enables the global return mechanism for the system: trajectories with large b-coordinate cross the critical manifold, follow the fast direction with $\dot{b} < 0$, and

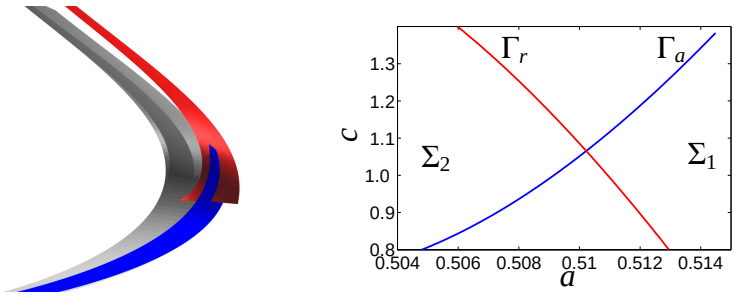

(a) Slow manifolds $\mathcal{S}^q_\epsilon$ and $\mathcal{S}^r_\epsilon$.

(b) Γ_a and Γ_r on Σ.

Figure 2.3: Slow manifolds of the autocatalator for parameter values $(\epsilon, \mu) = (0.01, 0.2965)$. (a) The critical manifold is shown in gray, and the slow manifolds $\mathcal{S}^q_\epsilon$ and $\mathcal{S}^r_\epsilon$ are shown in blue and red, respectively. The slow manifolds intersect transversally at a maximal canard. (b) The intersection of the slow manifolds with a cross section Σ given by the plane $b = 5\mu/(2 - 2\mu)$. $\Sigma \cap \mathcal{S}^i_\epsilon$ is denoted by Γ_i for $i \in \{a, r\}$. Γ_r (red) separates the cross section into Σ_1 and Σ_2.

approach the attracting slow manifold. As ϵ decreases, the repelling slow manifold extends further along the b-coordinate, and trajectories cross the critical manifold at still larger values of b. Milik and Szmolyan [80] assert that the large excursions can be cast as a singular perturbation problem with the assumption $b = O(1/\epsilon)$, but they do not give details. Gucwa and Smolyan prove the existence of a large periodic orbit for a two-dimensional variant of the autocatalator using the blow-up method [52].

2.2.2 Singular Hopf bifurcation

System (2.1) has a one-parameter family of equilibria, parametrized by μ, given by

$$(a, b, c)_{eq} = \left(\frac{10(\mu^2 - \mu)}{29\mu^2 - 8\mu + 4}, \frac{5\mu}{2(1-\mu)}, \frac{5\mu}{2(1-\mu)} \right). \tag{2.3}$$

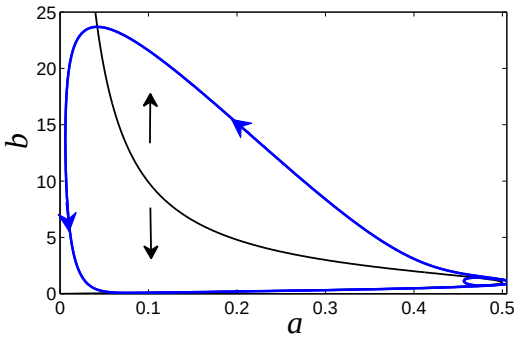

Figure 2.4: The critical manifold $\mathcal{S}$, shown in black, and a stable 1^1 MMO for $(\epsilon, \mu) = (0.01, 0.298)$, shown in blue, are projected onto the ab-plane. The fast direction is indicated by the black arrows. The trajectory crosses the critical manifold near $b \approx 23$, where the angle between $\mathcal{S}$ and the fast direction is small. Note the difference in scale of a and b.

The Jacobian of the system written in the slow time scale is

$$J(a, b, c; \epsilon, \mu) = \begin{pmatrix} -\epsilon(b^2+1) & -2\epsilon ab & \epsilon\mu \\ b^2+1 & 2ab-1 & 0 \\ 0 & \epsilon & -\epsilon \end{pmatrix}. \tag{2.4}$$

The Jacobian can also be expressed in terms of the parameters alone since the equilibrium depends only on μ.

A singular Hopf bifurcation (SHB) occurs when a Hopf bifurcation occurs $O(\epsilon)$ away from the fold for sufficiently small $\epsilon > 0$. At $\mu = 2/7$, the SHB occurs simultaneously with a saddle-node type II in the reduced system. Discussion of the SHB can be found in [4, 16, 43]. Other properties associated with the SHB are: (i) the periodic orbits born in the Hopf bifurcate or undergo *canard explosion*, and (ii) the slow attracting and repelling manifolds intersect transversally while varying a parameter [43]. Properties (i) and (ii) can be verified numerically using continuation software such as AUTO [26] or MATCONT [39].

Theorem 3. *System (2.1) has a singular Hopf bifurcation at* $\mu = 2/7 + O(\epsilon)$.

Proof. It must be shown that there is a Hopf bifurcation for $\mu = 2/7 + O(\epsilon)$ for $\epsilon > 0$. The characteristic polynomial of the system is

$$P(\lambda) = \lambda^3 + \lambda^2(1 - 2ab + 2\epsilon + \epsilon b^2) + \lambda\epsilon(b^2 - 2ab + 2 + (b^2+1)\epsilon) + \epsilon^2(b^2+1)(1-\mu). \quad (2.5)$$

A Hopf bifurcation occurs when the following two conditions are satisfied:

$$b^2 - 2ab + 2 + (b^2 + 1)\epsilon > 0, \quad (2.6a)$$

$$(1 - 2ab + 2\epsilon + \epsilon b^2)(b^2 - 2ab + 2 + (b^2 + 1)\epsilon) = \epsilon(b^2 + 1)(1 - \mu). \quad (2.6b)$$

Expanding (2.6b) and truncating higher order terms, we have

$$(2ab^3 - 4a^2b^2 - b^2 + 6ab - 2) + O(\epsilon) = 0. \quad (2.7)$$

Setting $\epsilon = 0$ and using (2.2) to express a and b in terms of μ, we have two solutions to (2.7), $\mu = 2/7$ and $\mu = -2/3$. We ignore the latter since it yields negative concentrations. When $\mu = 2/7$, the equilibrium is located at $a = b = 1$. The Hopf condition (2.6a) becomes

$$b^2 - 2ab + 2 + (b^2 + 1)\epsilon = 1 + O(\epsilon) > 0. \quad (2.8)$$

Therefore, a Hopf bifurcation occurs for $\epsilon > 0$ near $\mu = 2/7$. □

Figure 2.5 illustrates how MMOs are generated when an SHB is combined with a global return mechanism [43]. Let q be the equilibrium point near the fold, and fix $\epsilon > 0$. For $\mu_{Hopf} = 2/7 + O(\epsilon)$, q undergoes a supercritical Hopf bifurcation. Immediately after the Hopf bifurcation, q has a one-dimensional stable manifold $W^s(q)$ and a two-dimensional unstable manifold $W^u(q)$ bounded by the family of stable limit cycles, which we denote γ_μ. As μ increases, the Floquet multipliers of the limit cycle γ become complex, and the unstable manifold $W^u(q)$ begins to scroll around γ. Figure 2.5(a) shows the two-dimensional unstable manifold of the equilibrium point $W^u(q)$ in green and the slow repelling

manifold in red for $\mu = 0.2933$. $W^u(q)$ is bounded by the repelling slow manifold $\mathcal{S}^r_\epsilon$. $W^u(q)$ is approximated by computing trajectories with initial conditions emanating from a fundamental domain in the unstable eigenspace $E^u(q)$ tangent to the unstable manifold $W^u(q)$. Figure 2.5(b) shows the intersection of $W^u(q)$ and $\mathcal{S}^r_\epsilon$ with the plane $b = 1.25$. The intersection of γ with the section is indicated by a black cross. The turning point seen in $W^u(q)$ is a result of $W^u(q)$ scrolling around the limit cycle γ_μ, indicating that the nontrivial Floquet multipliers of the cycle are complex. As the diameter of $W^u(q)$ grows, it becomes tangent to $\mathcal{S}^r_\epsilon$ and then intersects the repelling slow manifold transversally. In this case, some trajectories contained in $W^u(q)$ escape the fold region and execute large excursions. Figure 2.5(c) shows a subset of $W^u(q)$ that contains the transversal intersection of $W^u(q)$ and $\mathcal{S}^r_\epsilon$ for $\mu = 0.2936$. This intersection can also be seen in the cross section $b = 1.25$ in Figure 2.5(d). This intersection is necessary for MMOs; however, it is not sufficient. For $\epsilon = 0.01$, the intersection occurs for $0.2933 < \mu < 0.2936$, but MMOs are not detected until $0.2940 < \mu < 0.2941$.

2.2.3 A mixed-rank return map

We begin our geometric analysis by choosing a cross section Σ_μ near the fold and considering its first return map $\Phi : \Sigma_\mu \to \Sigma_\mu$. The cross section is chosen to be parallel to the *ac*-plane so that it contains the equilibrium of system (2.1),

$$\Sigma_\mu = \left\{ (a, b_{\text{eq}}(\mu), c) \,\middle|\, b_{\text{eq}}(\mu) = \frac{5\mu}{2 - 2\mu},\ a > a_{eq} = \frac{b_{eq}}{b_{eq}^2 + 1} \right\}. \tag{2.9}$$

We emphasize that our choice of Σ_μ is μ dependent, but we write Σ_μ as Σ for simplicity. The inequality in (2.9) is imposed to ensure that returns to Σ have $\dot{b} > 0$. This allows us to properly count the number of small loops an MMO

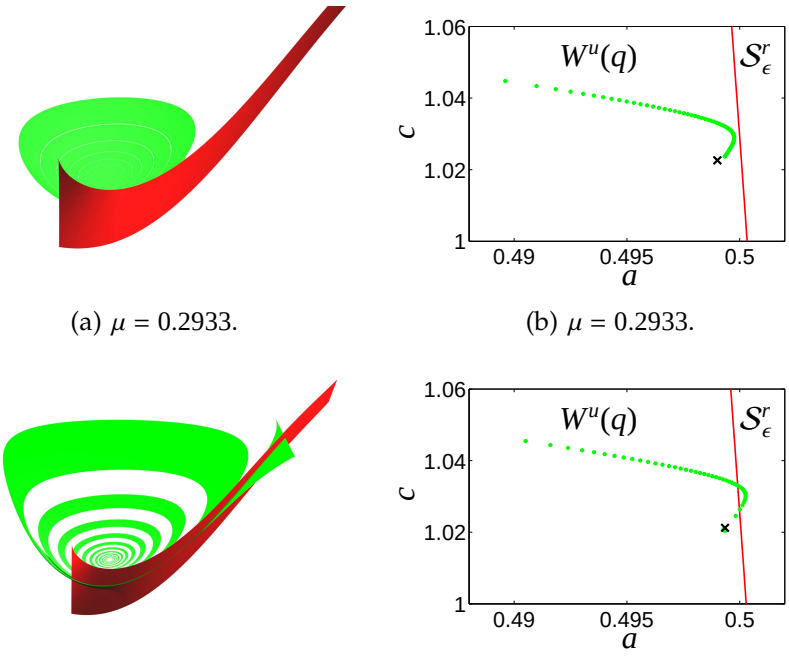

(a) $\mu = 0.2933$.

(b) $\mu = 0.2933$.

(c) $\mu = 0.2936$.

(d) $\mu = 0.2936$.

Figure 2.5: (a)-(b) $\mu = 0.2933$. (a) The two-dimensional unstable manifold of the equilibrium point $W^u(q)$ is shown in green. It is bounded by the slow repelling manifold $\mathcal{S}^r_\epsilon$, shown in red. (b) The intersections of $W^u(q)$ and $\mathcal{S}^r_\epsilon$ with the plane $b = 1.25$ are shown in green and red, respectively. The intersection of the limit cycle at $\mu = 0.2933$ is indicated by a black cross. (c)-(d) The corresponding manifolds are shown for $\mu = 0.2936$. (d) The intersections with the plane $b = 1.25$ show that $W^u(q)$ and $\mathcal{S}^r_\epsilon$ intersect transversally.

executes. We ignore the set of points $\mathcal{T} \subset \Sigma$ where the vector field is tangent to the cross section. $\mathcal{T}$ is given by the line $\mathcal{S} \cap \Sigma$. In practice, tangencies to Σ do not affect the dynamics because the forward invariant set does not intersect $\mathcal{T}$, its image, or its preimage.

The map Φ exhibits mixed-rank behavior. Let $\Gamma_i = \Sigma \cap \mathcal{S}^i_\epsilon$ for $i \in \{\mathrm{a}, \mathrm{r}\}$ be intersections of Σ with the attracting and repelling slow manifolds. Γ_r separates Σ into two regions, $\Sigma_1 = \{(a, c) \in \Sigma \mid c > \Gamma_r(a)\}$ and $\Sigma_2 = \{(a, c) \in \Sigma \mid c < \Gamma_r(a)\}$.

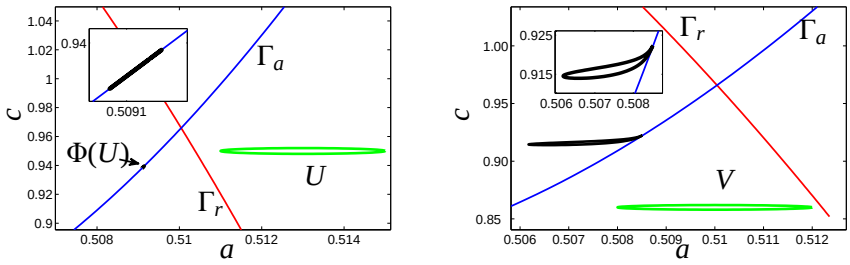

Figure 2.6: The first returns of two green circles of initial conditions at $(\epsilon, \mu) = (0.01, 0.298)$. Γ_a and Γ_r are shown in blue and red, respectively. (a) $U \subset \Sigma_1$ has a radius $r = 0.003$. $\Phi(U)$, shown in black, lies on Γ_a. (b) $V \subset \Sigma_2$ has a radius $r = 0.0025$. $\Phi(V) \subset \Sigma_2$.

Figure 2.3(b) shows the cross section partitioned into the two sets Σ_1 and Σ_2, separated by the repelling manifold Γ_r, shown in red. The return map Φ is regular when restricted to Σ_2, but is nearly singular at points of Σ_1 except those that are close to Γ_r.

Figure 2.6 illustrates the action of Φ in Σ_1 and Σ_2. It shows the first returns of two green circles of initial conditions on Σ: $U \subset \Sigma_1$ and $V \subset \Sigma_2$. Γ_a and Γ_r are indicated by blue and red lines, respectively. For any point $q \in \Sigma$, let $\phi_t(q)$ be the trajectory with initial condition q. Choose a point $p \in U$ which lies above the repelling manifold Γ_r. $\phi_t(p)$ is repelled away from the fold, where b grows rapidly on a large excursion. The trajectory $\phi_t(p)$ is reinjected onto the slow attracting manifold $\mathcal{S}^a_\epsilon$ by the global return mechanism. Therefore, $\Phi(p)$, and consequently $\Phi(U)$, must lie on Γ_a. Figure 2.6(a) shows the returns $\Phi(U)$ in black, with an expanded view of the returns shown in the inset. Although $\Phi(U)$ is diffeomorphic to a circle, the returns are indistinguishable from Γ_a. The one-dimensional returns exhibit the highly dissipative nature of Φ when restricted to Σ_1.

Figure 2.6(b) shows another circle of initial conditions V, shown in green. Let $q \in V$, and consider its trajectory $\phi_t(q)$. Because $V \subset \Sigma_2$, $\phi_t(q)$ cannot escape the fold region before intersecting Σ, and it executes a small loop in the vicinity of the fold. Since $\Phi(V)$ is not exponentially contracted to the slow manifold, the returns $\Phi(V)$ do not lie on Γ_a. The lack of exponential contraction of V to the slow manifold $\mathcal{S}_\epsilon^a$ implies that $\Phi|_{\Sigma_2}$ is regular. This is seen in Figure 2.6(b); the returns $\Phi(V)$ are shown in black and have a teardrop shape.

The dichotomy of small loops and large excursions can be used to determine the sectors of rotation on the cross section Σ. The jth *sector of rotation*, denoted RS^j, is the subset of Σ that executes j small loops before returning to Γ_a. If $\Phi^j(q) = \Phi \circ \cdots \circ \Phi(q)$ is the minimal iterate of Φ such that $\Phi^j(q) \in \Sigma_1$, then q lies in the jth sector of rotation, or RS^j. The definition implies that $\Phi(RS^{j+1}) \subset RS^j$ and $\Phi(RS^1) \subset \Sigma_1$. Therefore, the boundaries of the sectors of rotation are given by the inverse images of Γ_r. The sectors of rotation on Σ determine the sectors of rotation on the slow manifold $\mathcal{S}_\epsilon^a$ by taking the backward flow of the set $RS^k \cap \Gamma_a$ on Σ.

To summarize the behavior of the return map: initial conditions $p \in \Sigma_2$ which execute a finite number of small loops are mapped into Σ_1 and return to Σ on Γ_a. Initial conditions in Σ_1 execute a large excursion and return to Σ on Γ_a. Therefore, all initial conditions on Γ_a execute a number of small loops (possibly zero) and return to Γ_a by a large excursion. This is the key insight that allows us to reduce the system to a one-dimensional induced map: We can analyze the bifurcations of the MMOs by considering the induced map to Γ_a.

2.3 Induced maps and one-dimensional approximations

The previous section describes the behavior of the return map Φ and how its mixed-rank character can be exploited for analysis. In this section, we describe more of the geometry associated with the return map Φ. We identify a one dimensional set $X \subset \Sigma$ with a small neighborhood that is forward invariant. We approximate the return map Φ of the forward invariant set with a one-dimensional induced map. The construction of the induced maps depend upon the choice of Γ_a among the collection of exponentially close attracting slow manifolds. Numerical studies that compare bifurcations of the discrete one-dimensional maps and the continuous time flow of the autocatalator are presented in Section 5.

2.3.1 Geometric structure of Φ on Σ

To define X, we introduce some notation:

- $A_k = \Gamma_a \cap RS^k$ denotes the kth Γ-sector of rotation on Γ_a, with $A_0 = \Gamma_a \cap \Sigma_1$ denoting the segment of Γ_a above Γ_r;
- $\gamma^i = \Phi^i(\cup_{j \geq i} A_j)$ is the ith return of Γ_a via small loops;
- $\gamma^k_{A_j}$ denotes the kth forward image of A_j on γ^k for $k \leq j$; and
- $\partial RS^j = \Phi^{-j}(\Gamma_r)$ is the boundary of the jth sector of rotation.

Figure 2.7 shows the following geometric objects in Σ: the attracting and repelling slow manifolds Γ_a and Γ_r, the first two returns of Γ_a via small loops γ_1

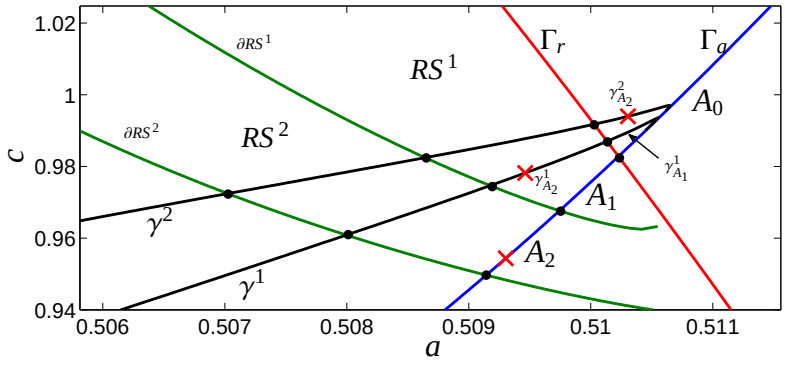

Figure 2.7: The geometric structure of Φ on Σ for $(\epsilon, \mu) = (0.01, 0.2965)$. Relevant geometric objects are labeled. The intersection of the stable 1^2 MMO with Σ is indicated by a red $\times$.

and γ_2, the sectors of rotation RS^1 and RS^2, the boundaries of the sectors of rotation ∂RS^1 and ∂RS^2, the segments $A_i \subset \Gamma_a$ for $i \in \{0, 1, 2\}$, and their images $\gamma^j_{A_i}$ for $j \in \{1, 2\}$. The secondary canards located at the intersections of the forward images of Γ_a with the backward images of Γ_r are marked by black dots. A kth *secondary canard* is a canard that executes k small loops before connecting to $\mathcal{S}^r_\epsilon$. The primary canard is given by the intersection $\Gamma_a \cap \Gamma_r$. See [45, 122] for more information about secondary canards at folded nodes.

The objects in Figure 2.7 organize the dynamics of Φ on Σ. Given a Γ-sector of rotation $A_k = RS^k \cap \Gamma_a$, the images $\Phi^j(A_k)$ follow the pattern

$$A_k \mapsto \gamma^1_{A_k} \mapsto \cdots \mapsto \gamma^k_{A_k} \mapsto \Gamma_a.$$

The image of the last map in this chain is not exact: $\Phi(\gamma^k_{A_k})$ is exponentially close to Γ_a, but we do not expect to be able to find Γ_a so that $\Phi(\gamma^k_{A_k}) \subset \Gamma_a$. Therefore,

we approximate the return map Φ on the $\gamma^k_{A_k}$ so that the set X defined by

$$X = \bigcup_{j=0}^{k} \bigcup_{i=0}^{j} \gamma^i_{A_j}$$

is invariant under the perturbed map. In the example shown in Figure 2.7, X consists of $A_0 \cup A_1 \cup A_2 \cup \gamma^1_{A_2} \cup \gamma^1_{A_1} \cup \gamma^2_{A_2}$. The set X is one-dimensional but need not be a manifold. Let $p_\mu : I \to \mathbb{R}$, for $I \subset \mathbb{R}$, denote a fourth-degree polynomial whose graph approximates Γ_a. We replace Γ_a by this polynomial approximation $\hat{\Gamma}_a$ and define $\hat{\Phi}^{k+1}(x)$ for $x \in A_k$ to be the point $(a, \hat{c})$ of $\hat{\Gamma}_a$ with the same a-coordinate as $\Phi^{k+1}(x) = (a, c)$. On each Γ-sector of rotation $A_k \subset \hat{\Gamma}_a$, we define the induced map $\Pi : A_k \to \hat{\Gamma}_a$ to be $\Pi(a) = \hat{\Phi}^{k+1}(a, p_\mu(a))$. We use a as a coordinate on $\hat{\Gamma}_a$ and drop the distinction between $\hat{\Gamma}_a$ and Γ_a in the remainder of this chapter.

The induced maps have a branch for each Γ-sector of rotation A_k. We refer to the branch of the map defined on A_k as the 1^k branch.

2.3.2 MMOs and induced maps

The connection between MMOs of the full system and periodic orbits of the induced maps can now readily be seen. Periodic MMOs yield periodic orbits of both Φ and Π. We expect the periodic orbits of Π to be exponentially close to those of Φ and ignore this difference in theoretical comparisons between the autocatalator flow and the induced map Π. Section 5 presents numerical investigations of these differences. A periodic MMO with signature $\{L_i^{s_i}\}_{i\geq 1}$ is period-n under Φ, where $n = \sum_i (L_i + s_i)$, and will be period-m under Π, where $m = \sum_i L_i$. Since each branch of the induced map corresponds to a sector of rotation, a fixed point of Π on the kth branch of the induced map corresponds to a 1^k MMO. The stability of the 1^k MMO in the full system is given by the magnitude of the

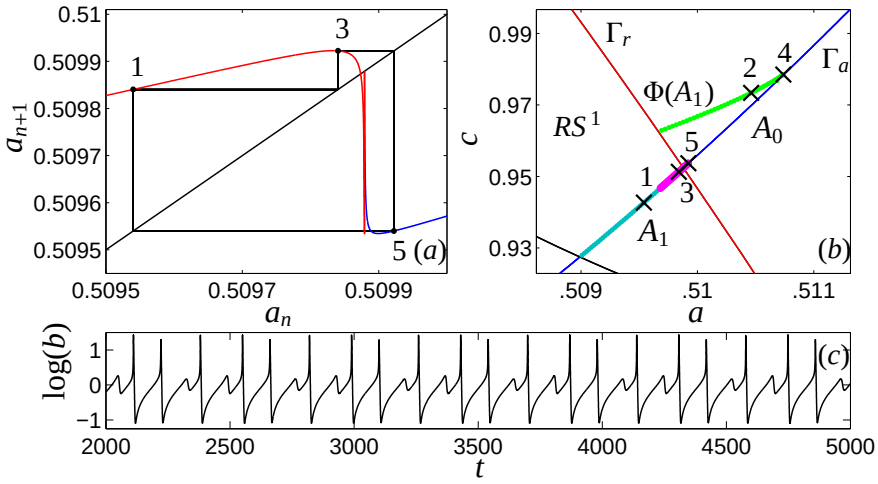

Figure 2.8: A periodic MMO for $(\epsilon, \mu) = (0.01, 0.2992)$. (a) The induced map Π shows the 1^0 and 1^1 branches in blue and red (resp.). The stable period-3 orbit is enumerated according to the returns of Φ seen in (b). (b) The Γ-sector of rotation A_1 is shown in cyan. The first and second returns of A_1, $\Phi(A_1)$ and $\Phi^2(A_1)$, are shown in green and magenta, respectively. Returns of the stable $2^1 1^1$ MMO are labeled 1-5. (c) The time series for the $2^1 1^1$ MMO.

slope of the induced map at the fixed point. For the parameter values in Figure 2.7, there is a stable 1^2 MMO, whose intersections with Σ are indicated by red crosses. The 1^2 MMO corresponds to a period-3 orbit under Φ, and its intersections follow the pattern

$$\cdots \mapsto A_2 \mapsto \gamma^1_{A_2} \mapsto \gamma^2_{A_2} \mapsto A_2 \mapsto \cdots .$$

More complicated MMOs will have multiple returns on Γ_a. Figure 2.8 shows the induced map Π, the first and second returns of Γ-sector of rotation A_1, and the time series for the stable $2^1 1^1$ MMO for the parameter values $(\epsilon, \mu) = (0.01, 0.2992)$. Figure 2.8(a) shows the induced map Π and its global attractor. The 1^0 blue branch and the 1^1 red branch give the a-coordinate returns of $\Phi(A_0)$, and $\Phi^2(A_1)$. Figure 2.8(b) shows a line of initial conditions on A_1 in cyan.

The first returns of A_1, shown in green, lie in Σ_1. The second returns $\Phi^2(A_1)$ are shown in magenta and lie on Γ_a. The period-5 periodic orbit of Φ is indicated by black crosses and enumerated. Three iterates of the orbit, enumerated 1, 3, and 5, lie on Γ_a. These points are enumerated on the period-3 orbit of Π seen in (a). Figure 2.8(c) shows the time series of the $2^1 1^1$ MMO which corresponds to the periodic orbits shown in (a)–(b). One full period of the time series contains three large excursions, indicating that the orbit is period-3 in the induced map. Throughout the rest of the chapter, all 1^0, 1^1, and 1^2 branches of induced maps will be shown in blue, red, and green, respectively.

2.3.3 Dynamics near the boundary layer

Our discussion of the return map Φ to this point has viewed Γ_r as the common boundary of regions Σ_1 on which Φ is nearly singular and Σ_2 on which Φ is regular. In order to fully describe the dynamics of Φ, we must investigate the dynamics of the boundary layer near Γ_r in more detail.

Let ℓ_{a_1} denote the line $\ell_{a_1} = \{(a, c) \in \Sigma \mid a = a_1\}$ for $a_1 \geq a_{eq}$, and consider the inverse image $\Phi^{-1}(\ell_{a_1})$. Figure 2.9 shows $\Phi^{-1}(\ell_{a_1})$ for sixteen equally spaced lines ℓ_{a_1} for $a_1 \in [0.509, 0.512]$. The return map Φ is a diffeomorphism, so the domain of Φ in the plane Σ is foliated by the family of inverse images $\Phi^{-1}(\ell_{a_1})$. Focus on the $a_1 = 0.512$ leaf of the foliation, drawn in green with a heavier linewidth. In Σ_1, the c-coordinate of the curve varies little and increases as the leaf nears Γ_r. The leaf turns and follows Γ_r with decreasing c for some distance and has a second turning point where it increases back through Σ_2. Figure 2.9(b) labels four inverse images in Σ_1. The maximum c-coordinate of each inverse image is

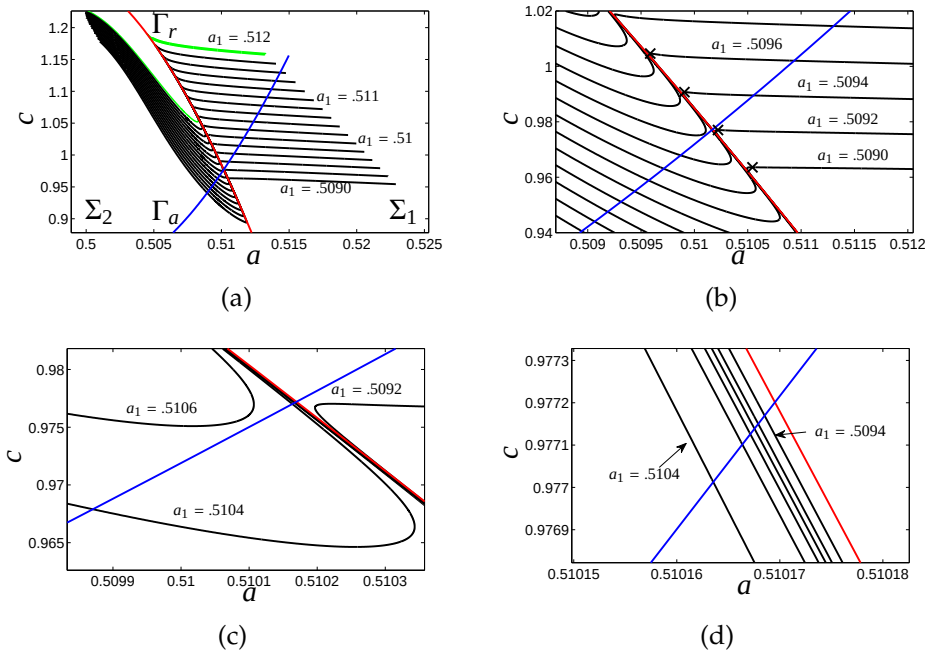

Figure 2.9: (a) The foliation of the return map Φ for $\mu = 0.297$ by inverse images of lines with constant a-coordinate for $a_1 \in [0.509, 0.512]$. Sixteen lines for equally spaced values of a_1 are drawn in green and black. Γ_a is drawn as a blue curve and Γ_r is drawn red. Increasingly expanded views of the foliation near $\Gamma_a \cap \Gamma_r$ are shown in (b)-(d). (b) Four inverse images are labeled. On each, the maximum c-coordinate in Σ_1 of the curves is marked by a black cross. (c) The inverse images of $a_1 = 0.5092, 0.5106$ are close to curves having tangencies with Γ_a in Σ_1 and Σ_2. (d) The inverse images have segments very close to Γ_r. This is due to the expansion of Φ near Γ_r.

marked by a cross. The maximum represents the minimum a-coordinate return for a line of constant c passing through the maximum. The distance between the maximum of the inverse image and Γ_r increases dramatically for leaves whose maxima occur below Γ_a. Figure 2.9(c) shows an expanded view of three inverse images near the intersection $\Gamma_a \cap \Gamma_r$, which are shown in blue and red. On either side of Γ_r, there is a unique inverse image which is tangent to Γ_a. Each tangency corresponds to a turning point in the a-coordinate of the line of first returns of Γ_a. The left tangency corresponds to a local maximum of the a-coordinate, and

the right tangency is a local minimum of the returns. For initial conditions on Γ_a between the tangency points, the return values of a decrease rapidly due to canards along trajectories with initial conditions close to Γ_r. Figure 2.9(d) shows that the inverse images are almost parallel to Γ_r in a neighborhood of Γ_r where the canard trajectories are found.

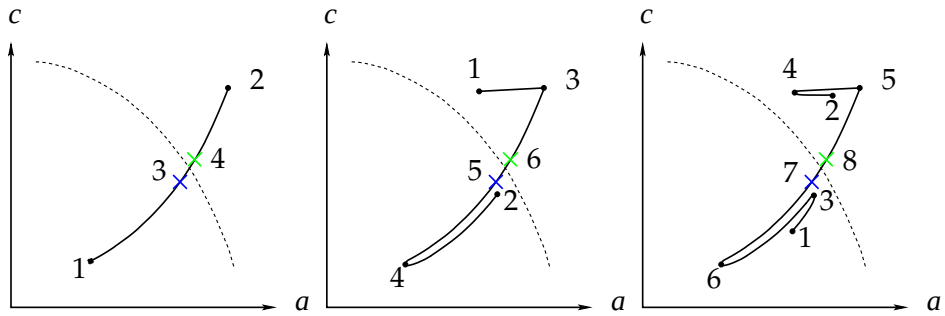

(a) Segment of Γ_a. (b) $\Phi(\Gamma_a)$. (c) $\Phi^2(\Gamma_a)$.

Figure 2.10: Cartoons of the first and second images of a segment of Γ_a under the return map Φ when the forward invariant set intersects only A_0, A_1, and their images. The endpoints of the segment of the Γ_a, the maximum and minimum of the foliation (blue and green crosses, respectively), and their images are enumerated. Enumerated points in (b) and (c) are the images of the corresponding points in (a) and (b). (a) Segments of the manifolds Γ_a (solid) and Γ_r (dashed) are shown. (b) The first return of Γ_a. (c) The second return of Γ_a. All "hooked" segments of the returns in (b) and (c) lie exponentially close to one another.

Suppose that the forward invariant set of Φ lies on A_0, A_1, and their images. Then any point on Γ_a returns to Γ_a in one or two iterates of Φ. Figure 2.10 shows a cartoon for the first two images of Γ_a. Figure 2.10(a) shows a segment of Γ_a and the two turning points of $\Phi|_{\Gamma_a}$, labeled with blue and green crosses. The endpoints of the segment of Γ_a drawn in the figure are labeled 1 and 2, and the turning points are labeled 3 and 4. The image of Γ_a is shown in Figure 2.10(b). The segment $\overline{13}$ lies on A_1 and returns with increased a-coordinate, and the segment $\overline{42}$ returns with decreased a-coordinate. Since $\overline{42} \in \Sigma_1$, $\Phi(\overline{42})$ lies exponentially

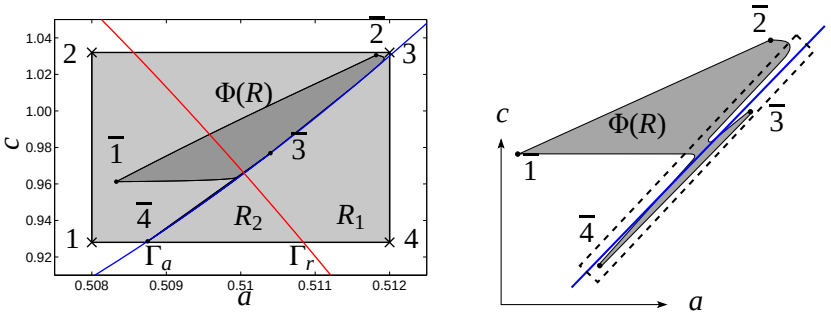

(a) $R = R_1 \cup R_2$ and its image $\Phi(R)$. (b) Cartoon of $\Phi(R)$.

Figure 2.11: A trapping region for Φ at $(\epsilon, \mu) = (0.01, 0.297)$. (a) A rectangle R (light gray) and $\Phi(R) \subset R$ (dark gray). The four corners of R are enumerated 1–4 and indicated by black crosses. The returns of the corners are marked with heavy dots and enumerated $\overline{1}$–$\overline{4}$. Γ_r partitions R into $R_i = R \cap \Sigma_i$. $\Phi(R_1)$ is exponentially contracted to Γ_a. (b) A cartoon of the returns $\Phi(R)$. Points labeled $\overline{1}$–$\overline{4}$ correspond to the images of the corners of R. All of the images $\Phi(R)$ that intersect the region bounded by dotted lines are contracted to Γ_a.

close to Γ_a. The orientation of these segments is preserved: the a-coordinates of the images is increasing as the a-coordinate of the preimages increases. This is not true for the segment $\overline{34}$, where the orientation of this segment is reversed. Figure 2.10(c) shows the second iterate of Γ_a. $\Phi(\overline{245})$ lies above Γ_a in Σ_1. The segment $\overline{631}$ in Figure 2.10(b) is again mapped exponentially close to Γ_a just like $\overline{42}$ in Figure 2.10(a). The one-dimensional approximation of $\Phi^2(\Gamma_a)$ has two turning points in Σ_2 – at points 3 and 6. The two turning points can be seen in Figure 2.8(a). The red 1^1 branch in Figure 2.8(a) consists of the second returns of A_1, which has two turning points.

Figure 2.11(a) shows a rectangle R that is mapped into itself by Φ for $(\epsilon, \mu) = (0.01, 0.297)$. R is shaded gray and is bounded by segments of the lines $a = 0.508$, $a = 0.512$, $c = 1.03$, and $c = 0.928$. The corners of R are enumerated 1–4 and marked with crosses. $\Phi(R)$ is shaded dark gray, and the images of the corners

of R are indicated by dots and are enumerated $\overline{1}$–$\overline{4}$. Γ_r partitions R into $R_i = R \cap \Sigma_i$. $\Phi(\overline{23})$ has two folds in the a-coordinate, while $\Phi(\overline{14})$ has only one. This is due to the increasing distance between Γ_r and the maximum a-coordinate of the inverse images of Φ by lines of constant a in Σ_1 whose maxima occur below Γ_a. Since $\Phi(\Sigma_1)$ is highly dissipative, the image $\Phi(R_1)$ is exponentially contracted to Γ_a. Figure 2.11(b) shows a cartoon of $\Phi(R)$ that makes the turning points more visible.

2.3.4 Computation of the induced maps

Computation of the induced maps by forward integration is difficult for trajectories that pass through the boundary layer near Γ_r. These trajectories possess canards, segments that follow the repelling slow manifold. The separation of trajectories along this manifold is sufficiently rapid that extraordinarily fine resolution of meshes of initial conditions are required to find the trajectories with long canard segments. Instead of pursuing this strategy, we use the boundary value solver AUTO [26] to compute trajectories in these regions. Our computations of the induced maps proceed in three steps:

1. approximate Γ_a by a polynomial,
2. integrate one trajectory from each Γ-sector of rotation that satisfies the boundary conditions in (2.10), and
3. compute all branches that intersect the forward invariant set by continuing these trajectories along Γ_a.

Our approximation of Γ_a is based on the observation that trajectories with initial points that make large loops return to Σ along the attracting slow manifold. We choose 200 points equally spaced along the line $\ell = \{(a, b, c) \in \mathbb{R}^3 \mid a = b = 0.1\}$ as initial conditions with c-coordinates selected so that their returns extend across the segment of Γ_a that is the domain for the induced map Π. Trajectories are computed to their intersection with Σ using the Radau5 integration algorithm [59], which is a fifth order variable-time step implicit solver with eighth order dense output for stiff systems. Relative and absolute error tolerances were set to 10^{-12} and 10^{-13}, respectively. We fit the return points to the graph of the fourth order polynomial $c = p_\mu(a)$ that minimizes the least squares residual.

Each branch of the induced map is calculated individually by continuation of a single trajectory from each Γ-sector of rotation in the forward invariant set. The program AUTO employs a pseudo arc-length continuation to solve the boundary value problem for a trajectory $\mathbf{x}(t)$ of (2.1) with time rescaled by a factor determined by AUTO subject to four boundary conditions:

$$\begin{aligned} \mathbf{x}(0) &\in \Gamma_a(I), \\ \mathbf{x}_2(1) &= 5\mu/(2-2\mu), \end{aligned} \tag{2.10}$$

where $I \subset \mathbb{R}$ is an appropriately chosen interval. These calculations successfully compute trajectories with canard segments that lie along the repelling slow manifold. The terminal points of the continued family of orbits are analyzed to find returns that lie exponentially close to Γ_a. We project the returns of the induced map onto Γ_a parallel to the c-axis to obtain the value of Π. The residual of $\Pi - \Phi^{k+1}$ on A_k is the difference of their c-coordinates since Π was defined to have the same a-coordinate as Φ^{k+1}. All AUTO continuations in this chapter utilize 500 mesh points with four collocation points per mesh.

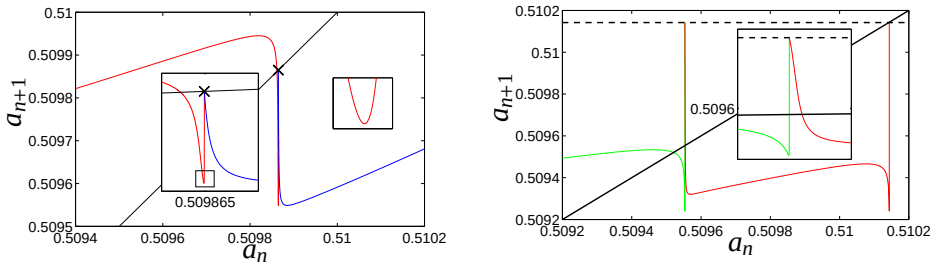

(a) $\mu = 0.2993$. (b) $\mu = 0.2972$.

Figure 2.12: Induced maps for two values of μ. The 1^0, 1^1, and 1^2 branches are shown in blue, red, and green, respectively. All critical points of the induced maps are smooth except the intersection of the branches. (a) The induced map at $\mu = 0.2993$. The intersection of the branches is indicated by a black cross. (b) The induced return map at $\mu = 0.2972$. The dotted line indicates the a-coordinate of the fixed point of Φ that lies on the small periodic orbit born from a Hopf bifurcation. The intersection of the green and red branches, shown in the inset, is a preimage of this fixed point near $a_n = 0.510142$.

Figure 2.12 shows the induced maps for $\mu = 0.2972$ and $\mu = 0.2993$. Throughout the chapter, the returns of 1^0, 1^1, and 1^2 branches are plotted in blue, red, and green, respectively. Consider the induced map at $\mu = 0.2993$. The map consists of two branches: a unimodal 1^0 branch (blue) and a bimodal 1^1 branch (red). The insets show that all critical points are smooth. The branches are terminated at their intersection in order to obtain a continuous induced map. This has the practical effect of distinguishing small loops from large loops by comparing the diameter of loops to the diameter of the periodic orbit born from the Hopf bifurcation. The termination point $(q, p_\mu(q)) \in \Sigma$ corresponds to a periodic orbit intersecting Γ_a because $\Phi^2(q, p_\mu(q)) = \Phi(q, p_\mu(q))$. A continuation of the family of periodic orbits born from the Hopf bifurcation locates the intersection of the periodic orbit with Σ at the point $(a, c) \approx (0.509864, 0.951337)$. The a-coordinate of the periodic orbit is marked on the induced map in Figure 2.12(a) with a black cross. This point lies exponentially close to the intersection of the two branches,

confirming that the intersection of the two branches corresponds to the location of a small periodic orbit.

Now consider the return map at $\mu = 0.2972$ shown in Figure 2.12(b). The 1^2 branch in green and 1^1 branch in red are continued until their intersection near $a_n \approx 0.50955$. The intersection of these curves implies that the 1^2 trajectories from the left approach the same return as the 1^1 trajectories from the right. The intersection of the two branches maps exponentially close to the a-coordinate of the small periodic orbit. AUTO calculates the location of the small periodic orbit on Σ at $(a, c) \approx (0.510142, 0.974840)$. The line $a_{n+1} = 0.510142$ is plotted as a dotted black line. The inset shows that the line gives the a-coordinate of the fixed point on the red 1^1 branch of returns.

2.4 Periodic MMOs in flows and induced maps

We fix $\epsilon = 0.01$ for the remainder of the chapter. Figure 2.13 shows the bifurcation diagram of Φ for an interval of the parameter μ where MMOs occur. For 1000 equally spaced values of $\mu \in [0.293, 0.3005]$, the limit set of representative trajectories is projected onto the a-axis. Eight bands of stable periodic MMOs are visible, and their signatures are labeled on the diagram. We define a *band* of stable MMOs to be an interval of the parameter μ where the global attractor of the full system is a stable periodic MMO. A *transition* between MMOs is an interval of the parameter μ between two stable bands of MMOs.

We present details about the errors associated with the computation of the induced maps and the accuracy of the bifurcations predicted by the induced maps. This section employs kneading theory [81] of one-dimensional maps to

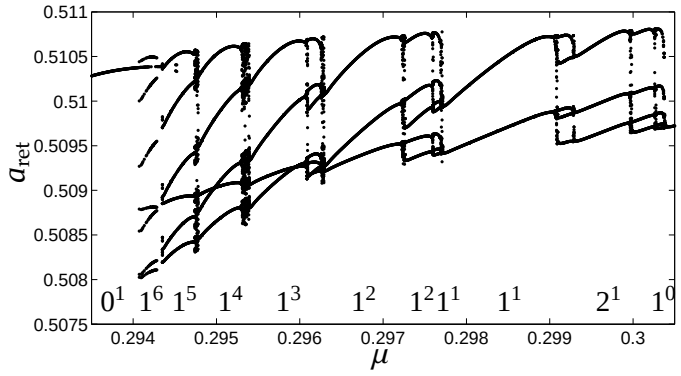

Figure 2.13: Bifurcation diagram at $\epsilon = 0.01$. Labels are shown for bands of stable MMOs that persist over large parameter regions.

analyze the bifurcation diagram. To show that the one-dimensional theory applied to the geometric reduction allows for a comprehensive understanding of the sequence of bifurcations that occur between stable MMOs, we present a detailed analysis of bifurcations that occur in the $2^1 1^1 \to 2^1$ MMO transition.

2.4.1 Symbolic dynamics of induced maps

Kneading theory uses symbolic dynamics to characterize invariant sets of piecewise monotone, one-dimensional maps of an interval to itself. We apply it here to study the induced map Π of the autocatalator. The domain of Π is partitioned into subintervals so that Π is monotone on each subinterval and given by a particular iterate of the return map Φ. We always use the minimal partition with these properties. The partition points are called critical points. We associate symbols with each subinterval and each critical point of the partition. Symbolic dynamics records the sequence of symbols associated with each trajectory. The *kneading data* consists of the symbolic sequences assigned to the

critical values [42, 81, 23]. One of the main theorems of kneading theory is that the kneading data essentially determine the full set of symbol sequences that are associated with other trajectories of the one-dimensional map. The theory also establishes conditions for the kneading data to be self consistent, so that it arises from a one-dimensional map. It gives further information about bifurcations that are associated with changes of kneading data in families of maps.

For one-parameter families of continuous, unimodal maps g with a single critical point and endpoints a, b that satisfy $g(a) = a = g(b)$, the kneading data is a single sequence and the families display universal sequences of bifurcations. For maps with k critical points, universal families depending upon k parameters can be defined [42]. An arbitrary family can be mapped into these universal families so that its bifurcations are mapped to the bifurcations of the universal family. If the maps have negative Schwarzian derivative [23], more is true. In that case, there is a critical point that approaches each attractor. Consequently, the possible attractors can be determined immediately from the kneading data. For each stable periodic orbit, there is a critical point whose itinerary follows the itinerary (symbol sequence) of that periodic orbit. Even if a map does not have negative Schwarzian derivative, these relations between attractors and critical points are likely to hold. We use them as a guide to our numerical analysis of the induced maps.

From kneading data we can determine the possible bifurcation sequences that arise in a one-parameter family connecting two maps. We use this observation to make predictions about the bifurcations of the autocatalator model. Starting with the induced map Π for different parameter values, we use kneading theory to infer the existence of intermediate bifurcations and parameter

regimes with MMOs having specific signatures. At each parameter value, the kneading data determines the itineraries of periodic orbits for that map. If a periodic itinerary occurs at the second parameter value but not the first, then we conclude that there must be a bifurcation that created the periodic orbit at an intermediate value of the parameter. We confirm predictions based upon this analysis of the symbolic dynamics of the induced map with numerical solution of initial and boundary value problems for the autocatalator system.

2.4.2 Itineraries of periodic MMOs

In this work, we consider only induced maps that have either one or two branches. Each branch can be partitioned into piecewise monotone subintervals, called *laps*. In the parameter regime that we consider, the induced maps have either five laps or seven laps. Table 2.1 lists the itineraries and absorbing sets for the eight bands of stable MMOs seen in this interval. The maps whose forward invariant sets lie on $A_2 \cup A_1$ have seven laps, and those whose forward invariant sets lie on $A_1 \cup A_0$ have five laps. Typical return maps from the five- and seven lap families are shown in Figure 2.14. Each critical point of the map is denoted by a bold letter **L** or **R**, indicating the branch on which the critical point lies, with a bar or hat to distinguish different critical points on the same branch. In both families of maps, **C** is given by the intersection of the two branches. The laps are denoted by L_i and R_i with subscripts increasing with a. The endpoints of the forward invariant interval are denoted by $\mathbf{L_{end}}$ and $\mathbf{R_{end}}$. In both families, the induced maps are smooth at all critical points except **C**.

Geometric properties of the return map Φ allow us to make general state-

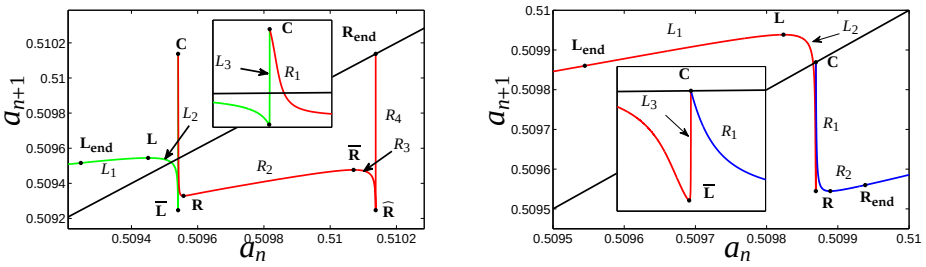

(a) 7 lap map.

(b) 5 lap map.

Figure 2.14: Induced maps with five and seven laps. The laps and critical points are labeled. The inset shows the critical point **C** and its adjacent laps. (a) A seven lap induced map at $\mu = 0.2972$. (b) A five lap induced map at $\mu = 0.2993$.

Family	μ	MMO	Itinerary
7 Lap	0.297	1^2	L_1
	0.2974	$1^2 1^1$	$L_1 R_2$
	0.29765	$1^2(1^1)^2$	$L_2 R_2 R_2$
5 Lap	0.2985	1^1	L_1
	0.2992	$2^1 1^1$	$L_1 L_2 R_2$
	0.2995	2^1	$L_1 R_2$
	0.3001	3^1	$L_1 R_2 R_2$
	0.30033	4^1	$L_1 R_2 R_2 R_2$

Table 2.1: The μ value, signature, and itinerary for an MMO in each of the eight large bands of stable MMOs in the five- and seven lap families.

ments about the kneading data of the induced maps. The intersection of the branches is a fixed point or the preimage of a fixed point since we have $\Pi^i(a) = \Pi^{i-1}(a)$. Therefore, in the seven lap map, we have $\Pi(\mathbf{C}) = \Pi(\mathbf{R_{end}}) = \mathbf{R_{end}}$, and in the five lap map, $\Pi(\mathbf{C}) = \mathbf{C}$. The minimum of each branch is given by the tangency to Γ_a by the foliation of Φ by inverse images of lines of constant a. Therefore, the minimum returns for each branch are equal: $\Pi(\overline{\mathbf{L}}) = \Pi(\widehat{\mathbf{R}})$ in the seven lap map and $\Pi(\overline{\mathbf{L}}) = \Pi(\mathbf{R})$ in the five lap map. These properties constrain the kneading data of the maps. For a map with five laps, let Σ be any sequence of symbols from the five letter alphabet $\{L_1, L_2, L_3, R_1, R_2\}$, and let the

signs $[+1, -1, +1, -1, +1]$ indicate whether the laps are increasing or decreasing. Let $\mathcal{L}_i(\Sigma)$ ($\mathcal{R}_i(\Sigma)$) indicate the subsequences of Σ that follow the symbol L_i (R_i).

Definition 4. *The sequence Σ is admissible if and only if the following conditions are met:*

$$\begin{aligned} &\Pi^2(\mathbf{R}) \leq \mathcal{L}_1(\Sigma) \leq \Pi(\mathbf{L}), \quad \Pi(\mathbf{R}) \leq \mathcal{R}_1(\Sigma) \leq \mathbf{C}, \\ &\Pi(\mathbf{R}) \leq \mathcal{L}_2(\Sigma) \leq \Pi(\mathbf{L}), \quad \Pi(\mathbf{R}) \leq \mathcal{R}_2(\Sigma) \leq \Pi^2(\mathbf{L}), \\ &\Pi(\mathbf{R}) \leq \mathcal{L}_3(\Sigma) \leq \mathbf{C}. \end{aligned} \tag{2.11}$$

The itinerary of any point is admissible. A basic theorem in kneading theory is a partial converse: if a sequence Σ is admissible with strict inequalities in this definition, then there exists a point whose future corresponds to the symbolic sequence Σ. Since the kneading sequence of the critical point $\mathbf{C}$ is fixed, only the kneading sequences of $\mathbf{L}$ and $\mathbf{R}$ vary with μ. The admissibility of any sequence Σ depends only on the itineraries of the critical values of $\mathbf{L}$ and $\mathbf{R}$. Conditions similar to (2.11) may be written down for the seven lap family.

Figure 2.15 shows the induced map, the globally attracting limit set, and the time series of each MMO listed in Table 2.1. The periodic orbits of the induced maps correspond to limit cycles in the full system. The sectors of rotation allow us to read off the signature of the limit cycle. In the five lap family, an iterate on the $\mathbf{R}$ branch corresponds to a single large amplitude oscillation, and any iterate on the $\mathbf{L}$ branch corresponds to a small amplitude oscillation followed by a large amplitude oscillation. For example, the signature of the MMO for $\mu = 0.3001$ shown in Figure 2.15 is 3^1.

The kneading data of a one-dimensional system gives additional information about the dynamics. In particular, the critical values often lie at the boundaries of chaotic attractors. We can see this phenomenon in the bifurcation

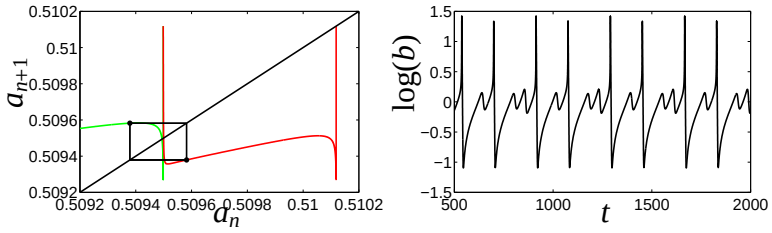

(a) $\mu = 0.2974$.

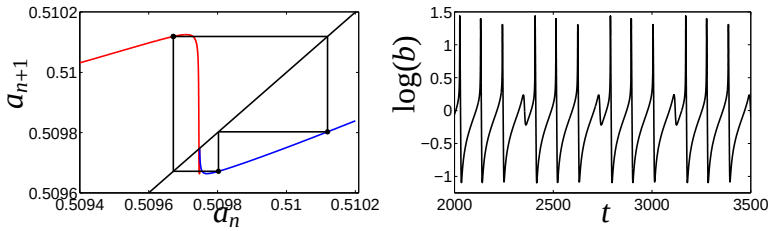

(b) $\mu = 0.3001$.

Figure 2.15: The induced maps and time series of stable MMOs for two values of μ listed in Table 2.1.

diagrams of the full system. Figure 2.16 shows the $2^1 \rightarrow 3^1$ transition for $\mu \in [0.29995, 0.29999]$. The induced maps for 41 equally spaced values of μ in the interval are computed. The a-coordinate of the critical values of **L** and **R** from the induced maps are shown in black. Many of the attractors within this region are bounded below by **R**, evidence that the family of induced maps successfully predict properties of the full system. We note that the points of this bifurcation diagram that lie above **L** correspond to returns following small amplitude oscillations that are not part of the induced map trajectories.

2.4.3 Numerical accuracy of the induced maps

In section 2.3.4, we enumerated the steps in computing induced maps. Each step in the computation makes approximations; we investigate the errors of these approximations. Subsequent subsections examine the accuracy of the periodic

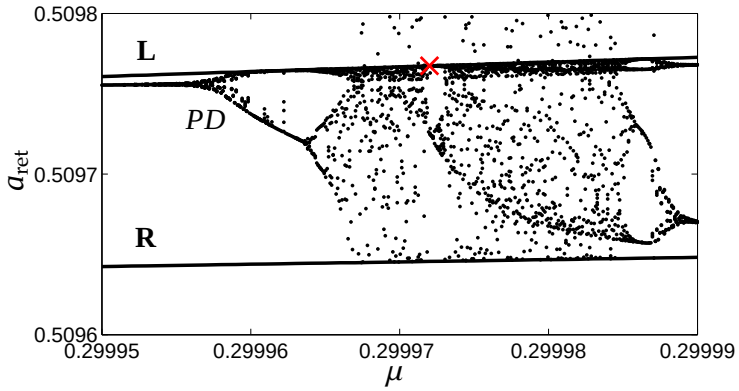

Figure 2.16: An expanded view of the $2^1 \rightarrow 3^1$ transition. The a-coordinates of critical points **L** and **R** computed from 41 induced maps in the interval $[0.29995, 0.29999]$ are shown in black. A period-doubling bifurcation near $\mu = 0.299958$ is labeled *PD*. The red cross indicates the location of a period-3 superstable orbit for the induced return map which corresponds to a 3^1 MMO in the full system.

MMOs and their bifurcations predicted by the maps.

Figure 2.17 shows the residual errors $\Delta c = |c_{\text{ret}} - p_\mu(a_{\text{ret}})|$ associated with the computation of the induced map Π for $\mu = 0.2993$; see Figure 2.17(a). The black cross indicates the intersection of the 1^0 and 1^1 branches. Figure 2.17(b) shows the invariance of the return map Φ. Let G_a denote the set of points used to estimate Γ_a. G_a is shown in cyan, with the segment of Γ_a it defines for the interval $a \in [0.5094, 0.5102]$ shown as a black curve. The first and second returns of 200 equally spaced numerically integrated initial conditions on Γ_a are shown in blue and red, respectively. These returns lie on both $\gamma^1(\Gamma_a)$ and Γ_a. Figure 2.17(c) shows the residual Δc for G_a, and the first and second returns of Γ_a to Σ, on a semilog plot. The dashed black line indicates a difference of 10^{-9}, shown for reference. In the first and second sectors of rotation, the difference Δc for the first and second returns (resp.) is roughly $O(10^{-9})$. The residuals vary up to 10^{-2} for returns not contracted to Γ_a. The residuals of the G_a are roughly

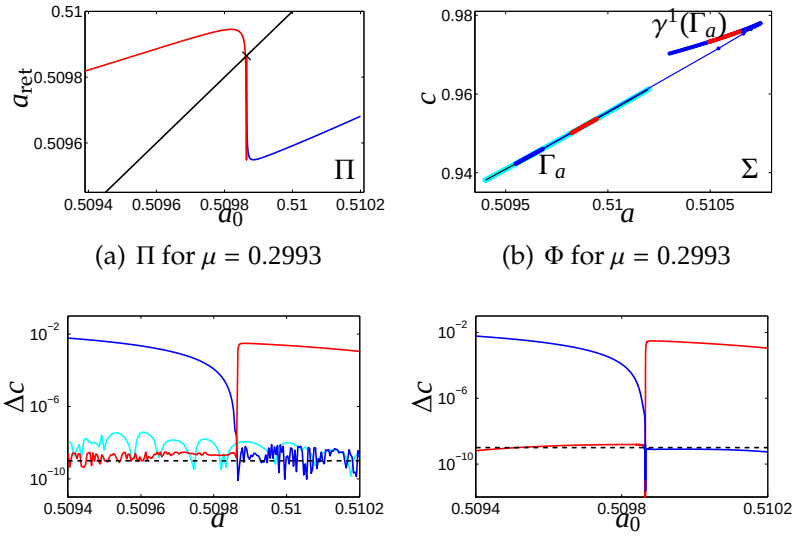

(a) Π for $\mu = 0.2993$ (b) Φ for $\mu = 0.2993$

(c) Δc for Num. Int. (d) Δc for Cont.

Figure 2.17: Residuals related to the invariance of Φ on Γ_a at $\mu = 0.2993$ tested via numerical integration and continuation methods. (a) The induced map at $\mu = 0.2993$. (b) G_a is shown in cyan, and Γ_a is shown in black. The first and second numerically integrated returns of 200 evenly spaced points on Γ_a are shown in red and blue. (c) The residuals Δc for several returns: G_a (cyan), the first and second returns of Γ_a (blue and red). (d) The residuals of the branches computed using continuation methods that satisfy (2.10).

$O(10^{-8})$. Figure 2.17(d) shows the residuals Δc of the returns of the two branches of the induced map computed using continuation. Again, the residuals of the branches in the sectors of rotation are roughly $O(10^{-9})$. There is a small interval near $\Gamma_a \cap \delta RS^1$ where both the first and second returns return close to Γ_a. This interval contains the intersection of the branches, given by the a-coordinate of the intersection of the limit cycle born from the Hopf bifurcation with Σ. This illustrates that termination of the branches at their intersection is consistent with the requirements of the induced map.

Because the returns of our chosen Γ_a are projected onto itself, the induced

maps only approximate the dynamics of the full system. We can test the accuracy of our maps by analyzing the kneading data for small perturbations of the μ parameter for values of μ whose periodic orbits contain critical points, also called *superstable orbits*. Let a_0 be the first point on a period-k periodic orbit. Then the address of the period-k orbit is given by $\mathbf{a} = a_0 a_1 \dots a_{k-1}$. The orbit $\mathbf{a}$ is stable if the following condition is satisfied:

$$\left| \frac{d\Pi^k}{da}(a_j) \right| = \prod_{i=1}^{k} |\Pi'(a_i)| < 1. \tag{2.12}$$

When (2.12) is satisfied, a linear stability analysis shows that nearby orbits converge to the periodic orbit [60]. When the product in (2.12) vanishes, convergence is quadratic and the orbit is called superstable. The superstable orbits of the induced maps correspond to limit cycles in the full system with pure imaginary multipliers. We test the accuracy of the induced maps, examining their fluctuations near superstable orbits, where the kneading data of a map changes.

Near $\mu = 0.29988$, there is a superstable period-2 orbit $\Pi^2(\mathbf{L}) = \mathbf{L}$. Figure 2.18(a) shows the return map for $\mu = 0.29988$. The inset shows the critical point $\mathbf{L}$ and its second iterate $\Pi^2(\mathbf{L})$. At $\mu = 0.29988$, $\Pi^2(\mathbf{L}) \in L_1$ and $\Pi^2(\mathbf{L}) - \mathbf{L} < 0$. The difference for $\mu = 0.29988$ value is marked with a black cross in the expanded view of Figure 2.18(b). Figure 2.18(b) shows the difference $\Pi^2(\mathbf{L}) - \mathbf{L}$ for $\mu \in [0.29985, 0.2999]$, using partitions of the interval with three different mesh spacings: 10^{-5}, 10^{-6}, and 10^{-7}. The difference is monotone for induced maps in both intervals $\mu \in [0.29985, 0.2993]$ and $\mu \in [0.29987, 0.29989]$ using mesh spacings of 10^{-5} and 10^{-6}, respectively. However, the inset of Figure 2.18(b) shows that the difference is no longer monotone for the interval $\mu \in [0.299879, 0.299881]$ using a mesh spacing of 10^{-7}. This indicates that the map Π^2 is computed with an accuracy on the order of 10^{-7} in this regime. The parameter value at which there is a superstable periodic orbit can reasonably be located in the interval be-

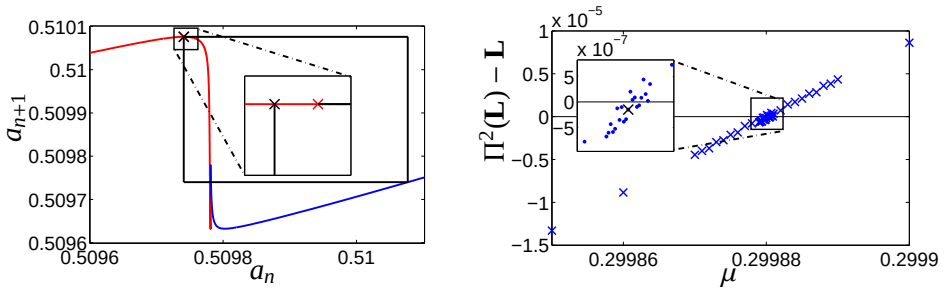

(a) $\mu = 0.29988$. (b) Distance from $\Pi^2(\mathbf{L}) = \mathbf{L}$.

Figure 2.18: (a) The return map for $\mu = 0.29988$. The cobweb diagram indicates the first two images of $\mathbf{L}$. The expanded view shows the critical point $\mathbf{L}$ and the second iterate $\Pi^2(\mathbf{L})$. (b) The difference in the a-coordinate $\Pi^2(\mathbf{L}) - \mathbf{L}$ for induced maps in the interval $\mu \in [0.29985, 0.2993]$. The inset shows that the difference becomes erratic on a scale of 10^{-7} in the mesh spacing of the μ parameter. The difference for $\mu = 0.29988$ is indicated by a black cross.

tween the first instance of $\Pi^2(\mathbf{L}) \in L_2$ and the last instance of $\Pi^2(\mathbf{L}) \in L_1$. These occur at $\mu = 0.2998801$ and $\mu = 0.2998805$, respectively. Therefore, the induced maps locate the bifurcation in the interval $\mu \in (0.29988, 0.2998806)$, which has length $O(10^{-7})$. In addition to $\Pi^2(\mathbf{L}) = \mathbf{L}$, we are able to locate other small period superstable orbits with an accuracy of $O(10^{-7})$ in parameter space. Thus, we expect to locate generic changes of kneading data to 6 consistent decimal places.

Bifurcations of MMOs in the full system can be estimated by iterating the induced maps. Figure 2.16 shows a PD bifurcation of a 2^1 MMO near $\mu = 0.29996$ in the $2^1 \to 3^1$ transition. Since a 2^1 MMO is a period-2 orbit in the induced map, we iterate the induced map to find fixed points of Π^2. We locate a pair of fixed points with derivatives $(\Pi^2)'$ close to -1 at $\mu = 0.299957$. Table 2.2 gives the slopes of Π^2 at the fixed points for two values of μ. Using a linear interpolation of the slopes of the fixed points, the maps predict a PD bifurcation at $\mu = 0.2999576$.

μ	$(\Pi^2)'$
0.299957	-0.9710
0.299958	-1.0199

Table 2.2: The slope of fixed points of the map Π^2 for two values of μ. The induced maps predict a PD bifurcation at $\mu = 0.2999576$.

An AUTO continuation of the stable 2^1 MMO at $\mu = 0.29995$ locates the same PD bifurcation at $\mu = 0.2999580$. The difference between the two predicted values of the bifurcation is approximately $4 \cdot 10^{-7}$. This residual is common for comparisons of bifurcations of small period MMOs of the full system with the corresponding periodic orbits of the induced map. We are able to successfully predict SN and PD bifurcations for small period MMOs of the full system by iterating the induced maps with an accuracy of $O(10^{-7})$.

2.4.4 Maps parametrized by c

When defining the induced map, we chose to use a parametrization of Γ_a by the a-coordinate. Since Γ_a is monotone in both a and c in a neighborhood of the forward invariant set, we could also define an induced map parametrized by the c-coordinate. We compare approximate induced maps for Γ_a parametrized by the a-coordinate with ones for Γ_a the c-coordinate as in Milik et. al. [79]. We denote these induced maps as *"a-maps"* and *"c-maps."*

When computing the c-maps, we follow the same procedure as described above: we compute a polynomial approximation to Γ_a, this time parametrized by c, and use AUTO to continue trajectories emanating from each branch of the induced map (i.e., one trajectory for each sector of rotation). Figures 2.19 and 2.20 were each calculated separately, parametrized by the labeled coordinate.

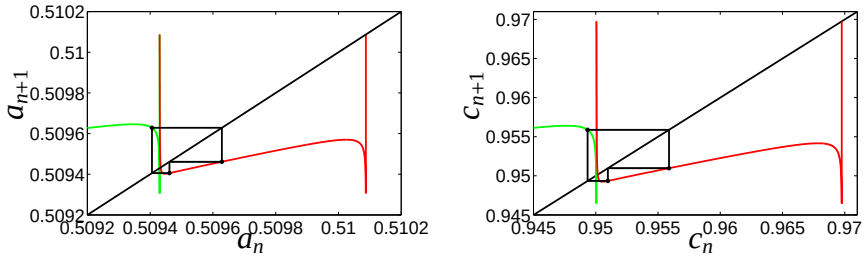

(a) a-map. (b) c-map.

Figure 2.19: Induced maps parametrized by both the a-coordinate and c-coordinate for $\mu = 0.29765$. Both maps admit a period-3 orbit.

We consider the two maps at the sets of parameters $(\epsilon, \mu) = (0.01, 0.299277)$ and $(\epsilon, \mu) = (0.01, 0.29765)$. The maps at these values have different numbers of laps: seven laps at $\mu = 0.29765$ and five laps at $\mu = 0.299277$. There is a stable $1^2(1^1)^2$ at $\mu = 0.29765$, and near $\mu = 0.299277$, there is a $2^1 1^1$ superstable orbit where the critical point **R** is period-3.

Figure 2.19 shows the induced a-map and c-map for $\mu = 0.29765$. The maps admit a stable period-3 orbit and have obvious similarities in appearance. We check the symbolic itineraries of the critical points. The sequences are identical:

$$a\text{-map} : \mathbf{L}R_2R_2L_2R_2R_2L_2R_2R_2L_2\ldots,$$

$$c\text{-map} : \mathbf{L}R_2R_2L_2R_2R_2L_2R_2R_2L_2\ldots,$$

$$a\text{-map} : \mathbf{R}L_2R_2R_2L_2R_2R_2L_2R_2R_2\ldots,$$

$$c\text{-map} : \mathbf{R}L_2R_2R_2L_2R_2R_2L_2R_2R_2\ldots.$$

We find that the same properties hold for the a-maps and c-maps at $\mu = 0.299277$. The itineraries of the critical points are identical. The maps appear to be related by an almost affine transformation. The insets of Figure 2.20 show

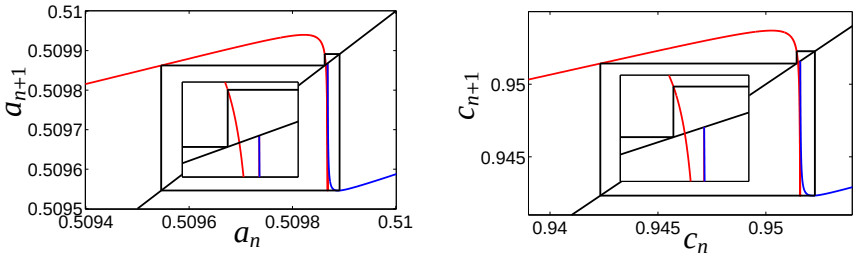

(a) a-map. (b) c-map.

Figure 2.20: The induced a-map and c-map for $\mu = 0.299277$. The inset of each map shows the intersection of the branches.

the intersection of the branches. The details of the maps in the boundary layer agree with one another: the relative position of the fixed point and the images of the periodic orbit are the same for both maps. Therefore, when $\epsilon > 0$, we find that the dynamics are described equally well by maps parametrized by a or c. For the remainder of the chapter, we consider only the induced a-maps.

2.4.5 Small period periodic orbits

Theorems of kneading theory state that the types of attractors of one-dimensional maps are largely determined by their kneading data. Globally attracting periodic MMOs are found in the five lap family when both **L** and **R** are attracted to the same periodic orbit. When this happens, one of the turning points has a critical value with the same symbolic sequence as the attracting orbit. Therefore, we search for stable MMOs by monitoring the trajectories of the two turning points of the induced maps of the five lap family. We predict that bistability might occur in this family but that regions of tristability would be undetectable.

Continuation of critical points and their iterates locates superstable orbits

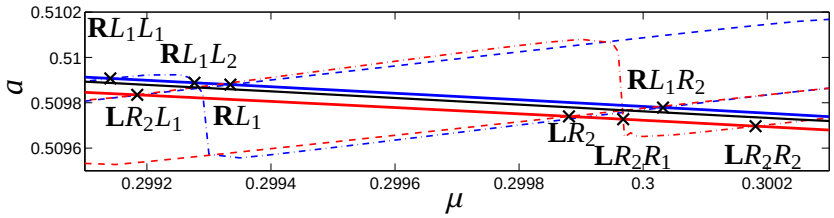

(a) Iterates of **L** and **R**.

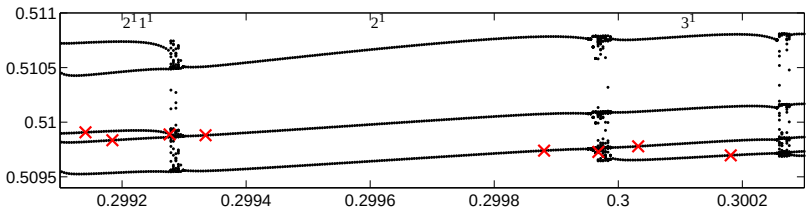

(b) Small period superstable orbits.

Figure 2.21: (a) Let $\mathbf{P} \in \{\mathbf{L}, \mathbf{R}\}$. $\mathbf{P}$, $\Pi^2(\mathbf{P})$, and $\Pi^3(\mathbf{P})$ are indicated by solid, dotted, and dashed-dotted curves, respectively. Returns of $\mathbf{R}$ ($\mathbf{L}$) are shown in blue (red). Intersections $\mathbf{P} = \Pi^i(\mathbf{P})$ give the location of superstable orbits. The black curve indicates the a-coordinate of the fixed point $\mathbf{C}$. (b) The superstable orbits superimposed on the bifurcation diagram for $\mu \in [0.2991, 0.3003]$. Three bands of stable MMOs are labeled.

and stable bands of MMOs. Let $\mathbf{P} \in \{\mathbf{R}, \mathbf{L}\}$ be a critical point. A superstable orbit is created whenever $\Pi^i(\mathbf{P}) = \mathbf{P}$ for $i \geq 1$. We show that period-2 and period-3 superstable orbits without canard segments generate wide bands of stable MMOs. Superstable periodic orbits containing canard segments generate a thin stable band and generally lose stability quickly.

Figure 2.21(a) indicates the existence of one period-2 and three period-3 superstable orbits for each of $\mathbf{R}, \mathbf{L}$ in the five lap family: the orbits are marked with black crosses, and the signature of each orbit is given. The returns of $\mathbf{L}$ and $\mathbf{R}$ are shown in bold red and blue lines, respectively. Second returns $\Pi^2(\mathbf{P})$ are shown in dashed lines, and third returns $\Pi^3(\mathbf{P})$ are shown in dotted-dashed lines. The iterates of $\mathbf{P}$ are computed from twenty-five evenly spaced induced maps for $\mu \in [0.2991, 0.3003]$ and four evenly spaced return maps in each of the

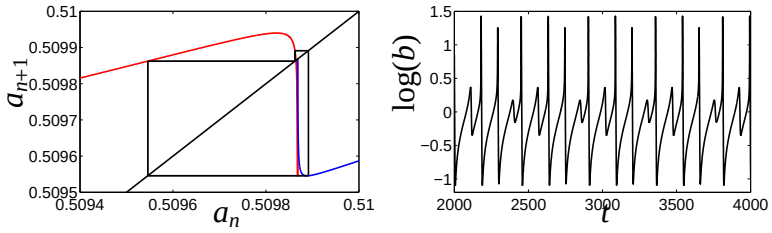

(a) $\mu = 0.299277$.

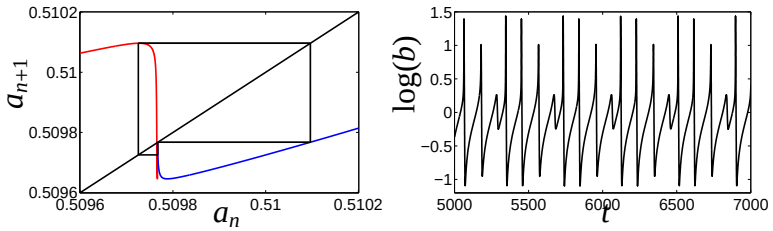

(b) $\mu = 0.299972$.

Figure 2.22: The induced map and time series near a superstable MMO for two μ values listed in Table 2.3.

intervals $[0.29926, 0.29929]$ and $[0.29996, 0.29999]$. The two smaller intervals are necessary to resolve the large gradients in $\Pi^3(\mathbf{P})$. The superstable orbits are also indicated on the bifurcation diagram in Figure 2.21(b). Each wide stable band in the bifurcation diagram contains a small period superstable orbit. A pair of superstable orbits lie in the $2^1 1^1$, 2^1, and 3^1 bands. Each pair of superstable orbits in the wide bands has the same signature and can be continued into one another. For example, the stable period-2 orbit $R_2 L_1$ at $\mu = 0.2996$ may be continued into the superstable $\mathbf{L}R_2$ by increasing μ or into the $\mathbf{R}L_1$ by decreasing μ. Table 2.3 gives the approximate location and the signature of the eight superstable orbits labeled in Figure 2.21(a). Figure 2.22 shows the induced map and the time series for each of the superstable orbits.

Two of the period-3 orbits do not lie in wide bands of stable MMOs: the $2^1 1^1$ orbit near $\mu = 0.299277$ is located in the $2^1 1^1 \to 2^1$ transition, and the 3^1 orbit near $\mu = 0.299972$ lies in the $2^1 \to 3^1$ transition. Red crosses in Figures 2.23 and 2.16

Orbit	μ	Itinerary	Signature
$\Pi^2(\mathbf{R}) = \mathbf{R}$	0.299335	$\mathbf{R}L_1$	2^1
$\Pi^3(\mathbf{R}) = \mathbf{R}$	0.299141	$\mathbf{R}L_1L_1$	$2^1 1^1$
	0.299277	$\mathbf{R}L_1L_2$	$2^1 1^1$
	0.300032	$\mathbf{R}L_1R_2$	3^1
$\Pi^2(\mathbf{L}) = \mathbf{L}$	0.299880	$\mathbf{L}R_2$	2^1
$\Pi^3(\mathbf{L}) = \mathbf{L}$	0.299184	$\mathbf{L}R_2L_1$	$2^1 1^1$
	0.299972	$\mathbf{L}R_2R_1$	3^1
	0.300181	$\mathbf{L}R_2R_2$	3^1

Table 2.3: Locations and signatures of small period superstable orbits in the five lap family.

(respectively) give the locations of the superstable orbits in their induced maps. Both of these orbits generate a thin band of stable MMOs. Figure 2.23 shows that the superstable orbit loses stability quickly, leading to a chaotic attractor as μ increases. Figure 2.16 shows a thin band of 3^1 MMOs near $\mu = 0.299972$. The 3^1 MMO appears to undergo a PD cascade and loses stability. Numerical integration near this orbit finds that the 3^1 MMO is stable in the interval $\mu \in (0.2999719, 0.2999729)$. Figure 2.22 shows the induced maps and the time series for the superstable orbits at $\mu = 0.299277$ and $\mu = 0.299972$. The time series for both superstable orbits have canard segments. Note that $\Pi^2(\mathbf{R}) \approx \mathbf{C}$ for $\mu = 0.299277$ and $\Pi^2(\mathbf{L}) \approx \mathbf{C}$ for $\mu = 0.299972$. One of the hallmarks of the induced maps in the regions between stable MMOs is that the trajectory of at least one critical point passes through the canard region near $\mathbf{C}$.

In a family of one-dimensional maps, all periodic orbits are created through saddle-node or period doubling bifurcations. We use kneading theory to investigate small period orbits in the $2^1 1^1 \to 2^1$ transition over the parameter interval $\mu \in (0.29926, 0.2993)$. A kneading theory calculation establishes that all periodic itineraries of period less than ten for $\mu = 0.2993$ are also present at $\mu = 0.29926$. This prompts us to conjecture that new periodic orbits in this transition are all

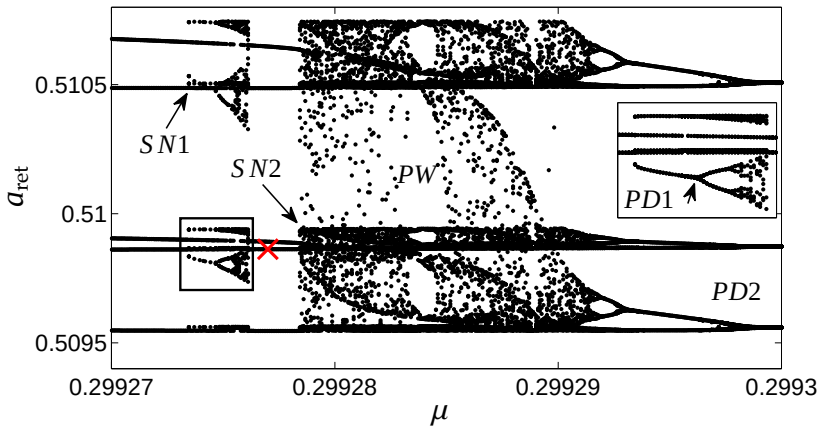

Figure 2.23: The bifurcation diagram of the $2^1 1^1 \rightarrow 2^1$ transition. Two saddle-node and two period doubling bifurcations are labeled. A period-8 periodic window near $\mu = 0.299284$ is labeled PW. The a-coordinate of the critical point $\mathbf{L}$ of the period-3 superstable orbit $\Pi^3(\mathbf{L}) = \mathbf{L}$ at $\mu = 0.299277$ is indicated by a black cross. An expanded view of the parameter interval containing $SN1$ and $PD1$ is shown.

created as μ decreases.

The bifurcations of small period periodic orbits shape the gross features of the bifurcation diagram. Table 2.4 lists the four period-3 orbits that do not contain the symbol L_3 and are admissible at $\mu = 0.29926$ but not at $\mu = 0.2993$. We ignore those sequences with the symbol L_3 because they are difficult to numerically detect in the full system. Table 2.4 shows that the order in which the period-3 orbits are destroyed is consistent with the ordering of the symbolic itineraries. This is directly related to the monotonicity of the kneading data over the interval of the μ parameter in which the bifurcations take place.

#	Itinerary	Interval of Destruction
1	$L_1L_2R_2$	(0.299277, 0.299278)
2	$L_1L_2R_1$	(0.299278, 0.299279)
3	$L_1L_2L_2$	(0.299281, 0.299282)
4	$L_1R_1L_2$	(0.299289, 0.299290)

Table 2.4: Periodic orbits of length-3 that are destroyed for $\mu \in (0.29926, 0.2993)$ and the interval in which they are destroyed.

2.4.6 Bifurcations in the $2^1 1^1 \to 2^1$ transition

Figure 2.23 labels four bifurcations in the $2^1 1^1 \to 2^1$ transition: two saddle-node bifurcations and two period doubling bifurcations. These four bifurcations are related to bifurcations of small period orbits. We describe features of the dynamics related to these bifurcations, namely bistability, a saddle-node bifurcation to chaos, and the period doubling cascade to a stable 2^1 MMO. We also investigate a thin periodic window labeled *PW* in Figure 2.23.

The first feature of the transition we investigate is an interval of bistability contained in the interval $\mu \in (0.299273, 0.299278)$. This interval contains two stable MMOs: a period-3 $2^1 1^1$ MMO that exists at the beginning of the transition and a period-4 $2^1(1^1)^2$ MMO born at a saddle-node bifurcation (*SN*1, Figure 2.23). A view of this region is expanded and plotted in the inset of Figure 2.23. Once created, $2^1(1^1)^2$ MMO immediately undergoes a period doubling cascade (*PD*1, Figure 2.23).

The kneading data predict the bistability and show that the $2^1(1^1)^2$ MMO band contains a superstable orbit with the itinerary $R_2L_1L_2\mathbf{L}$ for some $\mu \in (0.299273, 0.299274)$. The kneading data of the critical point $\mathbf{L}$ for the endpoints

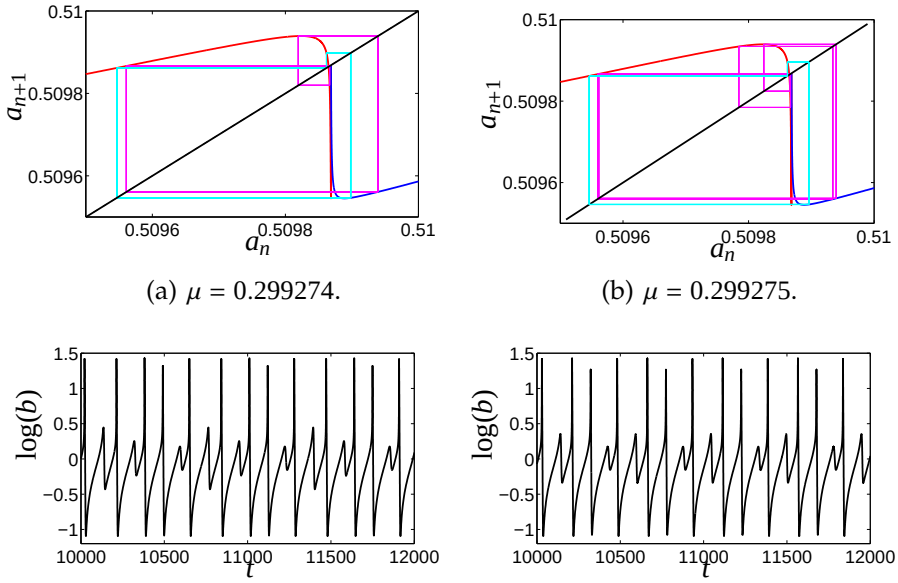

(a) $\mu = 0.299274$. (b) $\mu = 0.299275$.

(c) $\mu = 0.299274$. (d) $\mu = 0.299274$.

Figure 2.24: (a) Bistability at $\mu = 0.299274$. The induced map shows the limit set of **L** and **R** in magenta and cyan, respectively. **L** is attracted to a period-4 orbit and **R** is attracted to a period-3 orbit. (b) Bistability at $\mu = 0.299275$. **L** is attracted to a period-8 orbit and **R** is attracted to a period-3 orbit. (c)-(d) Two stable periodic orbits at $\mu = 0.299274$: a $2^1(1^1)^2$ MMO (c) and a $2^1 1^1$ MMO (d).

of this interval are given by

$$\mu = 0.299273 : \mathbf{L}R_2L_1L_2L_2\ldots,$$

$$\mu = 0.299274 : \mathbf{L}R_2L_1L_2L_1\ldots.$$

These kneading data show that $\Pi^4(\mathbf{L}) = \mathbf{L}$ for some $\mu \in (0.299273, 0.299274)$. Figure 2.24(a) and (b) show that the critical point **R** remains attracted to the period-3 orbit $L_1L_2R_2$ over the interval of bistability. Figure 2.24(c) and (d) show the time series for the period-3 and period-4 stable orbits at $\mu = 0.299274$. The superstable orbit perturbs to periodic orbits with the itineraries $[R_2L_1L_2L_2, R_2L_1L_2L_1]$. Both of these period-4 orbits are admissible at $\mu = 0.299274$, while neither is

admissible at $\mu = 0.299273$. The kneading data predict that the period-4 orbit arises from the saddle-node bifurcation $SN1$ for some $\mu \in (0.299273, 0.299274)$.

The bifurcation $SN1$ can be located by checking the number and the stability of the fixed points of the iterated map Π^4. Figure 2.25 shows Π^4 for three values of μ. Figure 2.25(a)-(b) show that four new fixed points of Π^4 are created in a saddle-node bifurcation that occurs for some $\mu \in (0.299273, 0.299274)$. Figure 2.25(b) shows the tangent line to a fixed point near $a_n = 0.5098$ at $\mu = 0.299274$. Figure 2.25(a) shows that no fixed points exist in this region of the map for $\mu = 0.299273$. An AUTO continuation of the $2^1(1^1)^2$ orbit at $\mu = 0.299274$ locates $SN1$ at $\mu = 0.2992735$. Although estimation of the location of $SN1$ using the induced maps is difficult, the bifurcations predicted by iterating the induced maps are consistent with those found in the full system.

The kneading data and the iterated maps show that there is period doubling bifurcation in the interval $\mu \in (0.299274, 0.299275)$. At $\mu = 0.299274$, the critical point **L** is attracted to the period-4 orbit $R_2L_1L_2L_1$. However, at $\mu = 0.299275$, **L** is attracted to the period-8 orbit $R_2L_1L_2L_1R_2L_1L_2L_2$ (see Figure 2.24(b)). This indicates that the period-4 orbit which attracts **L** has period doubled at $PD1$ for some $\mu \in (0.299274, 0.299275)$. Figure 2.25(c) shows the tangent line to the same fixed point shown in Figure 2.25(b). Table 2.5 gives the slopes of these tangent lines. The slopes pass through -1, indicating the existence of a period doubling bifurcation in the interval $(0.299274, 0.299275)$. Using a linear interpolation of the slope at the fixed points, the iterated maps predict the bifurcation $PD1$ at $\mu = 0.2992748$. An AUTO continuation of the stable $2^1(1^1)^2$ MMO at $\mu = 0.299274$ finds $PD1$ at $\mu = 0.2992747$. Like the PD bifurcation located above, the difference in the two predicted values is approximately 10^{-7}.

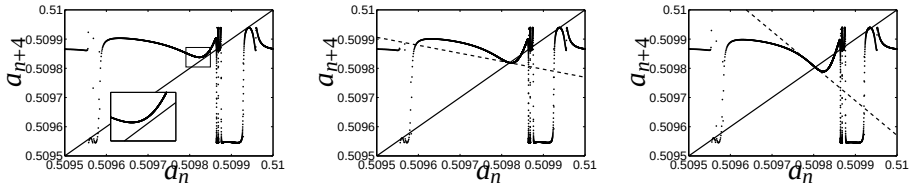

(a) Π^4 at $\mu = 0.299273$. (b) Π^4 at $\mu = 0.299274$. (c) Π^4 at $\mu = 0.299275$.

Figure 2.25: Π^4 for three μ values show evidence of a saddle-node bifurcation $SN1$ and PD bifurcation $PD1$. (a) An expanded view near $a = 0.5098$ shows there are no fixed points of Π^4 in this neighborhood. (b)-(c) Tangent lines to fixed points of the iterated maps are shown in dotted black. The slopes tangent to the iterated maps for the fixed points shown are given in Table 2.5. The induced maps predict an SN bifurcation for some $\mu \in (0.299273, 0.299274)$ and a PD bifurcation for some $\mu \in (0.299274, 0.299275)$.

μ	$(\Pi^4)'$
0.299274	−0.2735
0.299275	−1.1869

Table 2.5: Slopes of the iterated induced maps Π^4 at a fixed point for two values of μ. The maps predict a period doubling bifurcation at $\mu = 0.2992748$.

A second feature of the $2^1 1^1 \to 2^1$ transition that we investigate is the sudden expansion of the periodic attractor to chaotic behavior near $\mu = 0.299278$. The expansion of the attractor is the result of a pair of period-3 orbits annihilating each other in a saddle-node bifurcation. The first eleven symbols of the kneading data for $\mu = 0.299278$ and $\mu = 0.299279$ are given by the following:

$$0.299278 : \mathbf{L}R_2L_1L_2L_1L_2L_2L_2R_2L_1L_2L_2\ldots,$$

$$0.299278 : \mathbf{R}L_1L_2R_1L_1L_2R_1L_1L_2R_1L_1L_2\ldots,$$

$$0.299279 : \mathbf{L}R_2L_1R_1L_1R_2L_1L_2L_1R_2L_1L_2\ldots,$$

$$0.299279 : \mathbf{R}L_1L_2R_1L_1L_2R_1L_1L_2R_1L_1R_1\ldots.$$

The periodic orbit $L_1L_2R_1$ satisfies the admissibility conditions (2.11) at $\mu = 0.299278$ but not at $\mu = 0.299279$. This suggests that the period-3 orbit is annihilated in a saddle-node bifurcation for some $\mu \in (0.299278, 0.299279)$. Using numerical integration, we find the $2^1 1^1$ MMO is stable up to $\mu = 0.2992786$. We also find intermittency and chaos in numerically integrated time series for $\mu \in (0.2992787, 0.299279)$.

Figure 2.26(a) and (b) show the induced maps for $\mu = 0.299278$ and $\mu = 0.299279$. Figure 2.26(a) shows the period-3 orbit for $\mu = 0.299278$, in black. At $\mu = 0.299279$, the trajectories of both critical points appear chaotic; neither critical point approaches a periodic attractor. Figure 2.26(b) shows the limit set for **L** and **R** in magenta and cyan. This is consistent with the annihilation of the period-3 orbit by a saddle-node bifurcation.

Figure 2.26(c) and (d) shows the iterated maps Π^3 for $\mu = 0.299278$ and $\mu = 0.299279$. An expanded view of the map shows a pair of fixed points near $a_n = 0.50955$ in the inset of Figure 2.26(c) for $\mu = 0.299278$. Figure 2.26(d) shows that no fixed points exist in this region at $\mu = 0.299279$, indicating the existence of the saddle-node bifurcation $SN2$. An AUTO continuation of the stable $2^1 1^1$ MMO at $\mu = 0.299277$ detects the saddle node bifurcation $SN2$ at $\mu = 0.2992785$. The symbolic dynamics and the iteration of the return maps are consistent with both numerical integration and continuation.

The third feature of the $2^1 1^1 \to 2^1$ transition that we investigate is a periodic window near $\mu = 0.299284$. The periodic window is marked PW in Figure 2.23. The induced map at $\mu = 0.299284$ has a globally attracting period-8 orbit at $\mu = 0.299284$. The kneading data for the critical point **L** at $\mu = 0.299283$ and

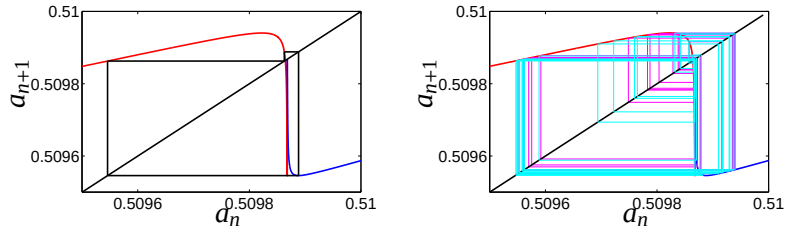

(a) $\mu = 0.299278$. (b) $\mu = 0.299279$.

(c) Π^3 at $\mu = 0.299278$. (d) Π^3 at $\mu = 0.299279$.

Figure 2.26: (a) The induced map at $\mu = 0.299278$. The limit set of both critical points is shown in black. (b) The induced map at $\mu = 0.299279$. The limit sets of **L** and **R** are shown in magenta and cyan, respectively. (c) The iterated map Π^3 at $\mu = 0.299278$. The inset shows two fixed points near $a = 0.50955$. (d) The iterated map Π^3 at $\mu = 0.299279$. The inset shows there are no fixed points near $a = 0.50955$, indicating the existence of a saddle-node bifurcation.

$\mu = 0.299284$ are given by

$$0.299283 : \mathbf{L}R_2L_1R_1L_1R_1L_1L_2L_2\ldots,$$

$$0.299284 : \mathbf{L}R_2L_1R_1L_1R_1L_1L_2L_1\ldots.$$

The eighth iterate of the critical point **L** is mapped into itself $\Pi^8(\mathbf{L}) = \mathbf{L}$ for some $\mu \in (0.299283, 0.299284)$. Figure 2.27(a) shows the induced map at $\mu = 0.2992839$ and the $R_2L_1R_1L_1R_1L_1L_2\mathbf{L}$ period-8 orbit, shown in black. The two canard points of the orbit, one on each branch, are indicated by black crosses. The canards are also reflected in the time series, which is shown in Figure 2.27(b). There are canard segments in both 1^1 segments and 1^0 segments of the orbit, which are indicated by red crosses. There is evidence that this window

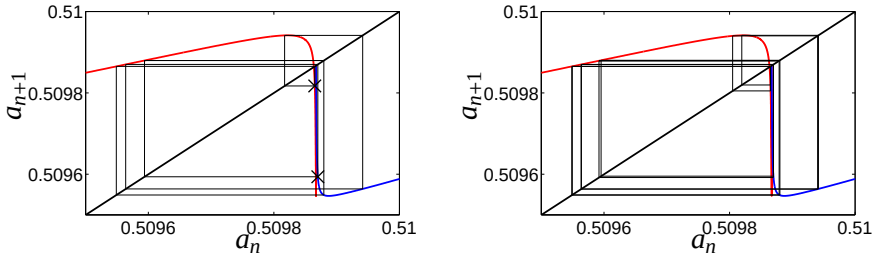

(a) $\mu = 0.2992839$.

(b) $\mu = 0.299284$.

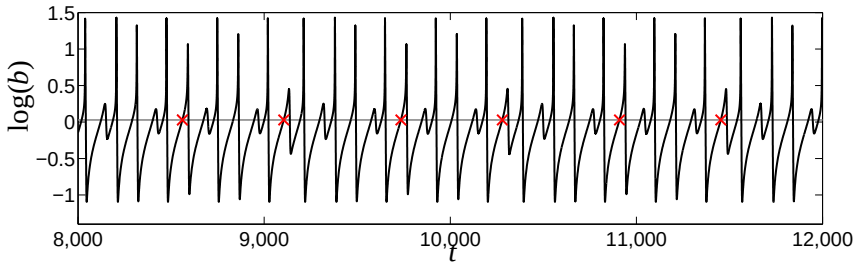

(c) $\mu = 0.2992839$.

Figure 2.27: (a) The induced map at $\mu = 0.2992839$ and its globally attracting period-8 orbit, shown in black. Two points of the period-8 orbit that lie in the canard region are marked with black crosses. (b) The induced map at $\mu = 0.2992839$ and its globally attracting period-16 limit set, shown in black. (c) The time series of the period-8 orbit at $\mu = 0.2992839$ computed by forward integration. The b-coordinate of the cross section Σ is indicated by a gray line. The canards marked in (a) are indicated by red crosses.

is destroyed by a period doubling cascade. Figure 2.27(c) shows the induced map for $\mu = 0.299284$ and the limit set which attracts both critical points. The limit set is a period-16 orbit, which is period-doubled from the stable period-8 orbit at $\mu = 0.2992839$.

The last feature that we investigate is a period doubling cascade to a stable 2^1 MMO. Figure 2.28 shows the induced maps and their globally attracting periodic limit set for both $\mu = 0.299292$ and $\mu = 0.299293$. At $\mu = 0.299292$, the globally stable MMO is the period-8 orbit $L_1R_1L_1R_2L_1R_1L_1R_1$. This orbit un-

μ	$(\Pi^4)'$
0.299292	−1.4535
0.299293	−0.9374

Table 2.6: Slopes of the iterated induced maps Π^4 at a fixed point for two values of μ. The maps predict a period doubling bifurcation at $\mu = 0.2992929$.

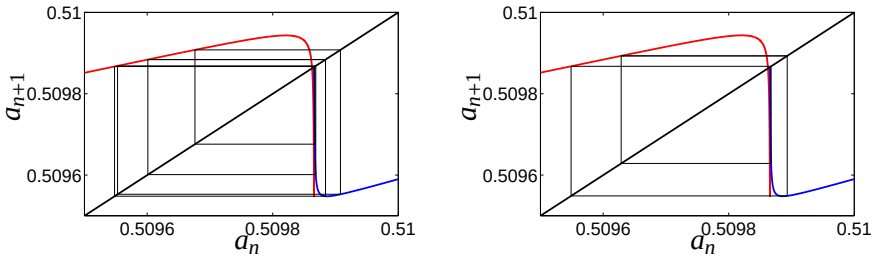

(a) $\mu = 0.299292$. (b) $\mu = 0.299293$.

Figure 2.28: (a) Globally stable period-8 orbit at $\mu = 0.299292$. (b) Globally stable period-4 orbit at $\mu = 0.299293$.

dergoes two period doubling bifurcations to a period-2 orbit L_1R_1 in the interval $(0.299292, 0.2993)$. At $\mu = 0.299293$, the global attractor is a period-4 orbit $L_1R_1L_1R_2$. Table 2.6 gives the slopes of a pair of fixed points of the iterated map Π^4 for the two values of μ. Using a linear interpolation of the slopes, the induced maps predict a period doubling bifurcation at $\mu = 0.2992929$. An AUTO continuation of the 2^12^1 orbit at $\mu = 0.299295$ finds the period doubling bifurcation at $\mu = 0.2992928$. The error in the predicted value is order $O(10^{-7})$.

The period-4 orbit $L_1R_1L_1R_2$ is stable for $\mu \in (0.299293, 0.299298)$. The global attractor for the interval $\mu \in (0.299293, 0.299295)$ is the period-4 orbit $L_1R_1L_1R_2$. However, for some $\mu \in (0.299295, 0.299296)$, the period-4 orbit passes through $\mathbf{R}$ to become the superstable orbit $L_1R_1L_1\mathbf{R}$. The itinerary of the orbit becomes the sequence $L_1R_1L_1R_1$ after the kneading transition. We list the kneading data for

μ	$(\Pi^2)'$
0.299297	−1.0832
0.299298	−0.9891

Table 2.7: Slopes of the iterated induced maps Π^2 at a fixed point for two values of μ. The maps predict a period doubling bifurcation at $\mu = 0.2992979$.

the critical point **R**:

$$0.299295 : \mathbf{R}L_1R_1L_1R_2L_1R_1L_1R_2\ldots,$$

$$0.299296 : \mathbf{R}L_1R_1L_1R_1L_1R_1L_1R_1\ldots.$$

This change in the kneading data allows the period-2 orbit L_1R_1. However, the period-2 orbit with this signature is unstable. The global attractor at $\mu = 0.299296$ is the period-4 orbit with signature $L_1R_1L_1R_1$. Although there is no change in the kneading data for $\mu \in (0.299296, 0.2993)$, there is a period doubling bifurcation where the period-4 orbit period halves into the period-2 orbit L_1R_1. Therefore, we must iterate the induced maps to determine the locations of the bifurcations. Figure 2.29(a) and (b) show the stable period-4 orbits for the two values of μ. Figure 2.29(c) shows the stable period-2 orbit at $\mu = 0.299299$. Table 2.7 lists the slopes of the iterated map Π^2 at a pair of fixed points for two values of μ. Using a linear interpolation of the slopes, the induced maps predict the PD bifurcation $PD2$ at $\mu = 0.2992979$. An AUTO continuation of the 2^1 MMO at $\mu = 0.2993$ locates $PD2$ at $\mu = 0.2992982$. Again, the difference between the predicted value and the actual value of the bifurcation is $O(10^{-7})$.

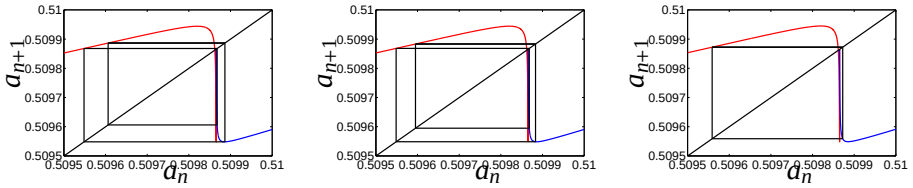

(a) $\mu = 0.299295$. (b) $\mu = 0.299296$. (c) $\mu = 0.299299$.

Figure 2.29: (a) The induced map and globally attracting period-4 orbit with signature $L_1R_1L_1R_2$ at $\mu = 0.299295$. (b) The induced map and globally attracting period-4 orbit with signature $L_1R_1L_1R_1$ at $\mu = 0.299296$. (c) The induced map at $\mu = 0.299299$ and the globally attracting period-2 orbit with signature L_1R_1.

2.5 Discussion

This chapter continues the investigation of the autocatalator, a three-dimensional vector field that models mixed-mode oscillations (MMOs) in chemical reactions. Milik and coworkers [79, 80] proposed the use of singular perturbation theory and reduction to one-dimensional maps for the investigation of this model. We have carried out this process in much greater detail and computed one-dimensional induced maps for this system. We highlight the differences between return maps and induced maps of the system for cross sections that extend from the fold curve of the critical manifold. These cross sections contain some points that return with small amplitude loops that do not undergo the extreme attraction associated with trajectories that return from large amplitude loops along the attracting slow manifold of the system. As a result, the return map displays a "mixed rank" character: in one region it is nearly singular and rank-1, while in another region, it is far from singular. The induced maps are constructed by iterating returns until they pass through the region where the return map is nearly singular. The two regions in the domain of the return map are separated by a thin strip of the cross section whose trajectories flow along

the repelling slow manifold and contain canard segments. We used the boundary value solver in the program AUTO to compute the return map in this strip. We found previously unobserved complexity of the return and induced maps in these regions. In particular, the induced maps have more turning points than the minimal number required to create continuous extensions across these regions. Moreover, the images of the canard segments are longer than the gaps between the images of segments without canards. The added complexity of the maps affects aspects of the chaotic behavior one finds in this system, a topic that has not been pursued here.

The construction of the induced maps is a multistep process, each step involving approximations. We investigated the accuracy of these approximations and carefully compared predictions based upon analysis of the induced maps with numerical calculations of periodic orbits and their bifurcations in the full autocatalator model. The kneading theory upon which our analysis is based relies heavily upon the piecewise monotone character of one-dimensional maps. We found that the piecewise monotonicity of the induced maps breaks down on a scale comparable to 10^{-7} despite computations of trajectories that are several orders of magnitude more accurate than that. The principal limitation associated with this accuracy is that only periodic MMOs of small periods can be readily computed. It is quite possible that improved methods for locating the slow manifolds of the system and computing the returns for trajectories on these manifolds would produce higher numerical accuracy. Nonetheless, these improvements would likely enable only a modest extension of those periodic MMOs that could be computed with confidence.

The constraints of kneading theory allow us to identify families of periodic

MMOs. Numerically, we located small intervals of parameter values containing bifurcations of specific periodic orbits with accuracy commensurate with the accuracy of the computation of the induced maps themselves. These computations were compared with continuation calculations using AUTO that located the corresponding bifurcations of periodic orbits in the autocatalator flow. The agreement between these two sets of bifurcation calculations was excellent, again comparable to the accuracy of computing the induced map itself. Thus, we conclude that the reduction of this slow-fast vector field to a one-dimensional induced map captures the dynamics of the system quantitatively as well as qualitatively.

The relationship between chaotic behavior in slow-fast systems and one-dimensional reductions has been explored by Guckenheimer, Wechselberger and Young [50], relying upon the theory of Henon-like maps [11, 121]. This work gives substantial insight and makes predictions about the dynamical behavior of the autocatalator in the transition regions of parameter space between the regions of stable periodic MMOs. Due to the limited accuracy of our computed induced maps, we have not pursued quantitative comparisons of the chaotic attractors of induced maps and continuous flows of the autocatalator.

CHAPTER 3

A SHORT HISTORY OF THE BELOUSOV-ZHABOTINSKII REACTION

3.1 Motivation

The Belousov-Zhabotinskii (BZ) reaction is one of the most widely studied chemical reactions. The BZ reaction is characterized by the oxidation and bromination of malonic acid ($CH_2(COOH)_2$, usually denoted MA) by a metal-ion catalyst, often Cerium, ferroin, or manganese, in a sulfuric acid (H_2SO_4) solution. The source of the bromate ions is typically a potassium or sodium bromate salt ($KBrO_3$ or $NaBrO_3$), and the source of metal-ions is typically cerous sulfate ($Ce_2(SO_4)_3$), although both ferroin sulfate ($FeSO_4$) and manganese sulfate ($MnSO_4$) are also used. Belousov [9] and Zhabotinskii [124] discovered that after a short induction period, the reaction enters a regular oscillatory regime in a homogeneous (closed) batch reaction. This oscillatory regime can last for several hours before meeting its thermodynamic end in an equilibrium state. The oscillations of the Cerium catalyst are nearly periodic, with each cycle indistinguishable from the last, however, there is a steady buildup of the bromate ion (BrO_3^-) concentration. These oscillations generated much interest in both the experimental and modeling communities.

Sørenson discovered [110] that robust and complex oscillatory states are possible if the reaction takes place in a continuous-flow stirred tank reactor (CSTR). In a CSTR, reactants are continuously injected into the tank, while an equal amount of the well-mixed solution is removed to preserve volume. The injection of reactants keeps the chemical system far from equilibrium, making complex periodic and aperiodic behaviors possible. The flow rate of the feed re-

actants is used as the primary experimental bifurcation parameter. Experiments show that the BZ reaction exhibits complex oscillations at both high and low flow rates of the reactants. The CSTR-BZ reaction exhibits a stunning variety of behavior, including steady state, simple periodic orbits, mixed-mode oscillations (MMOs), alternating periodic and aperiodic sequences, excitability, invariant tori, bistability, intermittency, crisis bifurcations, and several well-known routes-to-chaos. Advances in experimental techniques and the formulation of complex models of the reaction elucidated the chemical mechanisms generating the complex behavior. Attempts to model individual phenomena observed in the BZ reaction through simple nonlinear models also helped to develop the field of nonlinear dynamics.

In the next two sections of this chapter, we outline some of the major results in experimental BZ chemistry and efforts to model the reaction and the observed phenomena in a CSTR. For the remainder of the chapter, the BZ reaction is assumed to take place in a CSTR. There are other contexts in which to study the BZ reaction, including the spatial patterns observed when the BZ reaction takes place in a thin unstirred dish, coupled BZ reactors, electrochemically coupled BZ reactors, and forced BZ reactors. We do not outline this work. See [105] for an introduction to these topics. The exposition in the next two sections closely follows that of Scott [105], Zhang, Györgyi, and Peltier [126], and Györgyi and Field [54].

3.2 Experimental results

3.2.1 Experimental conditions

The CSTR reactors used in BZ experiments typically have volumes of 30-40 mL, although some are as small as 2-3 mL and some are as large as 200 mL. The geometry of the reactors can vary but most experiments have been conducted in cylindrical reactors. In order to keep the temperature of the apparatus constant, the reactors are placed in a thermally controlled bath. To ensure the homogeneity of the solution, it is mixed vigorously at 500-2000 rpm. The feed reactants can either be premixed (mixed-feed) or injected individually. Usually there are three inflow feeds containing solutions of malonic acid, bromate ions, and Cerium. The earliest pumping mechanisms controlling the flow rate could not operate at sufficiently low flow rates. As a result, early studies only investigate high flow rate complexity. As pumping control increased, low flow rate complexity could be investigated. For most studies, high and low flow rates regimes are determined by the rates relative to a regime of relaxation oscillations (called the P_1 regime by many studies). Low (high) flow rate complexity is identified by decreasing (increasing) the flow rate from the P_1 regime. Oscillations of the reaction are monitored by either a bromide-ion-selective electrode, which is sensitive to the log of the bromide ion concentration, or a platinum electrode, which measures the redox potential of the system. The platinum electrode measurement is approximately proportional to the quantity $\log(O/R)$, where O and R are the oxidized and reduced forms of the catalyst.

Experiments are generally performed by varying the flow rate (or residence time) while keeping the feed concentrations constant and observing the result-

ing oscillations. The residence times τ are found by dividing the tank volume by the flow rate. Table 3.1 lists the feed concentrations, the concentration of the sulfuric acid medium, the temperature at which the experiments are performed, and the observed experimental behavior. For each flow rate, measurements are taken after a transient time of approximately ten residence times.

We identify five regimes of behavior in the BZ reaction: steady states at both very high and very low flow rates, complexity as the flow rate is increased (decreased) from the low (high) flow rate steady state, and a regime of relaxation oscillations at intermediate flow rates. We interpret the low and high flow steady states as perturbations of the zero flow rate and infinite flow rate, respectively. At zero flow rate, the system is a batch reaction and ends in a thermodynamic equilibrium. At infinite flow rate, the concentration of the solution is identical to the feed concentration. Therefore, the low and high flow rate branches of equilibria are called the *thermodynamic* and *flow branches*.

3.2.2 High flow rate complexity

The first observation of complex oscillatory patterns in a CSTR reactor was reported by Sørenson [110, 111], who observed MMOs with trains of large amplitude oscillations (LAOs) followed by trains of small amplitude oscillations (SAOs). For some experimental parameter values, the amplitude of the SAOs decrease below an observable threshold, then increase before the next train of large amplitude oscillations. Sørenson showed that these MMOs can be found in reactions catalyzed by both Cerium and manganese. Marek and Svobodoba [75] observed similar trajectories, and showed that they deform by varying both

the flow rate and $KBrO_3$ mixed-feed concentration.

Although Sørenson described these oscillations as "bursting patterns," we follow the terminology introduced by Janz, Vanecek, and Field [66], who called these trajectories "double composite oscillations" and refer to them as "double composite MMOs." The term was used by Janz and coworkers to reflect the pattern of nearly constant amplitude LAOs followed by nearly constant amplitude SAOs. We use this terminology to reflect the qualitative difference between these double composite MMOs with the typical 1^n MMOs which have a distinct hourglass shape. We stress that the difference is purely qualitative; in the next chapter we see that both of these behaviors are consistent with oscillations near a dynamic Hopf bifurcation. However, when modeling the two behaviors, different approaches are taken because the double composite MMOs are often preceded by a subcritical Hopf bifurcation, while the hourglass MMOs are often preceded by a supercritical Hopf bifurcation.

Graziani, Hudson, and Schmitz [40] also investigated oscillations at high flow rates. They observed relaxation oscillations at intermediate flow rates. As the flow rate was increased, they observed a 1^n nearly homoclinic orbit: long intervals of quiescent behavior are followed by SAOs of increasing amplitude before each large spike. The authors showed that these oscillations are terminated by a "hard" transition. This collapse of the periodic orbit to steady state may be the result of a subcritical Hopf bifurcation. However, in many studies, small amplitude periodic orbits are observed after 1^n MMOs. If the flow rate resolution is too large, small amplitude periodic orbits may not be observed. Evidence was also presented that the criticality of the Hopf bifurcation may be affected by the flow rate of the bromate ion feed. As the bromate ion feed flow rate was in-

creased, the interspike time between the 1^n orbits increased until LAOs were no longer observed, at which point only small amplitude oscillations are observed. Most interestingly, a time series in Figure 3 of [40] appears to show a torus. This issue was not explored further.

Another study by the same group [103] reported the first evidence of aperiodicity at high flow rates. The authors presented trajectories as the flow rate was increased from 1.0 to 7.0 mL/min. The following behaviors were observed: relaxation oscillations, a 1^1 trajectory, small amplitude oscillations, and steady state at the highest flow rates. Several aperiodic time series were shown for flow rates between 3.0 and 4.5 mL/min. The authors asserted that the aperiodic time series are evidence of chaos in the BZ reaction. They reported that oscillations are terminated at a supercritical Hopf bifurcation. Double composite MMOs were not reported; however, the mixed-feed and sulfuric acid concentrations differed significantly from the study [111].

Remark: The alternation of periodic and aperiodic states is sometimes referred to in the literature as *periodic-chaotic sequences*, or *PCS*. We avoid using this term to describe generic sequences of periodic and aperiodic behavior because of the debate surrounding the existence of chaos in the BZ reaction, particularly at high flow rates. Instead, we use the phrase *periodic and aperiodic sequences* or *periodicity sequences* to reflect the ambiguous nature of the source of the aperiodicity in the reaction. We discuss the issue of chaos in the BZ reaction at length below.

Hudson, Hart, and Marinko [62] investigated the high flow rate aperiodicity in a detailed study which reported more complex periodic orbits. This highly influential study showed mixed-mode oscillations of 1^n type for $n = 0, \ldots, 4$.

For the first time, experimental time series showed MMOs of *mixed-parent type* – concatenations of neighboring periodic orbits. They observed time series for $1^1 1^2$ and 2^2 MMOs. Between periodic regimes, the authors report aperiodic trajectories which are concatenated from segments of nearby periodic orbits. In addition, they showed a periodic nearly homoclinic orbit, similar to the time series shown in [40]. Like [103], they also observed that the system transitions to steady state via a supercritical Hopf bifurcation.

To further investigate the nature of the observed aperiodic regimes, Vidal and coworkers [119] computed the Fourier transform (FT) of periodic and aperiodic experimental time series. The FT of all periodic time series showed strong peaks, indicating dominant frequencies, and a high signal-to-noise ratio. Harmonics of the largest peaks are found in the FT of the periodic time series. The FT of the aperiodic time series showed broadband spectra and no dominant frequencies. The authors argued that this is evidence of chaos in the aperiodic regimes. Using slightly different but comparable feed concentrations, Hudson and Mankin [63] verified the FT signal-to-noise findings for periodic and aperiodic time series. They also concluded that this is evidence of chaotic behavior at high flow rates.

Since the discovery of complex BZ dynamics, there has been controversy surrounding the nature of the aperiodicity observed at high flow rates. This is primarily due to the fact that the flow rate intervals for aperiodic regimes are very thin for such short residence times. As a result, distinguishing deterministic chaos from stochastic mixtures of periodic states due to imperfect mixing or flow rate fluctuations may be difficult. For example, the FT method suffers from this drawback. Others have argued [64] that aperiodicity may be the result

of perturbations in the mixing or flow rate that become amplified by the autocatalytic nature of the reaction. Schneider and Münster [104] investigated the source of high flow rate complexity by adding Gaussian noise of 5–7% to the flow rate and comparing the resulting dynamics to previous studies. They observed the statistical mixing of periodic states and argued that their results are consistent with the above findings, which are used as evidence of chaos at high flow rates. Györgyi and coworkers [56] addressed these concerns by performing precise experiments that varied the stirring rate, the impurity level in the catalyst, the type of pumping mechanism, and the reactor size and geometry. They independently reproduced the results of Hudson, Hart, and Marinko [62] and found that none of these changes resulted in qualitatively different sequences of periodicity and aperiodicity. All of the flow rates at which transitions in the perturbed experiments occurred differed from the original experiment by less than 1.3%. They concluded that the aperiodicity observed at high flow rates is due to the chaotic nature of the reaction.

3.2.3 Low flow rate complexity

In contrast to high flow rate complexity, aperiodicity observed at low flow rates is universally accepted as deterministic chaos. The experiments of Roux, Swinney and coworkers [114, 107, 99, 100] at the University of Texas utilized tools from dynamical systems to examine the nature of the oscillations at low flow rates. These tools included the use of phase plane reconstruction, Poincaré sections, return maps, next maximum amplitude (NMA) maps, and the computation of Lyapunov exponents. Turner and coworkers denote the 1^n periodic regimes by P_{n+1} and they denote the aperiodic regime that concatenates P_i and

P_{i+1} segments by C_i. In this work, we will commonly refer to the P_1 relaxation oscillation regime and the C_1 aperiodic regime which concatenations 1^0 and 1^1 trajectory segments. Turner et. al. [114] decrease the flow rate from the P_1 relaxation oscillation regime to the thermodynamic steady state for residence times between 0.87 hours and 2.28 hours. They observed a nearly symmetric pattern of periodic and aperiodic states as those found at high flow rates – periodic regimes P_2 through P_5 were observed, with aperiodic regimes found between each periodic regime.

The Texas group introduced the technique of phase space reconstruction to the chemical community in order to analyze the dynamics of the system. Following the construction of Takens [112], the phase portrait is reconstructed by choosing a time delay T_1 and plotting the time series $B(t_i)$ vs. $B(t_i + T_1)$, where $B(t_i)$ represents the time series of the platinum or bromide ion electrode. This process can be generalized to delay coordinate embeddings in higher dimensions. While the choice for the value of T_1 is nearly arbitrary (i.e. not a multiple of the period of a periodic orbit), Fraser and Swinney [36] found that an optimal choice for T_1 is generally between one-tenth and one-half of the period of a typical oscillation for noisy data. The Texas group typically used $T_1 = 8.8$ s. Using the reconstruction method, one visually verifies that the topological nature of periodic orbits and aperiodic orbits are different.

Turner et. al. [114] and Roux, Simoyi, and Swinney [99] reconstructed strange attractors observed at several parameter values. They computed intersections of an aperiodic trajectory in the C_1 attractor with a cross section, and found that the intersections lie on an approximately one-dimensional curve. Successive iterations $\{X_n\}$ form a sequence which can be used to define a one-

dimensional map $X_{n+1} = f(X_n)$. Roux et. al. [100] showed that the experimental return map has a single maximum, and approximated the unimodal map with an exponential function of the form $f(x) = axe^{-bx}$. They showed that the unimodal map has a positive Lyapunov exponent of $\lambda = 0.5 \pm 0.1 > 0$, indicating that the map exhibits deterministic chaos.

Hourai, Kotake, and Kuwata [61] also studied low flow rate complexity in detail. Using mixed-feed concentrations approximately an order of magnitude less than the Texas experiments (see Table 3.1 for the parameter values used in [61]), they produced a detailed sequence of periodic and aperiodic trajectories. As the flow rate increased, they observed trajectories that evolve from steady state to small amplitude periodic orbits, to 1^n MMOs, and finally to relaxation oscillations. Most impressively, they showed a 1^9 MMO whose SAOs show an hourglass pattern: between each large spike, the amplitude of the SAOs symmetrically decrease then increase. This behavior is consistent with oscillations observed near a dynamic Hopf bifurcation. Hourai and coworkers also fitted the experimental data with one-dimensional maps using piecewise smooth functions. For two of these maps, positive Lyapunov exponents are computed, indicating the existence of chaos in the approximating one-dimesional maps.

The carefully designed Texas experiments [114, 107, 99, 100] allowed for a more comprehensive comparison of experimental work to the existing mathematical theory of one-dimensional maps. Simoyi, Wolf, and Swinney [107] constructed experimental return maps and orbits of the maps that correspond to experimental time series. They compared the observed sequence of orbits to the universal sequence or "U-sequence" [78] of periodic orbits. Although the complete U-sequence was not observed, the ordering of the observed states

were consistent with the U-sequence. Finite segments of trajectories which correspond to missing orbits in the U-sequence were also observed, however, these states were not determined to be asymptotically stable. This incompleteness is likely due to the narrow flow rate ranges over which the missing states exist.

Simoyi, Wolf, and Swinney [107] and Coffman et. al. [21] documented the first instance of a PD sequence using experimentally constructed one-dimensional maps. A relaxation oscillation in the P_1 regime was observed with period T. As the flow rate was decreased, orbits of period $2T$, $4T$, and $8T$ were observed after a sequence of PD bifurcations. Only a few segments of the period-16 orbit were observed because the flow rate regime where this orbit is stable is very thin. Although finding an entire PD sequence is not experimentally feasible, these studies indicate that a PD sequence to chaos is likely to occur in the BZ reaction. In addition to the PD sequence, Coffman et. al. also observed multiplicity in the system. The experimental setup was nearly identical to previous studies [114, 100], but after purifying the commercially available malonic acid, they found three separate flow rate intervals where the U-sequence is observed. This suggests that the BZ reaction is highly sensitive to impurities.

Most experiments investigated either low flow or high flow complexity, but not both. In contrast, Ibison and Scott [64] used one set of flow concentrations which were nearly identical to [63], and varied the residence times between the two stable stationary states on the flow and thermodynamic branches. In contrast to the very regular alternation of periodicity and aperiodicity observed in [61] at low flow rates, Ibison and Scott found mostly aperiodic states. At high flow rates, they found small sinusoidal orbits emanating from a supercritical Hopf bifurcation as the flow rate was decreased from the flow branch steady

state. Immediately after this state they found the previously unreported behavior of 1^n time series for very large n ($n \approx 40$), where the amplitude of the small orbits remain visible. The interspike time in this regime is very long, approximately 10 residence times. The SAOs of these orbits sometimes showed a pattern of increasing and decreasing amplitudes between spikes. The authors suggested that this behavior may be the result of interaction with a torus.

3.2.4 Routes-to-chaos

The one-dimensional maps constructed from experimental data provide evidence for a period doubling route-to-chaos in the BZ reaction. Although inherent experimental limitations prevent the direct observation of chaos, dynamical systems theory provides the tools to interpret the PD sequence and other structures that are associated with routes-to-chaos. This includes the breakup of an invariant torus, intermittency, and crisis bifurcations. The existence of these phenomena provide some of the best evidence for chaos at high flow rates.

Researchers at Bordeaux [1] performed an impressive set of experiments documenting the existence of tori and their break-up en route to chaos. Argoul and coworkers performed five careful experiments where they tracked the evolution of a torus and periodicity sequences. At very low flow rates the thermodynamic steady state was observed. As the flow rate increased, they reported a supercritical Hopf bifurcation that created small amplitude periodic orbits. They carefully verified that both the amplitude and period of the limit cycles scale according to mathematical theory of Hopf bifurcations [47]. At higher flow rates, a secondary Hopf bifurcation is observed and creates an invariant

torus. As the flow rate was increased further, the system spent more time near equilibrium (in the "hole" of the torus) and the time between large oscillations grew. Using slightly different initial conditions, they showed that the torus deforms and exhibits a fractal nature. The intersections of the torus and a Poincaré section became thick, indicating chaotic behavior that resulted from the folding and stretching of the torus.

Masełko and Swinney [77] also observed quasiperiodicity, phase-locking on a torus, and sequences of periodicity. With fine experimental control, they were able to resolve MMOs that have both two- and three-parent types. They showed that the sequence of mixed-parent states can be described with Farey arithmetic [28]. While bistability at a subcritical Hopf bifurcation was identified early in experimental work [22], Masełko and Swinney reported the first instance of bistability of MMOs. Starting with a 1^1 MMO, the stirring mechanism was turned off for ten minutes. Upon reactivation of the stirring mechanism, a 2^2 MMO emerged.

Richetti and coworkers [92] first observed a phenomenon called a crisis, where a chaotic attractor of a 1D map collides with an unstable periodic orbit. This internal crisis is associated with a sudden expansion of the chaotic attractor. They observed an aperiodic attractor of 0^1 orbits in the vicinity of the chaotic attractor C_3, which concatenates 1^2 and 1^3 orbits. As the flow rate was varied, the chaotic attractors collided and expanded, resulting in trajectories that have long sequences of 0^1 segments and mixtures of 1^2 and 1^3 segments. They numerically identified a similar crisis using a 7-dimensional model of the BZ equations proposed by Richetti and Arneodo [91]. Although the BrO_3^- feed concentration used in the simulation was similar to the experimental value, the

concentrations for the MA and Ce(III) feeds differed by two and one orders of magnitude, respectively.

Crisis bifurcations are related to the phenomenon of intermittency. Type-I intermittency occurs in a 1D map near a saddle-node bifurcation as an orbit takes many iterates to pass through the thin bottleneck near the bifurcation [89]. Pomeau et. al. [90] observed type-I intermittency in the BZ reaction at low flow rates. From the thermodynamic branch, a supercritical Hopf bifurcation was observed. As the flow rate was increased they observed small oscillation behavior interrupted by large spikes. An experimentally computed one-dimensional map appears similar to a map near a saddle-node bifurcation. Baier, Wegmann, and Hudson [5] also found intermittency when they observed time series with long intervals of both 4^1 and small amplitude 0^1 segments at low flow rates. They identified this type of intermittency as type-III, which occurs when a limit cycle loses stability as a Floquet multiplier passes to the outside of the unit circle through -1.

A few comments on the existence of chaos in the BZ reaction are necessary. The aperiodicity observed at low flow rates has been universally accepted as deterministic chaos. The width of the C_1 chaotic band is larger than the flow rate resolutions of the the pumping mechanisms. The evidence mounted via the use of dynamical systems theory – Poincaré maps, return maps, next-maximum amplitude maps – have led to the consensus that deterministic chaos occurs in the BZ reaction at low flow rates. Unfortunately, the experimental control necessary to discern chaotic bands at high flow rates prevents the confirmation of chaos at these flow rates. The discussion in this chapter examines evidence both for and against chaos at high flow rates. Fortunately, the identification of

dynamical objects associated with well known routes-to-chaos provide the best evidence for chaos at high flow rates. However, even today there is no universal consensus on this issue.

Experiment	[MA]	$[BrO_3^-]$	$10^3 \cdot$ [cat]	$[H_2SO_4]$	Temp (°C)	Observed Phenomena
[110, 111]	0.5	0.09	0.8 (C,M)	1.5	25	DC-MMOs
[75]	0.032	0.5	1.0	1.5	25	ROs
	0.032	0.01	1.0	1.5	40	ROs
	0.032	0.01	0.2	1.5	40	MMOs
	0.066	0.025	0.2	1.5	40	DC-MMOs
[40, 62, 63, 56]	0.3	0.14	1.0	0.2	25	HF-PAS, HC
[40, 103]	0.3	0.14	0.125 (F)	0.2	25	HF-PAS, HC
[119]	0.24	0.108	0.75	1.44	39	PAS
[98]	0.08	0.036	0.25	1.44	40	Strange attractor
[114, 107, 100, 99]	0.25	0.14	0.83	0.2	28.3	LF-PAS
[61]	0.056	0.039	0.025	0.05	25	Detailed (LF)PAS
[76]	0.0813	0.0275	0.416 (M)	1.5	25	MMOs
[77]	0.018	0.0275	0.416 (M)	1.5	28	MMOs
	0.3	0.0275	0.416 (M)	1.5	28	DC-MMOs
	0.056	0.033	0.416 (M)	1.5	28	MP-MMOs
	0.049	0.033	0.416 (M)	1.5	28	1^1-2^2 MMOs
	0.081	0.028	0.416 (M)	1.5	28	3^3 MMO
	0.3	0.028	0.416 (M)	1.5	28	6^6 MMO
[92]	0.25	0.1	1.7	0.2	27	LF-PAS, crisis
[21, 104]	0.25	0.1	0.83	0.2	28	LF-PAS, mult.
[1]	0.2	$6.5 \cdot 10^{-3}$	0.5	1.5	43	HB
	0.525	0.036	0.25	0.75	43	QP
	0.5	0.036	0.25	0.75	40	Fractal torus
	0.15	0.075	0.5	1.0	43	HF-PAS
	0.1	0.01	0.5	1.5	43	HF-PAS
[5]	0.3	0.1	0.25	0.4	25	HF-PAS, Type-III inter.
[64]	0.3	0.14	1.0	0.23	21	(LF,HF)-PAS, QP
[104]	0.3	0.087	1.0	0.37	25	HF-PAS

Table 3.1: Experimental parameters and observed phenomenon for many BZ experiments. Table 4.2 lists the conversion of $[H_2SO_4]$ to $[H^+]$ concentration. The catalyst is assumed to be Cerium (C), unless otherwise noted: F and M indicate ferroin and manganese. Key: PAS – periodic-aperiodic sequences (HF – high flow, LF – low flow), HC – homoclinicity, MMO – mixed-mode oscillations (MP – mixed-parent type, DC – double composite), QP - quasiperiodicity, HB – Hopf bifurcation, mult. – mulitiplicity, and inter. – intermittency.

3.3 Modeling results

The complexity of the chemistry and variety of behaviors exhibited by the BZ reaction make it difficult to model. Attempts to model the BZ reaction have typically fallen into one of several categories: 1) stoichiometric mass-action models of the homogeneous BZ-CSTR reaction, 2) simple models intended to isolate and replicate specific behaviors exhibited by the reaction, and 3) the construction of families of one-dimensional maps which approximate the dynamics observed in the reaction. Each of these avenues has contributed greatly to the chemical and mathematical understanding of BZ dynamics. Below, we outline some of the most important modeling results in each of these categories.

3.3.1 FKN Mechanism

The BZ reaction consists of both organic and inorganic chemical reactions. The inorganic reactions that oxidize the catalyst are well understood. However, the organic reactions that reduce the catalyst are quite complicated; Gyögyi, Turányi, and Field [57] expanded the organic process into 80 reactions involving 26 intermediate species. In order to formulate a model of reasonable size convenient for analysis, it is necessary to distill the most basic features of the inorganic chemistry. The first chemical mechanism used to describe the BZ reaction in a batch (closed) reaction was proposed by Field, Körös, and Noyes [34], and is commonly referred to as the FKN mechanism. The FKN mechanism is a series of 10 chemical reactions that can be grouped into three processes, called Process A, B, and C. The reactions are listed in Table 3.2. The different processes are responsible for the transitions seen in a single cycle of a batch reaction. The

success of the FKN mechanism in describing BZ dynamics makes it the starting point for nearly all BZ modeling. As a result, we introduce the FKN mechanism in some detail below.

(R1)	$Br^- + HOBr + H^+$	$\leftrightharpoons$	$Br_2 + H_2O$
(R2)	$HBrO_2 + Br^- + H^+$	$\leftrightharpoons$	$2HOBr$
(R3)	$BrO_3^- + Br^- + 2H^+$	$\leftrightharpoons$	$HBrO_2 + HOBr$
(R4)	$2HBrO_2$	$\leftrightharpoons$	$BrO_3^- + HOBr + H^+$
(R5)	$BrO_3^- + HBrO_2 + H^+$	$\leftrightharpoons$	$2BrO_2 + H_2O$
(R6)	$BrO_2 + Ce(III) + H^+$	$\leftrightharpoons$	$HBrO_2 + Ce(IV)$
(R7)	$BrO_2 + Ce(IV) + H_2O$	$\leftrightharpoons$	$Ce(III) + BrO_3^- + 2H^+$
(R8)	$Br_2 + CH_2(CO_2H)_2$	$\rightarrow$	$BrCH_2(CO_2H)_2 + Br^- + H^+$
(R9)	$6Ce(IV) + CH_2(CO_2H)_2 + 2H_2O$	$\rightarrow$	$6Ce(III) + HCO_2H + 2CO_2 + 6H^+$
(R10)	$4Ce(IV) + BrCH_2(CO_2H)_2 + 2H_2O$	$\rightarrow$	$4Ce(III) + HCO_2H + 2CO_2 + Br^- + 5H^+$

Table 3.2: The FKN mechanism for the BZ reaction.

Process A: Reactions R1–R3. Process A dominates when the concentration of the bromide ion Br^- is high. All reactions in Process A remove the bromide ion, and the process reduces the bromate (BrO_3^-) to bromine (Br_2). The following reaction is a weighted sum of the reactions in Process A and can be considered the overall stoichiometry of Process A,

$$\text{R3 + R2 + 3R1: } BrO_3^- + 5Br^- + 6H^+ \rightarrow 3Br_2 + 3H_2O.$$

Once Process A removes the bromide ion, reactions R1–R3 occur at very low rates, which allows Process B to become dominant.

Process B: Reaction R4–R6. Process B follows Process A and dominates when the concentration of the bromide ion Br^- is low. When bromide ion concentration is low, the interaction with Br^- in R3 is very slow, allowing the bromate reaction with $HBrO_2$ in R5 to dominate. In Process B, $HBrO_2$ is catalyzing its own production, i.e., the reaction is autocatalytic. R5 produces $2BrO_2$, which proceeds to oxidize the catalyst in R6, producing $2HBrO_2$. Once Process B be-

gins, $HBrO_2$ is produced at a rapid rate. The autocatalytic reaction is given by the following sum,

$$\text{R5} + 2\text{R6}: \ BrO_3^- + HBrO_2 + 2Ce(III) + 3H^+ \rightarrow 2HBrO_2 + 2Ce(IV) + 3H_2O.$$

Process B is limited by reaction R4 and the oxidation of the catalyst in R6. Process B is terminated when a large percentage of the catalyst is in its oxidized state.

Process C: Reactions R7–R10. Since Processes A and B remove the bromide ion and oxidize the catalyst, Process C must reduce the catalyst and produce the bromide ion. Process C encapsulates the organic chemistry of the BZ reaction and is the least understood of the three processes. The overall stoichiometry of the process is given by the following reaction,

$$2Ce(IV) + BrMA + MA \rightarrow f Br^- + 2Ce(III) + \text{other products}.$$

Process C includes a stoichiometric factor f, which is a constant whose values usually lie in the interval $[2/3, 2]$. The stoichiometric factor f reflects the fact that bromide ion Br^- can be produced by interacting with bromine Br_2 and through the oxidation of BrMA, and that these processes occur at different rates, so the exact rate of production is unknown. If the oxidized catalyst Ce(IV) only reacts with BrMA, $f = 2$. If $f > 2/3$, there is a net bromide ion production, which matches batch experimental observations. Further details on Process C are carefully presented in [31] and [57].

3.3.2 Oregonator

The number of reactions and species involved in the FKN mechanism make it difficult to work with numerically. To simulate BZ dynamics in a closed reactor, Field and Noyes [35] produced the first simplified model based on the FKN mechanism, commonly called the Oregonator. The reactions of the Oregonator are listed in Table 3.3: the species involved are denoted by A = BrO_3^-, B = all oxidized species, X = $HBrO_2$, Y = Br^-, Z = Ce(IV), and P = HOBr.

$$\begin{array}{lrcl} \text{(O1)} & \text{A} + \text{Y} & \rightarrow & \text{X} + \text{P} \\ \text{(O2)} & \text{X} + \text{Y} & \rightarrow & 2\text{P} \\ \text{(O3)} & \text{B} + \text{X} & \rightarrow & 2\text{X} + 2\text{Z} \\ \text{(O4)} & 2\text{X} & \rightarrow & \text{A} + \text{P} \\ \text{(O5)} & \text{B} + \text{Z} & \rightarrow & \frac{1}{2} f \text{Y} \end{array}$$

Table 3.3: The reactions of the Oregonator.

Species A and B are assumed to be constant, and the bifurcation parameters are taken to be f and the reaction rate of reaction O5, denoted k_{O5}. In [34], Field, Körös, and Noyes proposed a set of reaction rates, which are referred to as FKN rates or the 'Hi' rates. Using the law of mass action, Table 3.3 results in a three-dimensional stiff differential equation. Taking $f = k_{O5} = 1$, Field and Noyes showed that the Oregonator exhibits limit cycles whose shape and period agree with experiments. However, when experimentally relevant values of f and k_{O5} are used the period of oscillations does not agree well with experiments.

Field and Noyes [35] used a quasi-steady state assumption on the bromous acid $HBrO_2$ in order to reduce the dimension of the system from three to two. This allows the system to be analyzed using the method of nullclines. Tyson [117] analyzed the two-dimensional Oregonator extensively, and argued that the original FKN rate constants are incorrect. He suggested that a new set of rate

constants are necessary to properly describe BZ dynamics. Field and Försterling [33] completed an independent measurement of the rate constants that are now universally accepted as more chemically accurate. These are commonly referred to as the FF constants, or the 'Lo' set. Tyson [116] also compared several simplifications of the full FKN mechanism, including the "IUator" of Schmidt and Ortoleva [102], and "Model K" of Tomita et. al. [113].

The first modification to the Oregonator was made by Field [30], who allowed all Oregonator reactions in Table 3.3 to be reversible. The resulting differential equation is also three-dimensional and the reversibility allows for oscillations to occur over chemically relevant intervals for the parameters f and k_{O5}. Field also found that the system exhibits excitability, which is observed experimentally in a closed reactor as oscillations approach thermodynamic equilibrium. It should be noted that although both the reversible and irreversible Oregonator models are three-dimensional, chaos was not found in either model.

To model the reaction in a CSTR, Turner et. al. [114] added flow terms to the reversible Oregonator using the FKN rate constants at low flow rates. They reported the alternation of periodic and chaotic sequences, however, no time series from the model were shown. While the sequences of periodicity and chaos were qualitatively similar to those observed experimentally, there were several key differences. The first difference is that the chaotic intervals were found to be much much wider than the periodic intervals. Second, the residence times over which complexity was observed did not match experiments. Turner et. al. observed experimental sequences of periodicity and aperiodicity for residence times $0.8\text{ hr} < \tau < 2.5\text{ hr}$. Using the same parameter values in the model, they found the corresponding behavior for residence times $0.294\text{ hr} < \tau < 0.302\text{ hr}$.

Janz, Vanecek, and Field [66] concentrated their efforts on modeling the double composite MMOs observed in [110, 111, 75]. They added flow terms to the irreversible Oregonator and made the species A and P dynamic variables, resulting in a five-dimensional model. The key aspect of this work is the parametrization of the stoichiometric factor f by the variable P. Setting $f = FP^2/(K + P^2)$ where F is approximately the average of f and $K = 4$, the bifurcation parameter f has a sigmoidal dependence on P. As the concentration of P oscillates, the parameter f also oscillates, allowing the system to repeatedly cross a subcritical Hopf bifurcation point. As a result, the system oscillates between regimes of steady state behavior and large periodic orbits, creating alternating trains of large and small amplitude oscillations like those observed experimentally.

Although various versions of the Oregonator were able to reproduce some experimental behavior qualitatively, it wasn't until Showalter, Noyes, and Bar-Eli [106] modified the reversible Oregonator that complex mixed-mode oscillations were able to be reproduced. This model is commonly referred to as the SNB model. They considered the inorganic steps O1–O4 to be reversible, while the organic reaction O5 was not. Additionally, the SNB model splits the autocatalytic step O3 into two separate reactions, similar to the original FKN mechanism. The six reactions of the SNB model involve seven different species, including the reduced and oxidized form of the catalyst Ce(III) and Ce(IV), and the radical species $BrO_2\cdot$. The total amount of the catalyst is conserved (Ce_{tot} = Ce(III) + Ce(IV)), and the BrO_2 radical is assumed constant. The resulting system of differential equations is five-dimensional.

The seminal study [106] shows that the SNB model is able to reproduce the character of the MMOs. For the first time, SAOs with an hourglass shape were

replicated numerically. High degrees of complexity were found in the model, including MMOs of mixed-parent type. However, both Showalter et. al. and Ganapathisubramanian and Noyes [37] observed no chaos. Although the SNB model is more satisfying chemically, the older FKN rate constants are used because the MMOs are not reproduced when the more accurate FF rate constants are used.

Barkley et. al. [8] gave the first evidence of quasiperiodicity in the SNB model. Using the original FKN rate constants, and varying both the Ce(III) and Br^- mixed-feed concentrations, tori are shown to form after a secondary Hopf bifurcation. While chaos is not explicitly found in the model in this study, they found that tori become wrinkled, which is a precursor to torus breakup and chaos. Due to numerical convergence issues, they are unable to characterize the behavior of the system during the transition from toroidal dynamics to MMOs; chaos was neither produced nor was it ruled out. Furthermore, the concentration of HOBr in the SNB model is much higher than observed experimentally.

It should be noted that the inability to produce chaotic time series in the earliest Oregonator models produced skepticism about the nature of the experimentally observed aperiodicity. Such skepticism was voiced more strongly when the SNB model was able to reproduce the complicated MMO sequences to great detail, but was unable to produce chaotic time series. The idea that the experimental aperiodicity was due to stochastic effects began to gain traction. This led to the study of coupled BZ systems in order to model imperfect mixing of the solution, where chaotic time series proved easy to produce [74].

3.3.3 Normal forms

Richetti et. al. [93] studied quasi-periodicity and MMOs in the BZ reactions using a perturbation of the three-dimensional hysteresis Hopf normal form (HHNF). For certain parameter values, the HHNF undergoes a secondary Hopf bifurcation to form a torus. Under a non-axisymmetric perturbation, MMOs form on the torus, which can become wrinkled. For other parameter values, sequences of periodicity and aperiodicity are observed. In the same study, Richetti et. al. [93] also simulated time series with a seven-dimensional variant of the FKN scheme developed by Richetti and Arneodo [91]. This model is quite rich – it nearly identically replicates the Texas periodicity sequences and also produces complex MMOs of multiple parent type, similar to those seen in Masełko and Swinney [77]. Richetti et. al. [92] showed that this system also replicates experimentally observed intermittency.

It was first suggested by Schmidt et. al. [103] that a folded slow manifold may be necessary for the creation of MMOs. Barkley [7] explored this possibility and discussed several slow manifold models, including the HHNF and a model proposed by Rössler [96]. Barkley compared the geometric properties of experimental time series with those of the Rössler model for MMOs (whose parameters are taken from Gaspard and Nicolis [38]) on a folded surface. Unsatisfied with both the HHNF and the Rössler model, Barkley proposed a phenomenological model which couples a pair of two-dimensional systems: system I exhibits a Hopf bifurcation and system II exhibits excitability. The model uses the periodic orbits of system I to perturb and excite system II. In this way, it is able to produce steady state, small amplitude periodic orbits, double composite and mixed-parent type MMOs, and chaos. However, Barkley was unable to find

invariant tori in this model.

3.3.4 Mappings

Many experiments have shown that sequences of experimental behavior can be described well by one-dimensional maps. Most studies using one-dimensional maps either construct a Poincaré map or a next maximum amplitude map and fit the experimental data with piecewise smooth functions. An alternate approach is to define a family of one-dimensional maps that have a qualitatively similar shape and exhibit a similar sequence of bifurcations. Two such examples are indented trapezoid maps of Beyer, Mauldin, and Stein [14] and Z-maps of Ringland, Issa, and Schell [94].

The indented trapezoid map was first suggested to Beyer, Mauldin, and Stein by T. Y. Li as a family of maps that would exhibit multiple steady states. The indented trapezoid maps are a five-parameter family of piecewise linear maps, whose height is taken as the main bifurcation parameter (see Figure 10 in [21] for an explanation of the map parameters). Coffman et. al. [21] fit the indented trapezoid maps to experimentally observed return map data. It was observed that bistability occurs in the system with purified malonic acid, and that these transitions can be described by the family of indented trapezoid maps.

The Z-maps of Ringland, Issa, and Schell [94] are also a five-parameter family of smooth maps with a single maximum and minimum. The main bifurcation parameter s controls the smoothness of the map: at low s the maps resemble a slowly varying cubic map, and at large s, the maps resemble a piecewise linear map with a nearly vertical middle branch. These maps exhibit both the

U-sequence and Farey sequences. This family has successfully reproduced sequences of bifurcations in other chemical models, such as the autocatalator [79].

3.3.5 More flow models

Bar-Eli and Noyes [6] implemented a full FKN scheme to replicate the results of Masełko and Swinney [77]. The FKN scheme implemented is a variant of a model proposed by De Kepper and Bar-Eli [22], called M2, where H_2O is allowed to be a dynamic variable. M2 is reduced to a 5-dimensional equation through a series of conservation and individual species assumptions. The feed parameters MA and BrO_3^- are used to produce two-dimensional bifurcation diagrams. Complex MMOs are found, including trajectories of two- and three-parent type. Chaotic mixing of states is found for narrow intervals of the flow rate and Farey sequences consistent with [77] are observed.

Ibison and Scott [65] proposed a five-dimensional model that implemented an inorganic production of Br^- that differed from the FKN mechanism. The model is an expanded form of an amplified Oregonator model proposed by Ruoff and Noyes [101]. The organic chemistry (reaction O5) has been expanded to four reactions which include the species Ce(III), Ce(IV), and $BrO_2\cdot$. The resulting model has Br^-, $HBrO_2$, HOBr, Ce(III), and $BrO_2\cdot$ as its variable species. The system replicates many experimental behaviors, including composite double MMOs, mixed-parent type MMOs, and periodicity sequences. The periodicity sequences at low flow rates were observed to be in agreement with the experiments of Hourai et. al. [61]. However, the Br^- concentrations observed in the model are roughly 5 or 6 orders of magnitude too small. Interestingly,

the MMOs were reported to have two different SAO patterns: an hourglass pattern and a wedge pattern, where SAOs have increasing amplitude. Mathematically, this suggests that the model may generated SAOs by more than one MMO mechanism.

3.4 Conclusion

The BZ reaction in a CSTR displays a stunning variety of behaviors. A good model will replicate many of these experimentally observed behaviors at experimentally relevant parameters. Deriving such a model requires an understanding of the organic chemistry involved in the reactions. The organic chemistry is quite complex and involves many intermediate species and reactions, many of whose reactions rates are unknown. The joint goals of capturing the chemical mechanisms generating the oscillations and making a chemically relevant low dimensional model appear to be mutually exclusive. However, experimental studies show that one-dimensional maps can be used to model much of the behavior in the BZ reaction. This is strong evidence that the underlying attractor of the reaction may be low dimensional. This gives the modeler some hope: if the complete chemistry is known (or simply complete enough), it may only be necessary to choose the correct chemical approximations in order to derive a chemically relevant low dimensional model.

This is approach taken by Györgyi, Field, and coworkers [57, 55, 53]. After distilling the organic process to its essential mechanism, Györgyi and Field propose a family of models to describe the BZ reaction. We begin the next chapter with an outline of this family of models.

CHAPTER 4

GYÖRGYI AND FIELD MODEL OF THE BELOUSOV-ZHABOTINSKII REACTION

4.1 Introduction

In this chapter, we examine a family of models for the CSTR-BZ reaction proposed by Györgyi and Field [53]. Specifically, we focus on two variants of a four-dimensional model called Model D. This family is derived from an expanded FKN mechanism [34] and, more importantly, reproduces experimental time series using experimental parameters. The goal of this chapter is twofold: 1) to use geometric singular perturbation theory (GSPT) to frame our analysis of the mathematical mechanisms that create complexity, including mixed-mode oscillations, at both low and high flow rates, and 2) to carefully compare behaviors exhibited by the model to experimentally observed behaviors using experimental parameters as model parameters.

In the analysis of the models, we use GSPT to frame our analysis. The chemical reaction model has a natural separation of time scales which allows us to construct approximate fast and slow subsystems. We emphasize that our use of GSPT is non-rigorous; we do not use global rescalings in order to place the system into a slow-fast normal form. Instead, we use GSPT as a tool to interpret the behavior exhibited by the models. Our primary use of slow-fast theory is the computation of equilibria of approximating fast subsystems for Model D. This allows us to see if the dynamics of the fast subsystem are consistent with the dynamics of the full system.

Two of the biggest difficulties we encounter in our analysis are the lack of a global separation of time scales and the identification of slow variables. In Model D, the ratio of the time scales governing the different chemical species may change radically throughout phase space, including different regions of phase space visited by the same trajectory. This prevents us from identifying a globally consistent set of slow variables. This lack of global separation is problematic for the application of GSPT methods. Although the theory is not always directly applicable, we will sometimes use the language of GSPT to describe the behaviors observed in the models. Issues related to varying time scales are discussed more fully in later sections.

Figure 4.1 shows two examples of the oscillatory behavior of Model D at a low and high flow rate. Note that SAOs in Figure 4.1(a) have an hourglass shape. For each flow rate regime, we use the natural separation of time scales to construct approximate fast and slow subsystems. For the parameter values used in [53], we show that the fast subsystems have a Hopf bifurcation, also called a dynamic Hopf bifurcation. Dynamic Hopf bifurcation has been identified as an SAO generating mechanism in both the Olsen model of the Perioxidase-Oxidase reaction [24] and the SNB model of the BZ reaction [25]. This suggests that dynamic Hopf bifurcation is an important mechanism in the generation of chemical oscillations.

The rest of this chapter is organized in the following manner. In section 2, we introduce the Györgyi and Field family of models, describe the dimension reduction methods used to define the four-dimensional Model D, and discuss how to scale Model D for analysis. Sections 3 and 4 give a mathematical description of the behaviors at high and low flow rates, respectively. In section 5, we

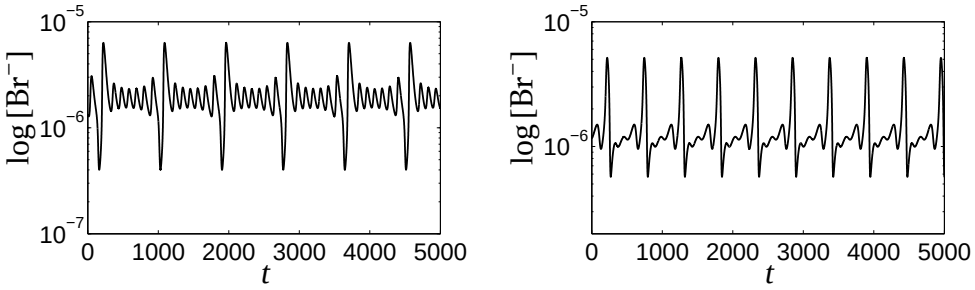

(a) $k_f = 1.8 \cdot 10^{-4}$. (b) $k_f = 1.31 \cdot 10^{-3}$.

Figure 4.1: Time series for MMOs in Model D: (a) A 1^6 mixed-mode oscillations at flow rate $k_f = 1.8 \cdot 10^{-4}$, (b) a 1^3 MMO at flow rate $k_f = 1.31 \cdot 10^{-3}$. Low and high flow rate parameters are used in Model D_{QSS} and Model D_{EQ}, respectively.

catalog the behavior of Model D by choosing experimental parameters as model parameters. Finally, in section 6, we outline future directions for this work.

4.2 Model D

Györgyi, Rempe, and Field [55] first proposed a model which is both chemically realistic and amenable to reduction. Understanding that a major shortcoming of previous models was the lack of a sophisticated organic mechanism, Györgyi, Turányi, and Field [57] expanded the organic chemical mechanism to 80 reactions and 26 chemical species. In [55], this mechanism is distilled into nine reactions involving only the organic species malonic acid, bromomalonic acid (BrMA), and malonyl radical (MA·). The proposed model, later called Model A, is comprised of 19 chemical reactions and 11 chemical species. The differential equation describing Model A can be found by applying the Law of Mass Action to the 19 reactions and adding terms to model the inflow and outflow of a CSTR.

Györgyi and Field formulate the family of models through a series of numer-

ical and chemical (stoichiometric) approximations. We refer to the collection of these models as the GF family of models. Györgyi and Field found "redundant species" by removing all reactions involving each individual species, and comparing the resulting trajectories with the full system. If the resulting trajectories retain their original character, the species is declared redundant. Through this process, the species Br· is removed. The MA concentration is also noted to be nearly constant for all chemically relevant parameters, so it is assumed constant. These assumptions result in Model B, which is a 9-dimensional system described by 13 reactions.

Model C, a seven-dimensional system, is derived by eliminating two of the Model B species: hydrobromous acid (HOBr) and bromine (Br_2). Bromine is produced and consumed by exactly one reaction each in Model B. Reaction B1 is controlled by diffusion and reaction B9 is considered fast in the presence of high [MA]. The reactions are given by the following

$$\begin{aligned} &\text{(B1)} \quad \mathrm{HOBr} + \mathrm{Br^-} + \mathrm{H^+} \rightarrow \mathrm{Br_2} + \mathrm{H_2O}, \\ &\text{(B9)} \quad \{\mathrm{MA}\} + \mathrm{Br_2} \rightarrow \mathrm{BrMA} + \mathrm{Br^-} + \mathrm{H^+}. \end{aligned}$$

Because reaction B9 is considered fast, all HOBr consumed in reaction B1 is converted into BrMA, eliminating the intermediate species Br_2. Györgyi and Field also eliminate HOBr by replacing it with BrMA in the model. Therefore, Model C has different chemistry than Model B, and is the smallest model in the family that can be derived using the Law of Mass Action.

Additional assumptions on individual species are necessary to further reduce the dimension of the model. Model D is a four-dimensional reduction of Model C originally formulated in terms of the concentration of the species $HBrO_2$, Br^-, Ce(IV), and BrMA. Györgyi and Field used the conservation of the

total amount of Cerium to remove Ce(III) from the model. We reformulate the model in terms of Ce(III) because Ce(III) is used as an experimental parameter. The concentration of the malonyl radical MA· is replaced by a polynomial expression representing the quasi-steady state assumption (QSS), which assumes that $d[\mathrm{MA}\cdot]/dt \approx 0$ while disregarding the flow term. At a chaotic low flow rate $k_f = 3.17 \cdot 10^{-4}$, good agreement between the QSS assumption and the Model C concentration of MA· is found. Finally, the radical species $BrO_2\cdot$ is eliminated by both an equilibrium (EQ) and a QSS assumption. This is motivated by the findings of Field and Försterling [33] that $[BrO_2\cdot]$ is usually at equilibrium with $[HBrO_2]$ and $[BrO_3^-]$. The assumption is given by the relation

$$[BrO_2\cdot]_{EQ} = \sqrt{k_{C4}[HBrO_2]}/k_{C5}. \tag{4.1}$$

However, the EQ assumptions overestimates $[HBrO_2]$ at low concentrations. Therefore, the QSS assumption is used as an alternative

$$[BrO_2\cdot]_{QSS} = \frac{-k_{C6}[\mathrm{Ce(III)}] + \sqrt{(k_{C6}[\mathrm{Ce(III)}])^2 + 8k_{C5}[HBrO_2](2k_{C4} + k_{C7}[\mathrm{Ce(IV)}])}}{4k_{C5}}. \tag{4.2}$$

The equilibrium and quasi-steady state assumptions for $[BrO_2\cdot]$ yield two versions of Model D: D_{EQ} and D_{QSS}. The reactions and reaction rates for the two models are equal, and can be found in Table 4.1. Note that $[BrO_2\cdot]_{EST}$ in reaction D4 is given by either $[BrO_2\cdot]_{EQ}$ or $[BrO_2\cdot]_{QSS}$. Model D is given by the equations

	Reaction	Reaction rate	Rate constant
D1.	$Br^- + HBrO_2 + \{H^+\} \rightarrow 2BrMA$	$r_{D1} = k_{D1}[Br^-][HBrO_2][H^+]$	$k_{D1} = 2.0 \cdot 10^6/(M^2 s)$
D2.	$Br^- + \{BrO_3^-\} + 2\{H^+\} \rightarrow BrMA + HBrO_2$	$r_{C2} = k_{C2}[Br^-][BrO_3^-][H^+]^2$	$k_{C2} = 2.0/(M^3 s)$
D3.	$2HBrO_2 \rightarrow BrMA$	$r_{D3} = k_{D3}[HBrO_2]^2$	$k_{D3} = 3.0 \cdot 10^3/(Ms)$
D4.	$\frac{1}{2}HBrO_2 + Ce(III) + \{H^+\} \rightarrow HBrO_2$	$r_{D4} = k_{D4}[Ce(III)][H^+][BrO_2\cdot]_{EST}$	$k_{D4} = 6.2 \cdot 10^4/(M^2 s)$
D5.	$HBrO_2 \rightarrow Ce(III) + \frac{1}{2}HBrO_2$	$r_{D5} = k_{D5}[Ce(IV)][HBrO_2]$	$k_{D5} = 7.0 \cdot 10^3/(Ms)$
D6.	$\{MA\} \rightarrow Ce(III)$	$r_{D6} = k_{D6}[MA][Ce(IV)]$	$k_{D6} = 0.3/(Ms)$
D7.	$BrMA \rightarrow Ce(III) + Br^-$	$r_{D7} = k_{D7}[BrMA][Ce(IV)]$	$k_{D7} = 30.0/(Ms)$
D8.	$BrMA \rightarrow Br^-$	$r_{D8} = k_{D8}[BrMA][MA\cdot]_{QSS}$	$k_{D8} = 2.4 \cdot 10^4/(Ms)$

Table 4.1: Model D reactions, reaction rates, and rate constants. The model is derived in terms of Ce(III) instead of Ce(IV). Curly braces $\{\cdot\}$ indicate species whose concentrations are assumed to be constant.

$$\begin{aligned}
d[HBrO_2]/dt = &- k_{D1}[Br^-][HBrO_2][H^+] + k_{D2}[Br^-][BrO_3^-][H^+]^2 - 2k_{D3}[HBrO_2]^2 \\
&- 0.5k_{D4}[H^+][Ce(III)][BrO_2\cdot]_{EST} + 0.5k_{D5}[HBrO_2][Ce(IV)] \quad (4.3a) \\
&+ k_f([HBrO_2]_{mf} - [HBrO_2]), \\
d[Br^-]/dt = &- k_{D1}[Br^-][HBrO_2][H^+] - k_{D2}[Br^-][BrO_3^-][H^+]^2 \\
&+ k_{D7}[BrMA][Ce(IV)] + k_{D8}[MA\cdot]_{QSS}[BrMA] \quad (4.3b) \\
&+ k_f([Br^-]_{mf} - [Br^-]), \\
d[Ce(III)]/dt = &- k_{D4}[H^+][Ce(III)][BrO_2\cdot]_{EST} + k_{D5}[HBrO_2][Ce(IV)] \\
&+ k_{D6}[MA][Ce(IV)] + k_{D7}[BrMA][Ce(IV)], \quad (4.3c) \\
d[BrMA]/dt = &\ \alpha(2k_{D1}[Br^-][HBrO_2][H^+] + k_{D2}[Br^-][BrO_3^-][H^+]^2 + k_{D3}[HBrO_2]^2 \\
&- k_{D7}[BrMA][Ce(IV)] - k_{D8}[MA\cdot]_{QSS}[BrMA], \quad (4.3d) \\
&+ k_f([BrMA]_{mf} - [BrMA])),
\end{aligned}$$

where $[MA\cdot]_{QSS}$ is given by

$$[MA\cdot]_{QSS} = \left(k_{D8}[BrMA] + \sqrt{(k_{D8}[BrMA])^2 + 8k_{D6}k_{C11}[Ce(IV)]}\right)/(4k_{C11}), \quad (4.4)$$

and $k_{C11} = 3.0 \cdot 10^9/(Ms)$. We append a multiplicative factor α to (4.3d) for convenience.

A short comment about the parameter values used in this chapter is necessary. In sections 3 and 4, we analyze the regimes of low flow rate and high flow rate complexity using parameter values taken from experiments. The *low flow parameters* used by the Texas group [99, 86, 87] are given by

$$([\mathrm{MA}], [\mathrm{BrO_3^-}], [\mathrm{Ce(III)}]_{\mathrm{mf}}, [\mathrm{H_2SO_4}]) = (0.25, 0.1, 0.83 \cdot 10^{-3}, 0.2),$$

where all concentrations are given in molarity, i.e. 1 M = 1 mol/dm^3. The *high flow rate parameters* are based on the early studies by Hudson and coworkers [62, 63]

$$([\mathrm{MA}], [\mathrm{BrO_3^-}], [\mathrm{Ce(III)}]_{\mathrm{mf}}, [\mathrm{H_2SO_4}]) = (0.3, 0.14, 1.0 \cdot 10^{-3}, 0.2).$$

We use the subscript $[\mathrm{Ce(III)}]_{\mathrm{mf}}$ to distinguish between the concentration of Ce(III) in the reactor tank and the concentration of Cerium ions in the mixed-feed. The sulfuric acid concentration $[\mathrm{H_2SO_4}]$ is converted into a proton concentration $[\mathrm{H^+}]$ using Table I in Robertson and Dunford [95]. We reproduce relevant portions of this table in Table 4.2. For $[\mathrm{H_2SO_4}] = 0.2$ M, the proton concentration is given by $[\mathrm{H^+}] = 0.26$ M. In section 5, we use experimental parameters as model parameters; many experimental $[\mathrm{H_2SO_4}]$ values from Table 4.6 can be found in Table 4.2. The $\mathrm{H_2SO_4}$ concentration of the studies that cannot [119, 98, 61, 1, 64, 104] is computed using a linear interpolation of the values listed in Table 4.2. Finally, in [53], all mixed-feed concentrations of the variable species are set to zero except Ce(III). However, given [32], we set the following mixed-feed concentrations $[\mathrm{HBrO_2}]_{\mathrm{mf}} = 0$ M, $[\mathrm{Br^-}]_{\mathrm{mf}} = 10^{-7}$ M, and $[\mathrm{BrMA}]_{\mathrm{mf}} = 10^{-8}$ M.

In the previous chapter, we identified five dynamical regions of behavior in the BZ reaction: the thermodynamic branch of equilibria, the flow branch of equilibria, low flow rate complexity, the P_1 regime of relaxation oscillations,

$[H_2SO_4]$ M	$[H^+]$ M	$[H_2SO_4]$ M	$[H^+]$ M
0.1	0.132	0.7	0.874
0.2	0.260	0.8	0.992
0.3	0.383	0.9	1.11
0.4	0.508	1.0	1.24
0.5	0.631	1.5	1.82
0.6	0.754	2.0	2.46

Table 4.2: Proton concentration in a sulfuric acid solution. Data taken from Robertson and Dunford [95].

high flow rate complexity, and the flow branch of equilibria. We seek a mathematical description of the mechanisms generating complexity using GSPT. At low flow rates, we find MMOs in the absence of an equilibrium point. The SAOs of the MMOs have an hourglass shape, consistent with dynamic Hopf bifurcation. At high flow rates, we find that interactions between an attracting slow manifold and the unstable manifold of an equilibrium point shape the dynamics. Following Györgyi and Field [53], we analyze the low flow rate and high flow rate complexity using Model D_{QSS} and Model D_{EQ}, respectively.

4.2.1 Scaling Model D

As mentioned above, the separation of time scales in Model D may vary in different regions of phase space. We measure the local separation of time scales using the variational equation, which is given by

$$\dot{\delta z}(t) = DF(z(t))\delta z(t), \tag{4.5}$$

where $z \in \mathbb{R}^4$ represents the four chemical species, and $F(z)$ is the right-hand side of equation (4.3). Specifically, the eigenvalues of DF measure the local rates of contraction and expansion. For $z \in \mathbb{R}^4$ near a slow manifold, the eigenvector associated with the eigenvalue of smallest magnitude corresponds to the direction

of weakest expansion or contraction, i.e., the direction of motion along a slow manifold. Therefore, the slow variable can be approximated by a linear combination of the dynamic variables whose coefficients are given by the weakest left eigenvector. Let w be the eigenvector corresponding to the eigenvalue with the smallest absolute value λ_4 of the matrix DF, i.e. $w \cdot DF = \lambda_4 w$. We approximate the slow variable

$$[s] = [s](w) = w_1[\mathrm{HBrO_2}] + w_2[\mathrm{Br^-}] + w_3[\mathrm{Ce(III)}] + w_4[\mathrm{BrMA}]. \tag{4.6}$$

At low flow rates, we find many small rapid oscillations in the $HBrO_2$, Br^-, and Ce(III) concentrations for trajectories with SAOs. While the BrMA concentration does not rapidly oscillate, it is not uniformly monotone. However, this indicates that a transformation of the system may be necessary to determine the slow variable. As a first approximation, consider [BrMA] a slow variable and compute the family of equilibria of the approximate fast system (4.3, $\alpha = 0$). The one-dimensional family of equilibria make up the critical manifold. We find a Hopf bifurcation of the fast subsystem near the SAOs of the full system. We compute the eigenvalues of DF at this dynamic Hopf bifurcation. This allows us to replace [BrMA] in Model $\mathrm{D_{QSS}}$ by the quantity

$$[\mathrm{BrMA}] = ([s] - w_1[\mathrm{HBrO_2}] - w_2[\mathrm{Br^-}] - w_3[\mathrm{Ce(III)}])/w_4. \tag{4.7}$$

We differentiate equation (4.6), while preserving the artificial time scale ratio parameter α, and append it to (4.3a-4.3c)

$$\dot{[s]} = \alpha(w_1[\mathrm{H\dot{B}rO_2}] + w_2[\dot{\mathrm{Br}}^-] + w_3[\mathrm{Ce}(\dot{\mathrm{III}})] + w_4[\dot{\mathrm{BrMA}}]). \tag{4.8}$$

We refer to system (4.3a-4.3c, 4.7–4.8) as the *full system* and (4.3a-4.3c, 4.7–4.8, $\alpha = 0$) as the *layer equation*. At high flow rates, we identify [BrMA] as a slow

variable without any need to rescale the system. This is discussed in the next section.

Figure 4.2 shows that the critical manifolds at low and high flow rates have qualitatively different shapes. For the purposes of studying Model D at the Györgyi and Field parameters in sections 3 and 4, let $k_f \in [10^{-4}, 4 \cdot 10^{-4}]$ be considered low flow rates, and $k_f \in [9.0 \cdot 10^{-4}, 1.5 \cdot 10^{-3}]$ be considered high flow rates. Figure 4.2(a) shows a cartoon critical manifold $\mathcal{S}$ for Model D_{QSS} for low flow rates. The critical manifold is S-shaped, separating $\mathcal{S}$ into upper, middle and lower branches by two folds, which denoted L_1 and L_2. The branches of the critical manifold are denoted $\mathcal{S}_u$, $\mathcal{S}_m$, $\mathcal{S}_\ell$, respectively. For each flow rate, there is a dynamic Hopf bifurcation located on the upper and lower branches, which are denoted H_u and H_ℓ. Figure 4.2(b) shows the critical manifold for Model D_{EQ} at high flow rates. Again, there are two dynamic Hopf bifurcations on the critical manifold, however, the critical manifold is monotone increasing, without any turning points.

The stability of each branch in the layer equation is given by a triplet of the form $(\pm, \pm, \pm)$ where each $\pm$ indicates the sign of the real part of the eigenvalues of the equilibria that comprise the branch. For each flow rate considered in this section there is a unique equilibrium of the full system. We are unaware of the existence of multiple chemically relevant equilibria at any parameter values in this analysis. The stability of the equilibria of the full system are found by appending a $(-)$ to each triplet in Figure 4.2. Computing the variational equation in regions of phase space near the attractors, we find a large negative eigenvalue whose magnitude is at least on order of magnitude larger than the others. This suggests that the underlying attractor of the full system may be contained

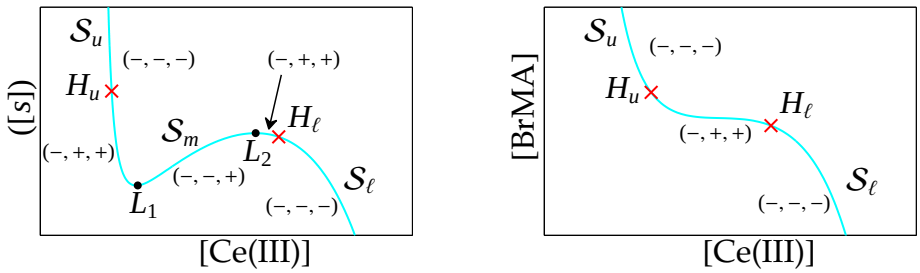

(a) Low flow rates. (b) High flow rates.

Figure 4.2: Cartoons of the critical manifolds at low and high flow rates: (a) Model D_{QSS} at low flow rates has a critical manifold with three branches. The branches of the critical manifold are denoted: upper branch, $\mathcal{S}_u$; middle branch, $\mathcal{S}_m$; lower branch, $\mathcal{S}_\ell$. The Hopf bifurcations H_u and H_ℓ are indicated by a red cross. The limit points L_1 and L_2 are indicated by a black dot. The triplets containing + and − give the sign of the eigenvalues on that segment of $\mathcal{S}$. (b) Model D_{EQ} at high flow rates has a monotone critical manifold.

in a lower dimensional submanifold. We make no attempt to use dimension reduction methods to compute this manifold.

4.3 High flow rate complexity

High flow rate complexity in the BZ reaction is characterized by the alternation of periodicity and aperiodicity for flow rates larger than the P_1 relaxation oscillation regime. Near $k_f = 1.117 \cdot 10^{-3}$, a relaxation oscillation undergoes a PD bifurcation, resulting in a 2^0 orbit. As the flow rate is increased near $k_f = 1.18 \cdot 10^{-3}$, the system has a chaotic attractor that concatenates 1^0 and 1^1 MMO segments. The alternation of periodic and aperiodic MMOs continues until $k_f = 1.35535 \cdot 10^{-3}$, where the MMOs are no longer observed. Oscillations of the system end at a supercritical Hopf bifurcation at $k_f = 1.388120 \cdot 10^{-3}$. A family of stable periodic orbits emanates from this Hopf bifurcation as flow rates decrease. This fam-

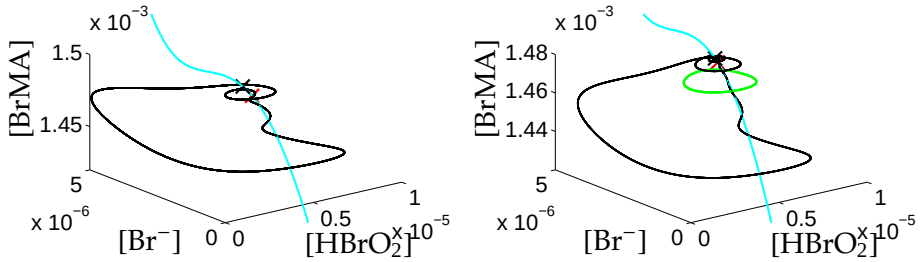

(a) $k_f = 1.31 \cdot 10^{-3}$ (b) $k_f = 1.35 \cdot 10^{-3}$

Figure 4.3: MMOs in phase space for two high flow rates. For each MMO, the critical manifold is shown in cyan, the dynamic Hopf bifurcation is indicated by a red cross, and the equilibrium point of the full system is indicated by a black cross. (a) $k_f = 1.31 \cdot 10^{-3}$. (b) $k_f = 1.35 \cdot 10^{-3}$. Additionally, a periodic orbit born from the Hopf bifurcation of the full system is show in green.

ily loses undergoes a PD bifurcation near $k_f \approx 1.348 \cdot 10^{-3}$, and loses stability for slightly smaller flow rates. Therefore, there is a region of bistability of small amplitude periodic orbits and MMOs for flow rates $k_f \in [1.348 \cdot 10^{-3}, 1.35535 \cdot 10^{-3}]$.

Figure 4.3 shows two high flow rate MMOs in phase space at $k_f = 1.31 \cdot 10^{-3}$ and $k_f = 1.35 \cdot 10^{-3}$. At each flow rate, we compute a critical manifold of the approximate fast subsystem given by equation (4.3, $\alpha = 0$). For each subfigure, the equilibria of the fast subsystem are shown in cyan, a dynamic Hopf bifurcation is indicated by a red cross, and the equilibrium point of the full system is indicated by a black cross. Because $k_f = 1.35 \cdot 10^{-3}$ lies in an interval of bistability of small amplitude periodic orbits and MMOs, a periodic orbit is shown in green. For each MMO, the SAOs are initiated near [BrMA] = $1.44 \cdot 10^{-3}$. The critical manifold is fully attracting here; the eigenvalues associated with the equilibria of the fast subsystem all have negative real part. This is consistent with the decreasing amplitude of the SAOs that are initiated in this region. The trajectory is being attracted to a slow manifold which passes by the dynamic Hopf bifurcation of the fast subsystem at [BrMA] = $1.490149 \cdot 10^{-3}$ for $k_f =$

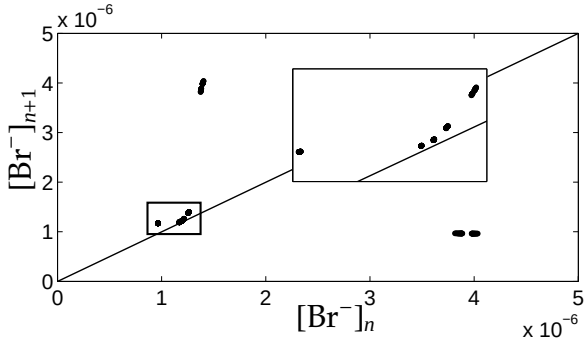

Figure 4.4: Next maximum-amplitude map for Model D_{EQ} at $k_f = 1.35535 \cdot 10^{-3}$. A saddle-node bifurcation occurs for $k_f \in (1.35535 \cdot 10^{-3}, 1.35536 \cdot 10^{-3})$.

$1.31 \cdot 10^{-3}$ and [BrMA] $= 1.490061 \cdot 10^{-3}$ for $k_f = 1.35 \cdot 10^{-3}$.

After the trajectory passes by the dynamic Hopf bifurcation, the SAOs begin to grow in amplitude. However, the trajectory begins to interact with an equilibrium point of the full system. This is the major difference between the high and low flow rate regimes in Model D: there is no interaction with an equilibrium point at low flow rates. As the flow rate increases, the distance between the equilibrium point and the dynamic Hopf bifurcation decreases. Therefore, trajectories pass by the dynamic Hopf bifurcation and are funneled into a small neighborhood of the equilibrium point. The equilibrium point is of saddle type for flow rates before the Hopf bifurcation of the full system, and is fully stable after the Hopf bifurcation. The trajectory leaves the neighborhood of the equilibrium by following its unstable manifold. Therefore, the increasing amplitude of the SAOs observed in this region is not due to the repulsion along the critical manifold, but is due to interaction with the unstable manifold of the equilibrium point.

The 1^n MMOs observed at high flow rates are no longer observed at $k_f = 1.35536 \cdot 10^{-3}$. Evidence suggests that the MMOs annihilated in a saddle-node

[BrMA]\k_f	$1.25 \cdot 10^{-3}$	$1.35 \cdot 10^{-3}$
$1.44 \cdot 10^{-3}$	-3.010416 -0.037189 ± 0.069749i -0.005306	-3.005663 -0.036947 ± 0.069664i -0.005324
$1.48 \cdot 10^{-3}$	-2.483724 -0.008247 ± 0.058563i -0.008290	-2.478618 -0.007943 ± 0.058383i -0.008338

Table 4.3: Eigenvalues of the matrix *DF* associated with the variational equation computed at points on the critical manifold. The values of [BrMA] for the two points are listed on the left vertical column, and the flow rates are listed on the top row.

bifurcation near $k_f = 1.35535 \cdot 10^{-3}$. Figure 4.4 shows a next maximum-amplitude (NMA) map at this flow rate. The NMA shows three groups of points for this particular orbit, one of which is near the main diagonal. The NMA map indicates that the system is near a saddle-node bifurcation. We detect no large periodic orbits at $k_f = 1.35536 \cdot 10^{-3}$, indicating that the large MMO has been annihilated or become unstable. For larger flow rates, the system has only small sinusoidal periodic orbits, which terminate in the flow branch of equilibria at $k_f = 1.388120 \cdot 10^{-3}$.

For all MMOs in this regime, the SAOs are initiated near [BrMA] = $1.44 \cdot 10^{-3}$ and are terminated near [BrMA] = $1.48 \cdot 10^{-3}$. We compute the eigenvalues of the matrix *DF* associated with the variational equation along the critical manifold at these BrMA concentrations for two flow rates $k_f \in \{1.25 \cdot 10^{-3}, 1.35 \cdot 10^{-3}\}$. The eigenvalues are tabulated in Table 4.3. For [BrMA] = $1.44 \cdot 10^{-3}$, there is approximately an order of magnitude difference between each of the real parts of the eigenvalues (two are complex conjugates). With a clear separation of time scales, we expect to be able to apply the theory of GSPT in this region. What we find in the full system is consistent with the predictions of GSPT: we find that large regions of phase space are funneled into a neighborhood of the critical

manifold. As the flow rate increases, the contraction prevents trajectories from having more than one large spike. For flow rates higher than $k_f = 1.23 \cdot 10^{-3}$, no MMOs has two concurrent LAOs.

Table 4.3 shows that the eigenvalues associated with the critical manifold are nearly constant throughout the the high flow rate regime. This means that the attraction to the critical manifold in phase space is insensitive to the flow rate. However, the qualitative nature of the MMOs changes as the flow rate increases: the amplitude of the SAOs decreases dramatically as the flow rate increases. This is due solely to the decrease in the speed of the vector field along the critical manifold. On the critical manifold, the largest component of the vector field is $d[\text{BrMA}]/dt$. At $[\text{BrMA}] = 1.44 \cdot 10^{-3}$, $d[\text{BrMA}]/dt = 4.552198 \cdot 10^{-7}$ and $d[\text{BrMA}]/dt = 3.096225 \cdot 10^{-7}$ for the flow rates of $k_f = 1.25 \cdot 10^{-3}$ and $k_f = 1.35 \cdot 10^{-3}$, respectively. Therefore, the trajectory spends more time near the critical manifold as the flow rate increases, causing the qualitative change in the MMOs.

At $[\text{BrMA}] = 1.48 \cdot 10^{-3}$, we find that three eigenvalues have approximately the same real parts that are of the same order of magnitude. In this region of phase space, our choice of fast subsystem may be incorrect – a system with three slow variables and one fast variable may be more appropriate. This leads to an ambiguity in classifying the Hopf bifurcation of full system at $k_f = 1.388120 \cdot 10^{-3}$. This Hopf bifurcation coincides with a dynamic Hopf bifurcation of the three-dimensional fast subsystem (4.3, $\alpha = 0$), so it can be classified as a dynamic Hopf bifurcation. However, Guckenheimer [43] shows that a Hopf bifurcation of a slow-fast system is consistent with singular Hopf bifurcation if the eigenvector associated with the pure imaginary eigenvalues has both slow

and fast components. The eigenvector associated with the terminal Hopf bifurcation at high flow rates is given by

$$\begin{pmatrix} -0.027849 \\ 0.011381 \\ -0.107715 \\ 0.750247 \end{pmatrix} \pm \begin{pmatrix} -0.215565 \\ 0.050280 \\ 0.612883 \\ 0 \end{pmatrix}.$$

If we consider the system to have one slow and three fast variables, then this eigenvector fits the criteria for a singular Hopf bifurcation. Without well defined fast- and slow subsystems, and a singular parameter representing the separation of time scales, a classification of this Hopf bifurcation using slow-fast theory cannot be made.

4.4 Low flow rate complexity

Low flow rate complexity of the BZ reaction is the regime of complex trajectories for flow rates between the thermodynamic branch of equilibria and the P_1 region of relaxation oscillations. The bifurcation diagram for Model D_{QSS} at low flow rates is shown in Figure 4.5. It shows intersections of the attractor with the cross section $[\text{Ce(III)}] = 8.307558 \cdot 10^{-4}$ as $d[\text{Ce(III)}]/dt > 0$ for flow rates $k_f \in [1.3 \cdot 10^{-4}, 3.4 \cdot 10^{-4}]$. We choose this cross section because it intersects the SAOs of the MMOs in this flow rate regime. At $k_f = k_{H_1} = 1.057989 \cdot 10^{-4}$, there is a supercritical Hopf bifurcation. For $k_f < k_{H_1}$, the thermodynamic branch of equilibria is globally stable. At k_{H_1} a stable family of periodic orbits is born. The diameter of the periodic orbits grows as the flow rate increases. Near $k_f = 1.3 \cdot 10^{-4}$, stable MMOs with a large number of SAOs appear. This can be

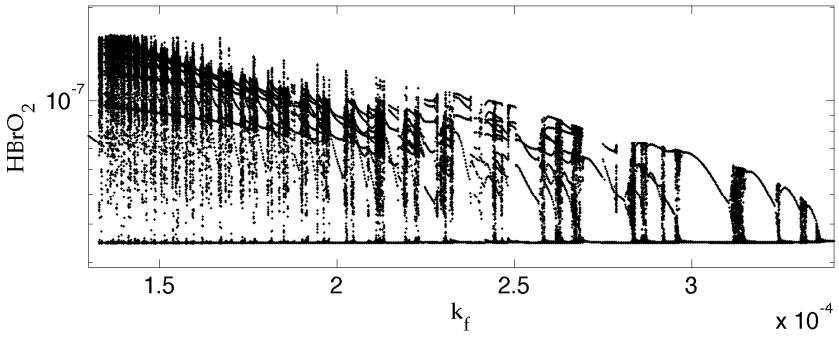

Figure 4.5: Bifurcation diagram for $k_f \in [1.3 \cdot 10^{-4}, 3.4 \cdot 10^{-4}]$. The diagram was calculated using 1001 evenly spaced parameter values, with intersections from 4 trajectories at each parameter plotted. The intersections with the hyperplane defined by [Ce(III)] = $8.307558 \cdot 10^{-4}$ as [Ce(III)] is increasing are plotted.

seen in Figure 4.5 as the attractor widens from a single intersection to many intersections. The alternation of periodic and aperiodic behavior at low flow rates is evident in the bifurcation diagram: for a particular flow rate, a small number of intersections indicates periodicity while a large number of intersections is indicative of chaos. As the flow rate increases, the number of SAOs decreases. Near $k_f = 3.3 \cdot 10^{-4}$, the system transitions to the P_1 relaxation oscillations regime as low flow SAOs cease to appear.

Unlike the high flow rate regime, the SAO region of phase space in the low flow regime can be transformed into slow-fast coordinates. We emphasize that this transformation is valid only in the region of phase space where SAOs occur; other scalings may be appropriate in other regions of phase space. As described in section 2, consider [BrMA] a slow variable. Using this approximation, we can define an approximating fast subsystem using equation (4.3, $\alpha = 0$). Figure 4.6(a) shows a 1^{18} MMO in phase space found at $k_f = 1.37 \cdot 10^{-4}$. The one-dimensional critical manifold of the approximate fast subsystem is shown in cyan. A dynamic Hopf bifurcation is located on the critical manifold at

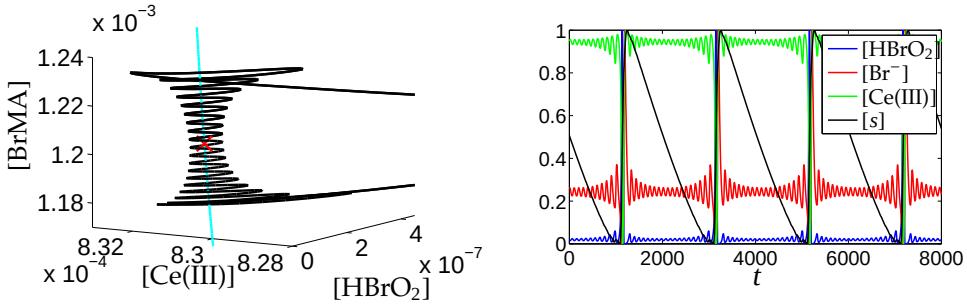

(a) Phase Space (b) Normalized

Figure 4.6: (a) A 1^{18} MMO in phase space at $k_f = 1.37 \cdot 10^{-4}$ in the original Model D_{QSS} coordinates, i.e. equation (4.3). The critical manifold is shown in cyan. A Hopf bifurcation of the layer equation is indicated by a red cross. (b) The 1^{18} MMO normalized to the interval $[0, 1]$ by an affine transformation in the transformed coordinate system, i.e. equation (4.3a–4.3c, 4.7–4.8, $\alpha = 0$). The minima and maxima of each concentration are given in Table 4.4.

[BrMA] = $1.202370 \cdot 10^{-3}$ and is indicated by a red cross.

To properly scale the system, we must compute the eigenvalues and eigenvectors of DF associated with the variational equation (4.5) near a slow manifold. As a first approximation to the slow manifold, we choose points on the critical manifold to compute w. We vary both the flow rate and the point on the critical manifold at which w is calculated. In the SAO region of phase space, the eigenvector associated with the smallest left eigenvalue of DF is insensitive to the location on the critical manifold at which the eigenvalues are computed. A transformation of the system into slow-fast coordinates makes the slow variable (4.6) monotone throughout the SAO region. We found that the monotonicity of the slow variable is unaffected by the choice of location or flow rate. This allows us to rescale the system by choosing a point in phase space at a particular flow rate. For convenience, we've chosen to compute w computed at the location of the dynamic Hopf bifurcation [BrMA] = $1.204033 \cdot 10^{-3}$

at the flow rate of $k_f = 2.0 \cdot 10^{-4}$. These choices reflect the fact that the SAOs are roughly symmetric about the dynamic Hopf bifurcation and because $k_f = 2.0 \cdot 10^{-4}$ is roughly in the middle of the low flow rate complexity regime. At $k_f = 2.0 \cdot 10^{-4}$, the eigenvector corresponding to the smallest eigenvalue is given by $w = (0.908367056, -0.235697237, 0.277281183, 0.205988466)$. Roughly interpreted,

$$4HBrO_2 - Br^- + Ce(III) + BrMA$$

can be considered a slowly reacting chemical quantity.

Figure 4.6(b) shows each individual species of the 1^{18} MMO computed using this rescaling. The slow quantity is monotone while the other species are rapidly oscillating. Each individual species has been normalized to the interval [0,1] using an affine transformation for comparison. The maxima and minima of the species are given in Table 4.4.

	$[HBrO_2]$ (M)	$[Br^-]$ (M)	[Ce(III)] (M)	[BrMA] (M)
min	$3.483408 \cdot 10^{-8}$	$4.293553 \cdot 10^{-7}$	$8.096239 \cdot 10^{-4}$	$4.728733 \cdot 10^{-3}$
max	$5.290276 \cdot 10^{-6}$	$6.328551 \cdot 10^{-6}$	$8.323484 \cdot 10^{-4}$	$4.842014 \cdot 10^{-3}$

Table 4.4: Maximum and minimum values of the normalized concentrations seen in Figure 4.6(b).

Figure 4.7(a-b) shows a 1^{15} MMO in phase space at $k_f = 1.425 \cdot 10^{-4}$. The critical manifold of the approximate fast subsystem is shown in cyan. A dynamic Hopf bifurcation, indicated by a red cross, is found on the critical manifold at $[s] = 4.781064 \cdot 10^{-4}$. As s decreases, the stability of the equilibrium of the fast subsystem changes. For $[s] > 4.781064 \cdot 10^{-4}$ on the critical manifold, the equilibria of the layer equation are stable; all eigenvalues have negative real part. At the dynamic Hopf bifurcation, a pair of complex eigenvalues of the layer equation cross the imaginary axis, and for $[s] < 4.781064 \cdot 10^{-4}$, the equilibria of

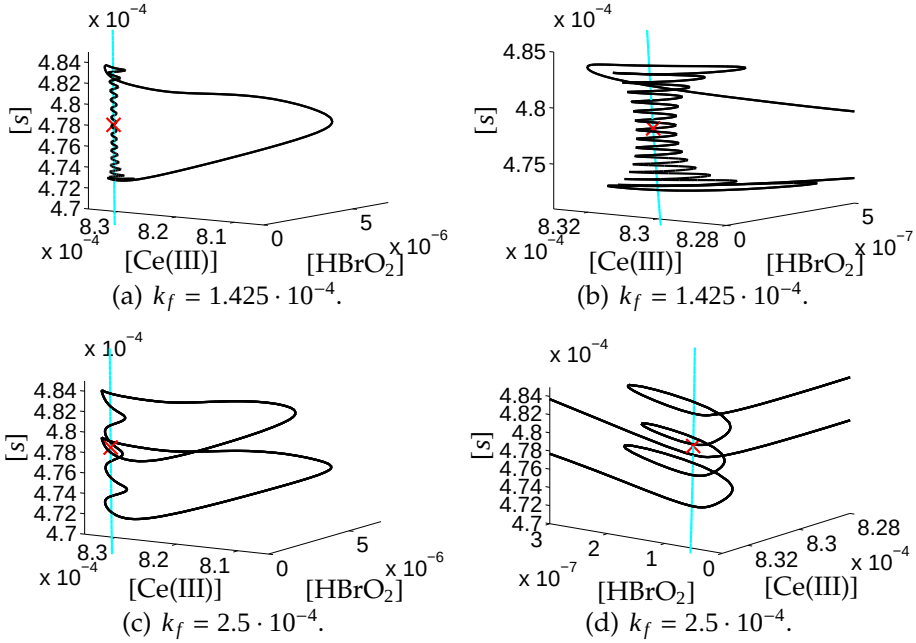

(a) $k_f = 1.425 \cdot 10^{-4}$. (b) $k_f = 1.425 \cdot 10^{-4}$.

(c) $k_f = 2.5 \cdot 10^{-4}$. (d) $k_f = 2.5 \cdot 10^{-4}$.

Figure 4.7: MMOs at different flow rates shown in phase space. (a)-(b) A 1^{15} MMO at $k_f = 1.425 \cdot 10^{-4}$. (c)-(d) A 2^3 MMO at $k_f = 2.5 \cdot 10^{-4}$. Subfigures (b) and (d) show enhanced views of the SAOs seen in (a) and (c).

layer equation are unstable. As a result, trajectories that approach the critical manifold near $[s] > 4.781064 \cdot 10^{-4}$ become attracted to it and begin to oscillate around it with decreasing amplitude. As the trajectory traverses the region near the Hopf bifurcation point, the critical manifold becomes unstable and oscillations around the critical manifold grow in amplitude. The hourglass pattern of SAOs is formed by the combination of stability of the critical manifold and the nearly constant speed in the slow direction near the critical manifold. The SAOs are roughly centered around the dynamic Hopf bifurcation and the minimum amplitude of the SAOs occurs near the the dynamic Hopf bifurcation. This can be seen clearly in Figure 4.7(b), which shows an enlarged view of the SAOs near the critical manifold.

Figure 4.7(c-d) shows a 2^3 MMO for the flow rate $k_f = 2.5 \cdot 10^{-4}$. For both flow

$[s]\backslash k_f$	$1.425 \cdot 10^{-4}$	$2.5 \cdot 10^{-4}$
$4.72 \cdot 10^{-4}$	-0.447720 0.003449 ± 0.069749i -0.000304	-0.447841 0.003703 ± 0.062925i -0.000413
$4.84 \cdot 10^{-4}$	-2.483724 -0.002895 ± 0.058563i -0.000253	-0.448291 -0.002649 ± 0.066981 -0.000361

Table 4.5: Eigenvalues of the matrix DF associated with the variational equation computed at points on the critical manifold for the two flow rates shown in Figure 4.7. The values of $[s]$ for the two points are listed on the left vertical column, and the flow rates are listed on the top row.

rates in Figure 4.7, the SAOs are initiated near $[s] = 4.84 \cdot 10^{-4}$ and are terminated near $[s] = 4.72 \cdot 10^{-4}$. Table 4.5 gives the eigenvalues of the equilibria of the layer equation at these locations on $\mathcal{S}$ for the flow rates $k_f \in \{1.425 \cdot 10^{-4}, 2.5 \cdot 10^{-4}\}$. The table shows that the real parts of the complex eigenvalues, which determine the attraction to and repulsion from $\mathcal{S}$, differ by roughly 10%. This difference is not sufficient to explain the disparity in the number of SAOs observed at the two flow rates. Examining the $[\dot{s}]$ terms at $[s] = 4.8 \cdot 10^{-4}$, where the SAOs are initiated, we find that $[\dot{s}] = 1.018501 \cdot 10^{-8}$ and $[\dot{s}] = 1.018501 \cdot 10^{-8}$ at $k_f = 1.425 \cdot 10^{-4}$ and $k_f = 2.5 \cdot 10^{-4}$, respectively. In the dynamic Hopf normal form, the separation of time scales is directly proportional to the speed at which the trajectory passes through the region. Therefore, we find that the separation of time scales is proportional to the flow rate. As the flow rate increases, the system becomes less stiff and spends less time in the SAO region. Further evidence of this is given by the nearly constant magnitude of the small oscillations at $k_f = 2.5 \cdot 10^{-4}$. This behavior is consistent with dynamic Hopf bifurcation when the separation of time scales is weak [25]. We also note that the imaginary parts of the complex eigenvalues listed in Table 4.5 are approximately an order of magnitude greater than the real parts. Contrast this with the low flow rate case,

where the real and imaginary parts were of the same order. This difference results in less attraction to the critical manifold with a high rate of oscillation, creating more SAOs at low flow rates than at high flow rates.

An important aspect of the MMOs in this regime is that the SAOs are generated in the absence of an equilibrium point. For the 1^{15} MMO shown in Figure 4.7, the minimum s-coordinate is roughly $[s] = 4.72 \cdot 10^{-4}$. However, the equilibrium point of the full system is located on the critical manifold at $[s] = 4.540637 \cdot 10^{-4}$. At no point does the trajectory interact with the equilibrium point. This is true for any MMO at low flow rates – the equilibrium point and the MMO are separated by a large distance.

The rescaling used in this analysis is not a globally valid rescaling; the dynamic variable s serves as a slow variable in the SAO region, however, the fast resetting of the slow variable indicates that s is not a valid globally slow variable. The coordinate transformation presented above does not produce a dynamic Hopf normal form. Although we cannot state with absolutely certainty that a dynamic Hopf bifurcation is responsible for the low flow rate behavior, nearly all evidence presented in this section is compatible with dynamic Hopf bifurcation. The changing magnitude of the amplitude of the SAOs and their relative position to the Hopf bifurcation make it clear that a dynamic Hopf bifurcation is the primary mechanism responsible for the creation of the MMOs.

4.4.1 Global return mechanism

The 2^3 MMO shown in Figure 4.7(c-d) shows that the global return mechanism at low flow rates can be more complicated than a simple resetting of the slow

variable s. More precisely, the resetting of the slow variable is the difference between the $\max(s(t)) - \min(s(t))$ over a large excursion. As the flow rate increases, the resetting of the s coordinate over a large excursion decreases and more than one LAO takes place between SAOs.

Consider the approximate fast subsystem (4.3a–4.3c, 4.7, $\dot{s} = 0$) at $k_f = 2.62 \cdot 10^{-4}$. In the layer equation, there is a family of limit cycles born at a supercritical dynamic Hopf bifurcation at $[s] = 4.787292 \cdot 10^{-4}$. The bifurcation diagram for the family of limit cycles is shown in Figure 4.8. The dynamic Hopf bifurcation is denoted H_u and indicated by a grey line. We note that the curve of limit cycles does not reach the Hopf bifurcation H_u due to convergence issues of the continuation methods used to calculate the curve. We were unable to continue limit cycles from the Hopf bifurcation; a limit cycle computed using forward integrations was used as an initial condition for the continuation calculation in AUTO.

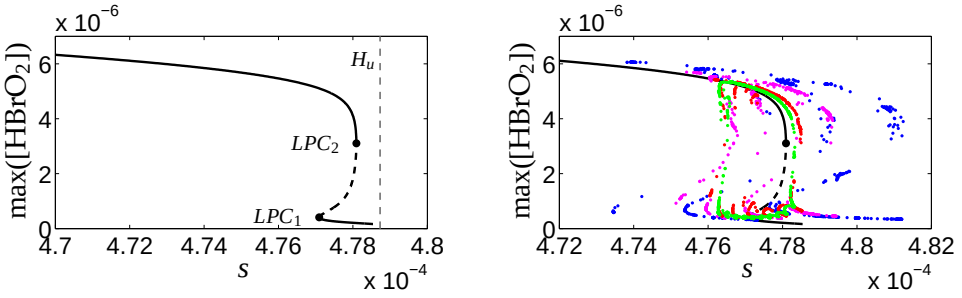

(a) Layer equation limit cycles

(b) max([$HBrO_2$]) for several trajectories

Figure 4.8: (a) The bifurcation diagram of limit cycles of the layer equation at $k_f = 2.62 \cdot 10^{-4}$. The supercritical Hopf bifurcation H_u at $[s] = 4.787292 \cdot 10^{-4}$ is indicated by a dotted grey line. Two limit point of cycles bifurcations, LPC_1 and LPC_2, separate the family of limit cycles into stable small, saddle-type, and stable large families of limit cycles. (b) Plots of s vs. the maxima of [$HBrO_2$] for the values of $\alpha \in \{1.0, 0.389, 0.114, 0.06\}$ plotted in blue, magenta, red, and green, respectively, at $k_f = 2.62 \cdot 10^{-4}$, overlaid on top of the bifurcation diagram of the limit cycles of the layer equation.

The family of limit cycles has two limit points: the family becomes unstable at LPC_1 at $[s] = 4.770931 \cdot 10^{-4}$ and regains stability at LPC_2 at $[s] = 4.780915 \cdot 10^{-4}$. There is a region of bistability of limit cycles in the layer equation between the limit point bifurcations. We differentiate the two stable branches of limit cycles by denoting them "large" and "small" in reference to their relative amplitudes. The large branch of stable limit cycles persists for decreasing s and forms a cylinder of limit cycles in the full four-dimensional phase space. This family is annihilated at a supercritical Hopf bifurcation at $[s] = 4.578102 \cdot 10^{-4}$. The large branch of stable limit cycles plays a role in the global dynamics of the system: when making large excursions, trajectories follow the stable cylinder of large limit cycles.

Consider the 1^6 MMO at $k_f = 1.8 \cdot 10^{-4}$ shown in black in Figure 4.9. Since the SAOs of the 1^6 MMO are terminated near $s = 4.725 \cdot 10^{-4}$, the stable large limit cycle of the layer equation for $[s] = 4.73 \cdot 10^{-4}$ is also shown (in its layer) in red. Figure 4.9(b-d) shows the MMO of the full system and the limit cycle projected onto the three coordinate planes of the fast subsystem. The MMO of the full system appears to follow the limit cycles of the layer equation; in each projection, the large excursion of the MMO is nearly indistinguishable from the limit cycle of the layer equation. This similarity is strong evidence that the global return mechanism is related to the cylinder of limit cycles of the layer equation.

Further evidence of this can be seen in Figure 4.8(b). Model D_{QSS} appears to have chaotic orbits at $k_f = 2.62 \cdot 10^{-4}$ and $\alpha \in \{1.0, 0.389, 0.114, 0.06\}$. For each trajectory, plots of the s coordinate vs. the local maxima of $[HBrO_2]$ are shown. The maxima for each α are plotted in blue, magenta, red, and green, respectively. As $\alpha \to 0$, we find that the maxima of the $[HBrO_2]$ coordinate tends toward the

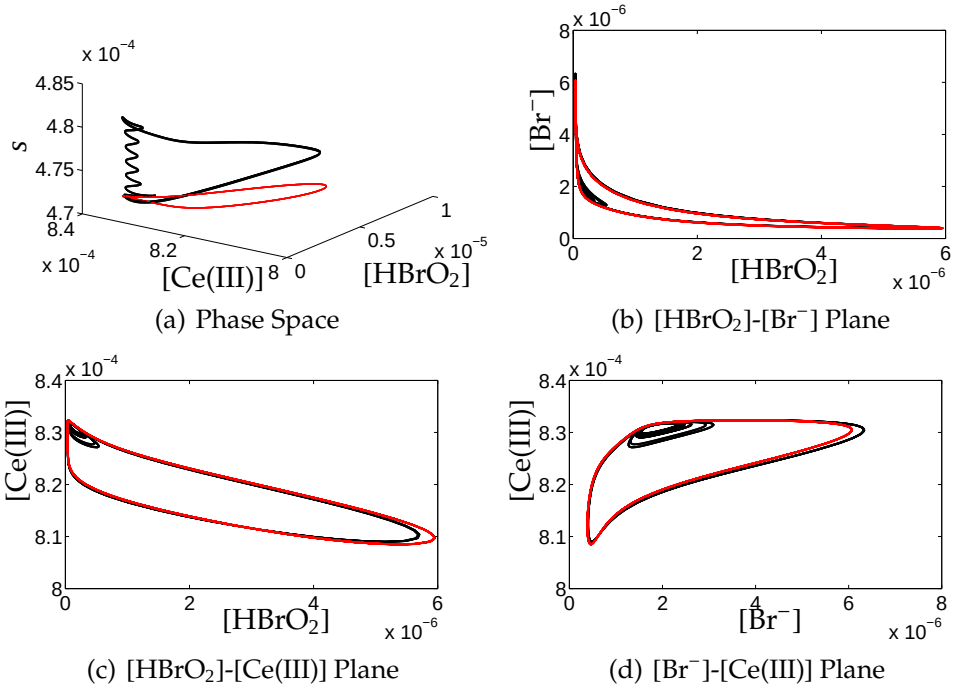

(a) Phase Space

(b) $[HBrO_2]$-$[Br^-]$ Plane

(c) $[HBrO_2]$-[Ce(III)] Plane

(d) $[Br^-]$-[Ce(III)] Plane

Figure 4.9: A stable 1^6 MMO of Model D_{QSS} at $k_f = 1.8 \cdot 10^{-4}$ and a large amplitude stable limit cycle of the layer equation at $[s] = 4.72 \cdot 10^{-4}$. (a) The MMO and the layer equation limit cycle in phase space. (b-d) The MMO and the layer equation limit cycle projected onto the three coordinate planes of the fast subsystem.

family of large limit cycles in Figure 4.8(a). We do not attempt to show that the family of limit cycles perturbs smoothly in the full system as a normally hyperbolic invariant manifold, however, the evidence presented above shows that the family plays a role in shaping the global dynamics of the system.

4.5 Catalog of Model D behaviors

In this section, we compare the dynamics of Models D_{EQ} and D_{QSS} with experimental data. The goal of this section is to catalog the wide range of behaviors that the model exhibits. Direct comparison to experiments is often difficult for

several reasons. First, not all external parameters are represented by Model D, such as the stirring rate and the temperature. We do not know of any study which takes these factors into account. Second, the flow rate at which an individual time series is measured may be omitted. This is particularly true of studies that compare experimental sequences of MMOs to Farey sequences, due to the large number of time series involved in the study. Third, not all studies use the same catalyst. Because Ce(III), ferroin and manganese react with different rate constants, direct comparison between experiment and numerical simulations is not possible. Because Model D only models Cerium catalyzed reactions, we adopt the convention of treating each experiment as if it were catalyzed by Cerium. To the author's knowledge, direct experimental comparison between trajectories of Cerium and other catalyzed reactions have not been completed. Finally, a comprehensive comparison of numerical simulations with experimental work at a single set of parameters requires an extensive list of experimental time series at these parameters. Such a list is rarely included in the experimental literature, so we are often forced to compare one or two experimental time series with the numerical simulations. This makes it difficult to determine with certainty that the numerical simulations replicate the observed experimental behavior. Despite this difficulty, Model D, either Model D_{EQ} or Model D_{QSS}, replicates nearly all of the experimentally observed behavior described in Chapter 3.

Table 4.6 contains sets of parameters that were used in our effort to compare numerical and experimental data. This list is not meant to be exhaustive; some studies, [75, 76] for example, have used many sets of parameters and list ranges for certain variables, instead of specifying values. Table 4.6 also indicates whether either Model D_{EQ} or Model D_{QSS} replicates the experimentally observed

behavior. For studies that list more than one set of parameters, we enumerate the experiments. For example, Marek and Svobodoba [75] Experiment #3 uses the parameters ([MA], $[BrO_3^-]$, $[Ce(III)]_{mf}$, $[H_2SO_4]$) = (0.032, 0.01, $2.0 \cdot 10^{-4}$, 1.5).

For a particular set of experimental parameters, we are careful to distinguish the following scenarios: i) the model replicates the experimentally observed behavior reported in the study, ii) the model replicates experimentally observed behavior from other studies, and iii) the model does not exhibit any chemically relevant complex behavior, viz. any behavior other than steady state or relaxation oscillations. The check marks in Table 4.6 reflect case i) where the model replicates the experimentally observed behavior reported in the study.

4.5.1 Observed behavior at experimental parameters

In this subsection, we discuss individual studies at whose parameter values Model D exhibits behavior matching experimentally observed behavior.

Texas Experiments, 1981–1989

Györgyi and Field [53] compared the trajectories of their models to experimental work. We do not recount all their specific findings here, but the main findings are that Model D_{QSS} replicates low flow rate complexity observed in the Texas experiments [114, 99, 86, 87], while Model D_{EQ} replicates the high flow complexity observed by Hudson, Hart, and Marinko [62]. It should be noted that parameters used for comparison by Györgyi and Field at the low flow rates are taken directly from experiments. However, when comparing Model D_{EQ} to ex-

Experiment	[MA]	$[BrO_3^-]$	$10^3\cdot$ [cat]	$[H_2SO_4]$	Temp (°C)	Observed Phenomena	EQ	QSS
[110, 111]	0.5	0.09	0.8 (C,M)	1.5	25	DC-MMOs	✓	
[75]	0.032	0.5	1.0	1.5	25	ROs		
	0.032	0.01	1.0	1.5	40	ROs		
	0.032	0.01	0.2	1.5	40	MMO	✓	
	0.066	0.025	0.2	1.5	40	DC-MMOs	✓	
[40, 62, 63, 56]	0.3	0.14	1.0	0.2	25	HFPAS, HC	✓	
[40, 103]	0.3	0.14	0.125 (F)	0.2	25	HFPAS, HC		
[119]	0.24	0.108	0.75	1.44	39	PAS		
[98]	0.08	0.036	0.25	1.44	40	Strange attractor		✓
[114, 107, 100, 99]	0.25	0.14	0.83	0.2	28.3	LFPAS		✓
[61]	0.056	0.039	0.025	0.05	25	Detailed (LF)PAS		
[76]	0.0813	0.0275	0.416 (M)	1.5	25	MMOs	✓	
[77]	0.018	0.0275	0.416 (M)	1.5	28	MMOs		
	0.3	0.0275	0.416 (M)	1.5	28	DC-MMOs	✓	
	0.056	0.033	0.416 (M)	1.5	28	MP-MMOs	✓	
	0.049	0.033	0.416 (M)	1.5	28	1^1-2^2 MMOs	✓	
	0.081	0.028	0.416 (M)	1.5	28	3^3 MMO	✓	
	0.3	0.028	0.416 (M)	1.5	28	6^6 MMO	✓	
[92]	0.25	0.1	1.7	0.2	27	LFPAS, crisis		
[21, 104]	0.25	0.1	0.83	0.2	28	LFPAS, mult.		✓
[1]	0.2	$6.5\cdot10^{-3}$	0.5	1.5	43	HB		✓
	0.525	0.036	0.25	0.75	43	QP	✓	
	0.5	0.036	0.25	0.75	40	Fractal torus	✓	
	0.15	0.075	0.5	1.0	43	HFPAS	✓	✓
	0.1	0.01	0.5	1.5	43	HFPAS		
[5]	0.3	0.1	0.25	0.4	25	HFPAS, Type-III inter.		✓
[64]	0.3	0.14	1.0	0.23	21	(LF,HF)PAS, QP	✓	
[104]	0.3	0.087	1.0	0.37	25	HFPAS	✓	

Table 4.6: Experimental parameters and observed phenomenon for many BZ experiments. Table 4.2 lists the conversion of $[H_2SO_4]$ to $[H^+]$ concentration. The catalyst is assumed to be Cerium (C), unless otherwise noted: F and M indicate ferroin and manganese. Key: PAS – periodic-aperiodic sequences (HF – high flow, LF – low flow), HC – homoclinicity, MMO – mixed-mode oscillations (MP – mixed-parent type, DC – double composite), QP - quasiperiodicity, HB – Hopf bifurcation, mult. – mulitiplicity, and inter. – intermittency. Check marks indicate whether or not Model D replicates the experimentally observed behavior.

perimental high flow rate data, only the MA and Ce(III) feed concentrations are taken from high flow rate studies [62]. The other two experimental parameters, the BrO_3^- feed concentration and the H_2SO_4 concentration, may have been altered to fit the Texas high flow rate data. However, all parameter values used in

the numerical study [53] are well within experimentally relevant ranges.

Marek and Svobodoba, 1975

Sørenson first observed complex BZ dynamics in a CSTR [110, 111]. These double composite MMOs were later rediscovered by Marek and Svobodoba [75] and Masełko and Swinney [76], among others. The experimental parameter values used in these experiments can be found in Table 4.6.

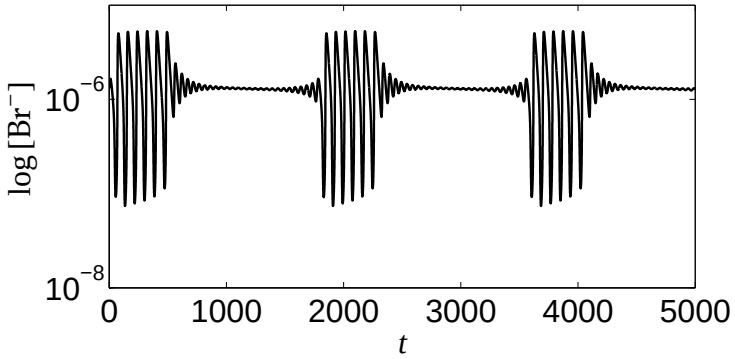

(a) $k_f = 8.6 \cdot 10^{-4}$

Figure 4.10: An MMO generated by Model D_{EQ} at $k_f = 8.6 \cdot 10^{-4}$ for ([MA], $[BrO_3^-]$, $[Ce(III)]_{mf}$, $[H_2SO_4]$) = (0.066, 0.018, $2 \cdot 10^{-4}$, 1.5).

Figure 2 of Reference [75] shows a double composite MMO with a $4^{11}3^{10}$ segment for the experimental parameters ([MA], $[BrO_3^-]$, $[Ce(III)]_{mf}$, $[H_2SO_4]$) = (0.066, 0.025, $2 \cdot 10^{-4}$, 1.5) at a flow rate of $k_f = 6.94 \cdot 10^{-4}$. At these precise parameter values, Model D_{EQ} does not exhibit any complex oscillations. However, if the $[BrO_3^-]$ feed concentration is decreased, qualitatively similar MMOs with trains of large oscillations are found. Figure 4.10 shows an MMO computed at ([MA], $[BrO_3^-]$, $[Ce(III)]_{mf}$, $[H_2SO_4]$) = (0.066, 0.018, $2 \cdot 10^{-4}$, 1.5) and $k_f = 8.6 \cdot 10^{-4}$. The duration of the SAOs, is highly sensitive to $[BrO_3^-]$ in this regime. It increases as $[BrO_3^-]$ is increased. For [MA] = 0.066 M and flow rates comparable to the

experiment, complex oscillations disappear near $[BrO_3^-] = 0.02$ M. Figure 4.10 shows that if we use $[BrO_3^-] = 0.018$ M, we find spiking similar to the experimentally observed behavior. The numerical flow rate is in good agreement with the experimental flow rate; the two flow rates differ by roughly 20%.

Masełko and Swinney, 1985–1986

In their impressive studies of Farey sequences in the BZ reaction, Masełko and Swinney [76, 77] presented many experimental trajectories. These include MMOs similar to the double composite MMOs of Sørenson [111], MMOs of mixed parent type, and bistability of MMOs. Model D_{EQ} is able to replicate each of these behaviors; though we find bistability of MMOs at different parameter values. There are basic quantitative differences between experimentally observed time series and those exhibited by the models. For instance the experimental double composite MMOs tend to have fewer SAOs than those exhibited numerically. Masełko and Swinney [77] also produced very complicated MMOs, such as a $2^2 2^1 (1^1)^4$. We do not detect MMOs of this complexity in Model D. We find that the model may not be as dynamically rich as the reaction itself. However, the qualitative similarity of trajectories at these parameter values is quite remarkable.

Masełko and Swinney [76, 77] reported double composite MMOs for two distinct parameter values. In [76], they report a 7^4 MMO for a residence time of 5.2 min ($k_f \approx 3.21 \cdot 10^{-3}$) and parameter values ([MA], $[BrO_3^-]$, [Mn], $[H_2SO_4]$) = (0.0813, 0.0275, $4.16 \cdot 10^{-4}$, 1.5). Using Model D_{EQ} at these same parameters and at a flow rate of $k_f = 1.98 \cdot 10^{-3}$, we find a 7^{13} MMO, which is shown in Figure 4.11(a). This MMO spends nearly equal amounts of time in the SAOs and

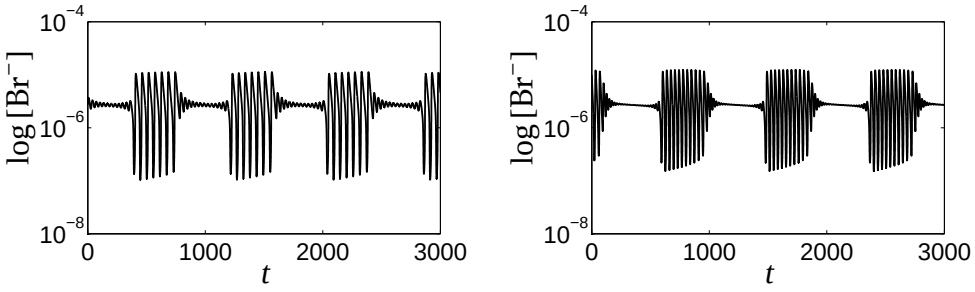

(a) $k_f = 1.98 \cdot 10^{-3}$ (b) $k_f = 1.24 \cdot 10^{-3}$

Figure 4.11: MMOs calculated at the Masełko and Swinney [76] parameter values: (a) $k_f = 1.98 \cdot 10^{-3}$ at Reference [76] parameter values. (b) $k_f = 1.24 \cdot 10^{-3}$ at Reference [77] Experiment #2 parameter values. See Table 4.6 for values.

LAOs. This is not true of the experimental time series, which spends less time in the SAOs. We make no attempt to vary other parameters to better fit the experimental data. The numerical and experimental flow rates are of the same order of magnitude and differ by less than 40%. However, because these reactions are catalyzed with Manganese, direct comparison between the simulations and the experimental behavior is not possible.

In [77], Masełko and Swinney presented another MMO: a 5^6 MMO at the parameters ([MA], $[BrO_3^-]$, [Mn], $[H_2SO_4]$) = (0.3, 0.0275, $4.16 \cdot 10^{-4}$, 1.5) for a residence time of 8.0 min ($k_f \approx 2.08 \cdot 10^{-3}$). The experimentally observed trajectory spends approximately equal time in SAOs and LAOs. At these parameter values, Model D_{EQ} also exhibits a double composite MMO. Figure 4.11(b) shows that at flow rate $k_f = 1.24 \cdot 10^{-3}$, the SAO and LAO regimes share equal time. Although the exact pattern of small and large oscillations do not agree, Model D_{EQ} exhibits qualitatively similar behavior to the experimentally observed oscillations. Again, the flow rates used experimentally and numerically are comparable.

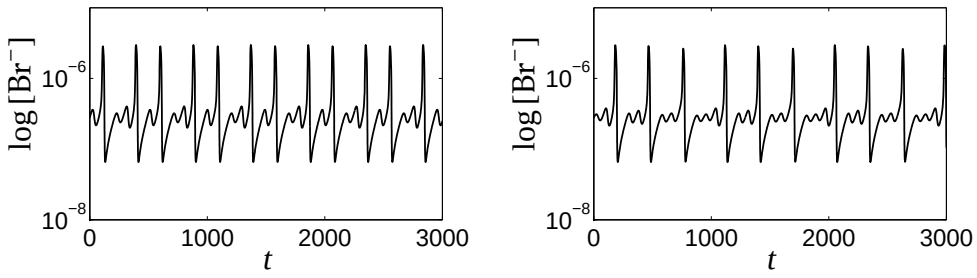

(a) $k_f = 5.89 \cdot 10^{-3}$ (b) $k_f = 5.92 \cdot 10^{-3}$

Figure 4.12: Mixed parent type MMOs at $k_f = 5.89 \cdot 10^{-3}$ and $k_f = 5.92 \cdot 10^{-3}$ for [77] Experiment #3 parameter values. Consult Table 4.6 for parameter values.

Masełko and Swinney [77] also presented a series of complex MMOs with multiple parent types, such as a $(2^3 2^2)^2 (1^1)^2 1^2$ MMO that occurs at the Experiment #3 parameter values ([MA], [BrO_3^-], [Mn], [H_2SO_4]) = (0.056, 0.033, $4.16 \cdot 10^{-4}$, 1.5) for a residence time of 435 s ($k_f \approx 2.30 \cdot 10^{-3}$). Using these parameter values, we find MMOs of two-parent type. Specifically, at $k_f = 5.89 \cdot 10^{-3}$ we find a $1^1 1^2$ MMO and at $k_f = 5.92 \cdot 10^{-3}$ we find a $(1^2)^2 1^3$ MMO. While the richness and complexity of the MMOs is not reproduced at these parameter values, the qualitative nature of the simulated trajectories is similar to those observed experimentally.

Hourai et. al. [61] only observed hourglass-shaped MMOs in studies that use low concentrations for all mixed-feeds. While complicated oscillations are not supported by either Model D_{EQ} or D_{QSS} at the experimental concentrations found in [61], the replication of the Marek and Svobodoba and Masełko and Swinney experiments show that Model D can support complex oscillations at low concentrations of MA and BrO_3^-. We predict that complex oscillations can be found in Model D for parameter values near those of [61]; however, no further exploration of parameter space is attempted in this work.

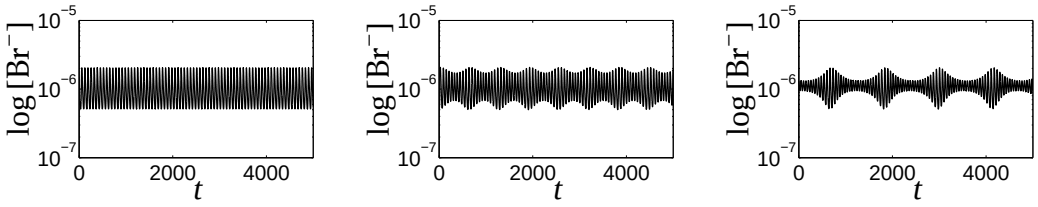

(a) $k_f = 4.55 \cdot 10^{-4}$ (b) $k_f = 4.30 \cdot 10^{-4}$ (c) $k_f = 4.0 \cdot 10^{-4}$

Figure 4.13: Quasiperiodic solutions of Model D_{EQ} for several flow rates using parameter values from [1] Experiment #2.

Argoul and coworkers, 1985–1987

Argoul et. al. [2, 1] performed a series of impressive experiments designed to track invariant tori in the BZ reaction. From these studies, we consider two sets of parameter values. However, Argoul et. al. used a variation of the typical experimental setup: the sulfuric acid concentration of the mixed-feeds differ. For the first set of parameters we consider, the medium for both the BrO_3^- and Ce(III) feeds is a sulfuric acid solution of H_2SO_4 = 0.75 M, but the medium for the MA feed is H_2SO_4 = 1.5 M. This is true for each of the five experiments in the study [1]; the three mixed feeds have two different sulfuric acid solutions. This experimental setup cannot be represented in Model D, because the proton concentration $[H^+]$ is directly proportional to the sulfuric acid concentration and is assumed to be constant. For simulations, we assume that all feeds have the same sulfuric acid concentration and we choose the majority value. For this experiment, we use H_2SO_4 = 0.75 M.

The first set of parameters are taken from Experiment #2: ([MA], $[BrO_3^-]$, $[Ce(III)]_{mf}$, $[H_2SO_4]$) = $(0.525, 0.036, 2.5 \cdot 10^{-4}, 0.75)$. Experimentally, Argoul et. al. detect a torus by observing quasiperiodic trajectories as the flow rate increases from a regime of relaxation oscillations. As the flow rate increased

further, the time between trains of large oscillations grows, and an asymmetry in the SAOs begins to develop. Before the breakup of the torus, the time between trains of large amplitude oscillations grows. The SAOs form an asymmetry where the inside of the torus appears "pinched" after the LAOs, and the envelope of the SAOs is a thin tube. The amplitude of the SAOs grows slowly before the next train of LAOs.

In Model D_{EQ}, we find the opposite sequence; a torus forms as the flow rate decreases from the regime of relaxation oscillations. Figure 4.13 shows three numerical simulations for the Experiment #2 parameter values. As the flow rate is decreased from the P_1 relaxation oscillation regime, the system undergoes a torus bifurcation. As the flow rate is decreased further, the time between large oscillations grows. The quasiperiodicity observed in the numerical trajectories are symmetric; no asymmetry develops.

Unfortunately, all flow rates are given in units of mL/min and the reactor size used in this experiment is not specified. We are unable to precisely compare the experimental flow rates to the numerical flow rates. However, Table 1 in Reference [1] lists the residence times for this experiment as 0.33 hours – 0.6 hours. Figure 4.13 shows that a torus is observed at a flow rate of $4.3 \cdot 10^{-4}$, which corresponds to a residence time of 0.64 hours, so the numerical residence times are comparable to those of the experiments.

In addition to quasiperioicity, Argoul et. al. also observed a sequence of MMOs at the Experiment #4 parameter set. At $k_f = 0.40$ mL/min, they observed a chaotic trajectory which concatenates 1^0 and 1^1 segments, although the segment 4^1 shows up three times. Even at higher flow rates, the number of observable SAOs is small. Time series for a 3^1 and 2^1 MMOs are shown, as well

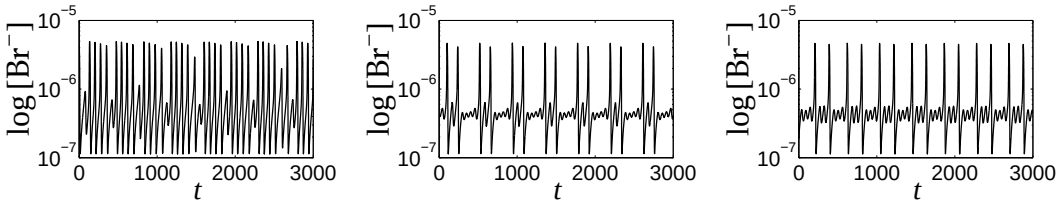

(a) $k_f = 4.8106 \cdot 10^{-3}$ (b) $k_f = 5.001 \cdot 10^{-3}$ (c) $k_f = 5.001 \cdot 10^{-3}$

Figure 4.14: MMOs of Model D_{EQ} at the [1] Experiment #4 parameters: (a) A chaotic MMO at $k_f = 4.8106 \cdot 10^{-3}$. (b)–(c) Bistability of MMOs at $k_f = 5.001 \cdot 10^{-3}$.

as a nearly homoclinic orbit. No small amplitude oscillations were reported for higher flow rates, possibly indicating that a subcritical Hopf bifurcation occurred.

At the Experiment #4 parameter set, Model D_{EQ} also exhibits a sequence of periodic and aperiodic time series. Figure 4.14(a) shows a chaotic orbit that concatenates 4^1 and 5^1 segments. This is quite similar to the time series shown in Figure 13(b) of [1]. As the flow rate is increased, Model D_{EQ} exhibits more MMOs, although the number of SAOs generated in the model is greater than those observed experimentally. At $k_f = 5.001 \cdot 10^{-3}$, we find an instance of bistability of MMOs at $k_f = 5.001 \cdot 10^{-3}$. Figure 4.14(b) and (c) show a $1^1 1^4$ and a $1^2 1^3$ MMO, respectively. No evidence of experimental bistability was reported at these parameters. This is also the first documented evidence of bistability of MMOs in Model D. Initial conditions for the two time series are given by $([HBrO_2], [Br^-][Ce(III)]_{mf}, [BrMA]) =$

$$\begin{cases} (1.336548 \cdot 10^{-5}, 1.734646 \cdot 10^{-7}, 3.492293 \cdot 10^{-4}, 1.098493 \cdot 10^{-3}) \text{ for Figure 4.14}(b), \\ (1.619353 \cdot 10^{-5}, 1.390882 \cdot 10^{-7}, 3.532030 \cdot 10^{-4}, 1.092514 \cdot 10^{-3}) \text{ for Figure 4.14}(c). \end{cases}$$

Unlike the experiments, small amplitude periodic orbits are found at high flow rates before the systems returns to steady state.

4.5.2 Experimental behaviors observed at other parameters

In this subsection, we describe experimentally observed behaviors that are replicated by Model D, but whose parameter values do not match experimental parameters. In the classification system described above, this falls under category ii).

Roux and coworkers, 1980

In the previous subsection, we described the experiments of Argoul et. al. [1] tracking the evolution of a torus en route to break-up. Using the [1] Experiment #2 parameters, Model D_{EQ} exhibits a torus. Figure 4.13 shows that the torus is very symmetric, although the experimental torus formed is not symmetric. However, if we use the parameter values found in Roux et. al. [98], Model D_{EQ} exhibits a torus whose oscillations are asymmetric (see Table 4.6 for parameter values). At these experimental values, Roux and coworkers find a strange attractor that concatenates large amplitude periodic orbits and 1^1 MMO segments. This is not found in Model D_{EQ}. Figure 4.15 shows three quasiperiodic time series for the flow rates $k_f \in \{1.44 \cdot 10^{-4}, 1.41 \cdot 10^{-4}, 1.35 \cdot 10^{-4}\}$. Panel (a) shows a relaxation oscillation at $k_f = 1.44 \cdot 10^{-4}$. As the flow rate is decreased, we observe the formation of a torus whose SAOs have an asymmetric pattern. The asymmetry is clear for the time series at $k_f = 1.41 \cdot 10^{-4}$ shown in Figure 4.15(b). Finally, at $k_f = 1.35 \cdot 10^{-4}$, the amplitude of the SAOs decreases rapidly and the envelope forms a thin tube. At comparable flow rates, Roux and coworkers find a strange attractor that concatenates 1^0 and 1^1 MMO segments.

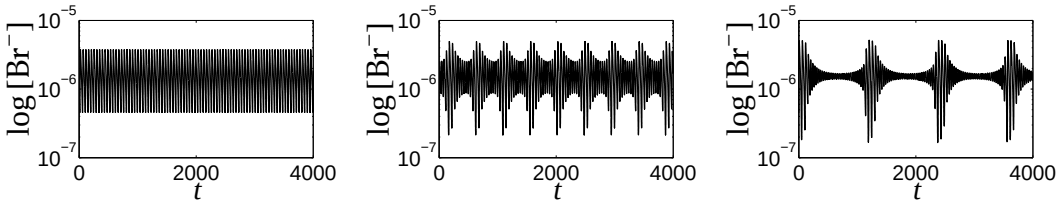

(a) $k_f = 1.44 \cdot 10^{-4}$ (b) $k_f = 1.41 \cdot 10^{-4}$ (c) $k_f = 1.35 \cdot 10^{-4}$

Figure 4.15: Quasiperiodic solutions of Model D_{EQ} for several flow rates using parameter values from [98]. The asymmetric patterns observed in the time series are similar to those observed experimentally in [1].

Masełko and Swinney, 1985–1986

In their careful study of MMOs and Farey sequences [77], Masełko and Swinney show a 1^3 MMO at the parameter values given in Table 4.6 for Experiment #1. The profile of the SAOs of the 1^3 MMO have an hourglass shape, much like the MMOs in section 4 observed at low flow rate parameters. At these parameter values, Model D_{EQ} exhibits double composite MMOs similar to those observed by Sørenson [111]. Figure 4.16(a) shows a typical MMO for Experiment #1 parameters at $k_f = 3.94 \cdot 10^{-3}$.

However, the system is very sensitive to the bromate concentration. Figure 4.16(b) shows that by increasing the bromate to $[BrO_3^-] = 0.035$, the criticality of the initial Hopf bifurcation is changed, and a small stable periodic orbit is born. This periodic orbit is unaffected by other regions of phase space. As a result, the small periodic orbit grows into relaxation oscillations without bifurcating and producing MMOs. It is possible that varying parameters other than $[BrO_3^-]$ may produce qualitatively similar MMOs, however, we do not attempt these computations.

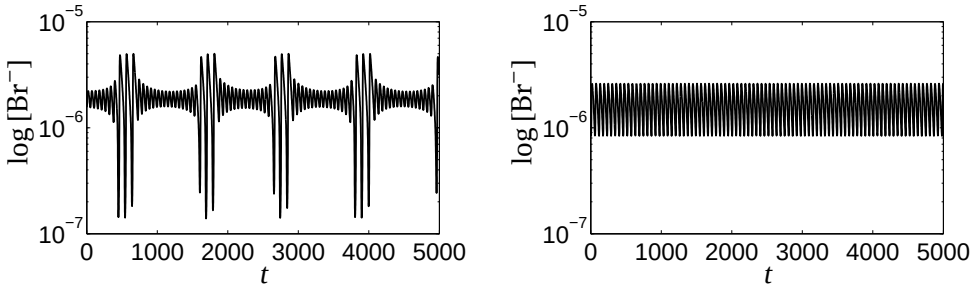

(a) $k_f = 3.94 \cdot 10^{-3}$, $[BrO_3^-] = 0.0275$ (b) $k_f = 4.6 \cdot 10^{-3}$, $[BrO_3^-] = 0.035$

Figure 4.16: (a) Low flow rate MMOs at [77] Experiment #1 parameter values for $k_f = 3.94 \cdot 10^{-3}$. (b) Periodic orbit at $k_f = 4.6 \cdot 10^{-3}$ for the same parameter values as (a), except we change $[BrO_3^-] = 0.035$.

4.5.3 Shortcomings of Model D

Texas low flow rates, 1981–1987

Györgyi and Field noted in [53] that the EQ model replicates low flow rate complexity well. For the low flow parameter rates from section 4 [114], a family of stable periodic orbits is born at a Hopf bifurcation at $k_f = 5.97540 \cdot 10^{-4}$. As the flow rate increases, the small periodic orbits grow into relaxation oscillations. The periodic orbits undergo no bifurcation until the high flow rate complexity regime. The bifurcation sequences at exhibited by Model D_{EQ} at high flow rates match those observed experimentally.

Figure 4.17 shows two periodic orbits in phase space for $k_f \in \{7.0 \cdot 10^{-4}, 8.0 \cdot 10^{-4}\}$. The family of equilibria of the layer equation (4.3, $\alpha = 0$) is shown in cyan. A Hopf bifurcation of the fast subsystem is indicated by a red cross. The black cross denotes the equilibrium point of the full system. Unlike the low flow rate dynamics of Model D_{QSS}, there is very little change in the BrMA concentration at large excursions. This causes the trajectory to pass by the critical manifold

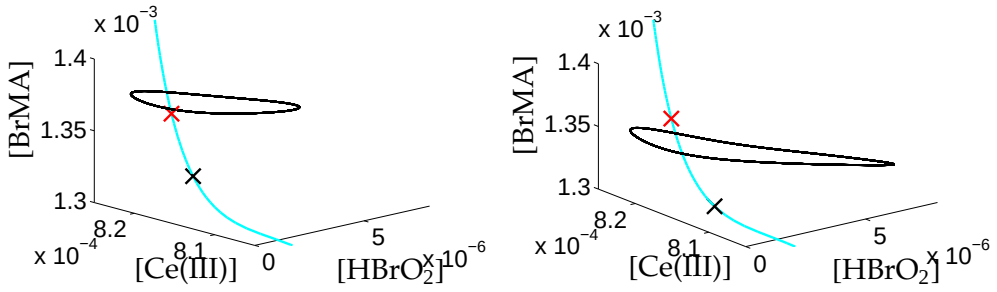

(a) $k_f = 7.0 \cdot 10^{-4}$ (b) $k_f = 8.0 \cdot 10^{-4}$

Figure 4.17: Trajectories of Model D_{EQ} at [114] parameters for two flow rates. No MMOs are observed in this regime.

near the dynamic Hopf point, where the real parts of the transverse eigenvalues are small. As a result, the periodic orbits do not become attracted to the critical manifold, and SAOs are not initiated. The periodic orbit does not interact with the critical manifold in any significant way at low flow rates. This does not replicate the low flow rate complexity of the Texas experiments.

Argoul and coworkers, 1985–1987

The last set of experimental parameters we discuss is Experiment #1 by Argoul et. al. [1]. They detect a supercritical Hopf bifurcation and carefully check that the period and frequency of the periodic orbit scales according to mathematical theory [47]. However, at these parameter values in Model D_{QSS}, trajectories whose SAOs have an asymmetric hourglass shape are detected: the extent of the increasing amplitude oscillations in phase space is much larger than extent of the decreasing amplitude oscillations. Figure 4.18(a) shows the time series for the QSS model at [1] experiment #1 parameters and $k_f = 4.0 \cdot 10^{-5}$. The amount of time spent during increasing amplitude oscillations is about an order of magnitude larger than the time spent during decreasing amplitude oscillations. This

makes the time series appear as though the SAOs have a "wedge" shape.

To begin the investigation of this trajectory, we compute the local separation of time scales, given by the eigenvalues of the variational equation at the point $(4.056713 \cdot 10^{-8}, 1.515076 \cdot 10^{-7}, 4.996578 \cdot 10^{-4}, 1.10 \cdot 10^{-3})$ to be $(-0.499288, 0.030978 \pm 0.059259i, -8.648 \cdot 10^{-5})$. The smallest eigenvalue is approximately three orders of magnitude smaller than the middle eigenvalues, indicating that there is a significant separation of time scales in this region of phase space, justifying our calculation of the critical manifold $(4.3, \alpha = 0)$. Figure 4.18(b) shows the trajectory in phase space, along with the critical manifold, shown in cyan. A Hopf bifurcation of the layer equation is also detected and indicated by a red cross.

The point at which the variational equation was calculated was chosen because it lies on the critical manifold near the initiation of the SAOs. We note that the real part of the complex eigenvalue is positive. This indicates that the equilibria of the layer equation is repelling, and that a nearby trajectory would be repelled away. However, the time series clearly shows the amplitudes of the SAOs decreasing before increasing. This behavior may be associated with an invariant torus. However, the behavior of the full system may not compatible with the behavior of the approximate fast subsystem. This is particularly troubling given the large separation of time scales in this region. However, to the author's knowledge, experimental time series resembling these trajectories have not been observed in chemical systems. Not only is the period of the oscillation much larger than what is typically observed in the BZ reaction, but the flow rates at which this behavior is observed are also quite low.

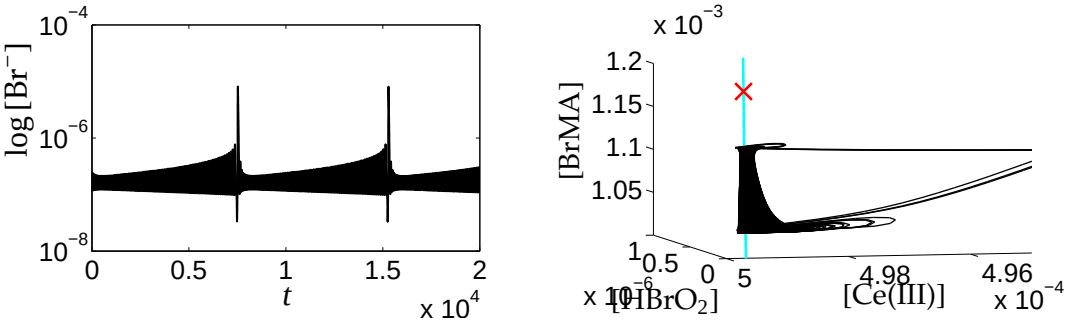

(a) $k_f = 4.0 \cdot 10^{-5}$ (b) $k_f = 4.0 \cdot 10^{-5}$

Figure 4.18: Model D_{QSS} exhibits wedgelike trains of SAOs at [1] Experiment #1 parameter values. (a) Time series at $k_f = 4.0 \cdot 10^{-5}$. (b) The same trajectory in phase space.

Vidal and coworkers, 1980

Some of the most peculiar experimental time series come from the study [119]. Vidal et. al. studied the periodic and aperiodic time series in what they referred to as the "transition to turbulence." Many of the periodic time series shown in the paper appear to have a slow modulation of amplitudes. This leads us to believe that the system may be experiencing periodic forcing. The peristaltic pumping mechanism may introduce small pulsing effects on the flow rate, although other studies [62] use the same mechanism and determine that the pulsing effect on the dynamics is minimal. However, to the author's knowledge, no other experimental study has reported these modulated time series.

4.6 Future Work

In this chapter, we examine the behavior of Model D using GSPT as a framework for mathematical analysis. We also discuss many of the behaviors exhibited by Model D at experimental parameters. This work can be extended via several

avenues, including further experimentation to test the predictability of Model D, examining the validity of the approximations made in the reduction of Model C to Model D, and extending the bifurcation analysis of Model D in parameter space.

4.6.1 Relating Model D to experiments

Further experiments can be performed to test Model D's ability to reproduce experimental behavior. We suggest two studies involving the low flow rate and high flow rate parameter values discussed in Section 3. In their studies, Turner et. al. [114] and Hudson, Hart, and Marinko [62] study only low flow rate and high flow rate behaviors, respectively. These studies are particularly important in the study of Model D because Model D replicates the behavior exhibited by the reaction at these experimental parameters. We propose that these experiments be extended to study both low and high flow rates for these two sets of parameters using Model D to make predictions about the flow rate complexity not investigated in the original study. Experimental control has improved greatly since both of the experiments were performed, and new predictions can be made about the expected behavior of the reaction in the flow rate regimes that were studied in [114, 62]. Because the behavior of Model D_{EQ} and D_{QSS} at the same parameters is not identical, detailed experiments may reveal which model best represents the reaction at these parameter values.

Turner et. al. [114] observed the alternation of periodic and aperiodic behavior at low flow rates at the parameter values $([MA], [BrO_3^-], [Ce(III)]_{mf}, [H_2SO_4]) = (0.25, 0.1, 0.83 \cdot 10^{-3}, 0.2)$. Turner et. al. found 1^n MMOs for $n \leq 5$ and pos-

sibly greater (an interval of periodicity and aperiodicity is reported for lower flow rates, but n is not given). At low flow rates, both Model D_{EQ} and Model D_{QSS} predict the bistability of MMOs and invariant tori, at $k_f = 1.387 \cdot 10^{-4}$ and $k_f = 5.437 \cdot 10^{-4}$, respectively. In the models, a family of periodic orbits born from a Hopf bifurcation undergoes a torus bifurcation to form an invariant torus. This occurs after the first MMOs are detected. No tori are reported in [114]. The bistability of tori and MMOs may be detected experimentally by passing through the low flow rate regime with both increasing and decreasing flow rates, while using a sufficiently small flow rate resolution.

At high flow rates and the above parameter values, the behavior of each model differs. Model D_{EQ} forms 1^n MMOs for $n = 1, 2$, and 3. For flow rates $k_f \geq 1.03 \cdot 10^{-3}$, the amplitudes of some of the SAOs of the 1^n MMOs become negligible. As the flow rate increases, MMOs are no longer observed and the system exhibits small periodic orbits until it reaches steady state at a supercritical Hopf bifurcation near $k_f = 1.073 \cdot 10^{-3}$. As the flow rate is decreased from this steady state, a family of stable periodic orbits is born. This family eventually exhibits a PD bifurcation and loses stability quickly. There is a region of bistability for $k_f \in [1.045 \cdot 10^{-3}, 1.050 \cdot 10^{-3}]$ where stable small periodic orbits and 1^n MMOs coexist.

Model D_{QSS} exhibits this same basic pattern of behavior, including the bistability of periodic orbits near the flow rate branch of equilibria. However, as the flow rate increases from the P_1 regime of relaxation oscillations, the shape of the high flow rate MMOs differs significantly. Figure 4.19 shows the difference between the two models at high flow rates. Figure 4.19(a) shows the SAOs of Model D_{EQ} at $k_f = 1.01 \cdot 10^{-3}$, while Figure 4.19(b) shows the segment of the 1^n

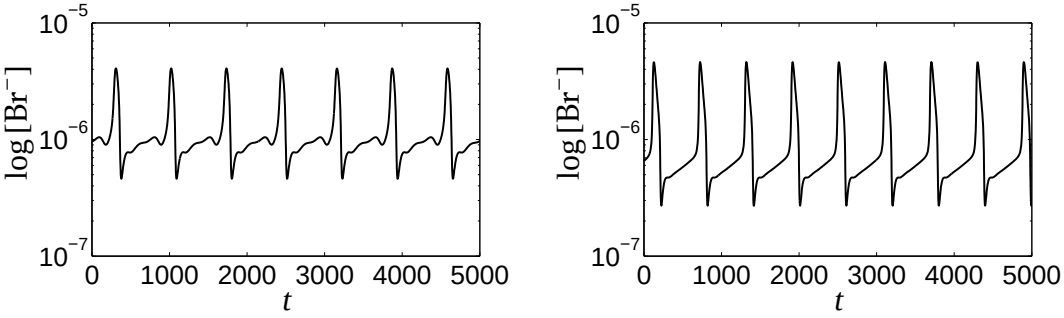

(a) $k_f = 1.01 \cdot 10^{-3}$ (b) $k_f = 8.6 \cdot 10^{-4}$

Figure 4.19: Model D at high flow rates using low flow rate parameters. (a) Model D_{EQ} at $k_f = 1.01 \cdot 10^{-3}$. (b) Model D_{QSS} at $k_f = 8.6 \cdot 10^{-4}$.

MMO between large spikes at $k_f = 8.6 \cdot 10^{-4}$ appears monotone. This is true for many 1^n MMOs at high flow rates, and indicates a strong contraction the equilibria of the fast subsystem. The shape of experimental SAOs observed at these parameter values will indicate if either model replicates the experimental behavior.

Ibison and Scott [64] investigated the behavior of the reaction using parameter values very similar to the study of Hudson, Hart, and Marinko study [62], which investigated the high flow rate regime. The differences between the two sets of parameters are the $[H_2SO_4]$ concentration and the temperature: Ibison and Scott used $([H_2SO_4], T) = (0.23, 21^\circ\,\mathrm{C})$, while Hudson et. al. used $([H_2SO_4], T) = (0.20, 25^\circ\,\mathrm{C})$. Ibison and Scott reported similar periodic and aperiodic time series at high flow rates with one major exception: they also recorded 1^n MMOs for very large n. The time between the large spikes of these oscillations were up to ten residence times, making the determination of whether or not the time series was periodic difficult. These trajectories are not reported in the original Hudson, Hart, and Marinko study [62]. Györgyi et. al. [56] reproduced the work of Hudson, Hart, and Marinko and also did not report these

trajectories.

At low flow rates, Ibison and Scott [64] find large parameter intervals of chaotic behavior. These results stand in contrast to the low flow rate studies of Turner et. al. [114] and Hourai et. al. [61], among others. Ibison and Scott report intermittency between large spikes and 1^1 segments as the flow rate is decreased from the P_1 regime of relaxation oscillations. They do not report any periodic MMOs and only report small periodic orbits before a Hopf bifurcation brings the system to steady state at the lowest flow rates. We emphasize that although the difference in the $[H_2SO_4]$ concentration is small, the difference in the temperature may be significant. However, this difference is not represented in the GF family.

At the parameter values $([MA], [BrO_3^-], [Ce(III)]_{mf}, [H_2SO_4]) = (0.3, 0.14, 1.0 \cdot 10^{-3}, 0.2)$, both Models D_{EQ} and D_{QSS} exhibit quasiperiodicity at low flow rates. This behavior is not reported by Ibison and Scott [64]. At low flow rates, Model D_{EQ} simultaneously exhibits a family of small periodic orbits and MMOs. The family of stable periodic orbits, born at a supercritical Hopf bifurcation at $k_f = 6.66 \cdot 10^{-4}$ bifurcates to form a torus near $k_f = 7.04 \cdot 10^{-4}$. The torus bifurcates back to a family of periodic orbits near $k_f = 7.214 \cdot 10^{-4}$ which grow in amplitude into relaxation oscillations. Near $k_f = 7.15 \cdot 10^{-4}$, a 1^4 MMO is the first MMO observed. MMOs of 1^n type are observed for $k_f \in [7.15 \cdot 10^{-4}, 7.384 \cdot 10^{-4}]$. This type of behavior could be detected experimentally by scanning the low flow rate complexity with both increasing and decreasing flow rates.

Model D_{QSS} forms a torus near $k_f = 2.17 \cdot 10^{-4}$. This torus exists simultaneously with trajectories exhibiting intermittency between 1^n MMOs. Figure 4.20 shows a time series of Model D_{QSS} exhibiting intermittency between a 1^8 MMO

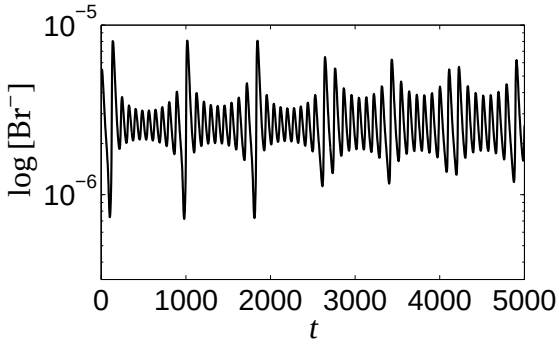

(a) $k_f = 2.20 \cdot 10^{-4}$

Figure 4.20: Intermittency of quasiperiodicity and 1^n MMOs of Model D_{QSS} at $k_f = 2.2 \cdot 10^{-4}$.

and a torus. This leads to chaotic behavior in this regime. After the breakup of the torus, the typical alternation of periodic and aperiodic 1^n MMOs occurs for decreasing n until the system enters the P_1 regime.

4.6.2 Approximations of Model D

Model D_{EQ} and D_{QSS} are derived by using either the equilibrium or quasi steady state assumption on the species $BrO_2\cdot$ in Model C, given by (4.1) and (4.2). Two evaluations of this approximation are possible by comparing the numerical approximation of Model D to first Model C and then to the experimental $BrO_2\cdot$ concentration. The former comparison is straightforward; compare the concentration of $BrO_2\cdot$ in Model C to the two approximations in Model D.

Direct comparison between the Model D approximations and the experimental concentration of $BrO_2\cdot$ is impossible because the species is not measured in BZ experiments. Therefore, an indirect method of comparison using Model C can be used. The validity of the approximations can be determined by finding

sets of experimental parameters whose behavior is replicated by Model C, and determining if either Model D_{EQ} or Model D_{QSS} replicate the behavior. If the behavior is replicated by both Model C and either Model D_{EQ} or Model D_{QSS}, we assume that the approximation is valid at these parameter values. However, neither of these comparisons yields any quantitative information about the experimental [$BrO_2\cdot$] concentration.

4.6.3 Bifurcation structure of Model D

This work is intended to be the beginning of a full investigation into the four-dimensional parameter space. Such an investigation will involve the computation of bifurcation diagrams with two or more parameters fixed. A recent study of the unfolding of the singular Hopf bifurcation by Guckenheimer and Meerkamp [48] constructed three-dimensional bifurcation diagrams by gluing together two-dimensional diagrams. While computationally expensive, this method provides a great deal of insight into the possible sequences of bifurcations that occur in the system. We can compute similar bifurcation diagrams by identifying the flow rate as the main bifurcation parameter and the bromate and Cerium feed concentrations as secondary parameters. In chapter 2, we showed that one-dimensional induced maps computed near a singular Hopf bifurcation can provide both quantitative and qualitative information about the bifurcation structure of a system. Using symbolic dynamics, we showed which individual orbits were permissible in the autocatalator. Given the evidence for singular Hopf bifurcation presented above, this method may be useful in the analysis of Model D.

Furthermore, the studies of Maselłko and Swinney [76, 77] and Argoul et. al. [1] presented very detailed bifurcation sequences of both invariant tori and MMOs. Specifically, Masełko and Swinney studied the evolution and breakup of invariant tori. They showed that the breakup of the torus was preceded by the wrinkling of the torus. We showed above that invariant tori exist in Model D and can also coexist with MMOs. We did not investigate the behavior associated with the breakup of the invariant tori in Model D, and we did not check whether the tori become wrinkled. Argoul et. al. presented time series showing highly complex MMOs. We identify MMOs of two-parent type, but do not observe three-parent type MMOs. Given Model D's ability to replicate experimental behavior, we predict that trajectories of this type can be found using a more extensive search of parameter space.

BIBLIOGRAPHY

[1] F. Argoul, A. Arneodo, P. Richetti, and J.-C. Roux. From quasiperiodicity to chaos in the Belousov-Zhabotinskii reaction. I. Experiment. *J. Chem. Phys.* Vol. 86, No. 6. 3325–3338. 1987.

[2] F. Argoul and J.-C. Roux. Quasiperiodicity in chemistry: An experimental path in the neighbourhood of a codimension-two bifurcation. *Phys. Lett. A* Vol. 108A, No. 8, pp. 426–430. 1985.

[3] P. Ashwin, J. Buescu and I. Stewart. Bubbling of attractors and synchronisation of chaotic oscillators. Phys. Lett. A 193(2): 126–139, 1994.

[4] S.M. Baer, T. Erneux. Singular Hopf bifurcation to relaxation oscillations. *SIAM J. App. Math.*, 46(5):721–739, 1986.

[5] G. Baier, K. Wegmann, and H.L. Hudson. An intermittent type of chaos in the Belousov-Zhabotinsky reaction. *Phys. Lett. A.* Vol. 141, No. 7, pp. 340–345. 1989.

[6] K. Bar-Eli and R.M. Noyes. Computations simulation experimental observations of complex bursting patterns in the Belousov-Zhabotinskii system. *J. Chem. Phys.* Vol. 88, No. 6, pp. 3646–3654. 1988.

[7] D. Barkley. Slow manifolds and mixed-mode oscillations in the BelousovZhabotinskii reaction. *J. Chem. Phys.* Vol. 89, No. 9, pp. 5547–5559. 1988.

[8] D. Barkley, J. Ringland, and J.S. Turner. Observations of a torus in a model of the Belousov-Zhabotinskii reaction. *J. Chem. Phys.* Vol. 87, No. 7. pp. 3812–3820. 1987.

[9] B.P. Belousov. In *Sb. Ref. Radiat. Med.*. Medgiz, Moscow. pp. 145. 1958.

[10] B. P. Belousov. *Oscillations and Traveling Waves in Chemical Systems*, pages 605–613. Wiley-Interscience, New York, 1985.

[11] M. Benedicks, L. Carleson. The dynamics of the Hnon map. Ann. of Math. (2) 133 (1991), no. 1, 73–169.

[12] E. Benoít , J.-L. Callot, F. Diener, and M. Diener. Chasse au canards. *Collect. Math.*, 31:37119, 1981.

[13] É Benoît. Canards et enlacements. *Inst. Hautes tudes Sci. Publ. Math.* No. 72 (1990).

[14] W.A. Beyer, R.D. Mauldin, and P.R. Stein. Shift-Maximal Sequences in Function Iteration: Existence, Uniqueness, and Multiplicity. *J. Math. Anal. Appl.* Vol. 115, pp. 305–362. 1986.

[15] K. Bold. C. Edwards, J. Guckenheimer, S. Guharay, K. Hoffman, J. Hubbard, R. Oliva, W. Weckesser. The forced van der Pol equation II: Canards in the reduced system. SIAM J. App. Dyn. Sys. 2(4):570–608. 2003

[16] B. Braaksma. Singular hopf bifurcation in systems with fast and slow variables. *J. Nonlinear Sci.*, 8(5):457–490, 1998.

[17] W. C. Bray. A periodic reaction in homogeneous solution and its realation to catalysis. *J. Am. Chem. Soc.*, 1921, 43 (6), pp. 1262–1267.

[18] M. Brøns, T. J. Kaper, and H. G. Rotstein. Introduction to Focus Issue: Mixed Mode Oscillations: Experiment, Computation, and Analysis. *Chaos*, (015101), 2008.

[19] M. Brøns, M. Krupa, and M. Wechselberger. Mixed mode oscillations due to the generalized canard phenomenon. *Fields Institute Communications*, 49:39–63, 2006.

[20] M. Cartwright, J. Littlewood. The equation $\ddot{y} - kf(y,\dot{y})\dot{y} + g(y,k) = p(t) = p_1(t) + kp_2(t)$, $k > 0$, $f(y) \geq 1$. *Ann. of Math.* 2(48):472–494. 1947.

[21] K.G. Coffman, W.D.McCormick, Z. Noszticzius, R.H. Simoyi, and H.L. Swinney. Universality, multiplicity, and the effect of iron impurities in the Belousov-Zhabotinskii reaction. *J. Chem. Phys.* Vol. 86, No. 1, pp. 119–129. 1987.

[22] P. De Kepper and K. Bar-Eli. Dynamical properties of the Belousov-Zhabotinskii reaction in a flow system. Theoretical and experimental analysis *J. Phys. Chem.* Vol. 87, pp. 480–488. 1983.

[23] Welington de Melo, Sebastian van Strien. *One-dimensional dynamics*, volume 25 of *Ergebnisse der Mathematik und ihrer Grenzgebiete (3) [Results in Mathematics and Related Areas (3)]*. Springer-Verlag, Berlin, 1993.

[24] M. Desroches, B. Krauskopf, and H. Osinga The geometry of mixed-mode

oscillations in the Olsen model for the Peroxidase-Oxidase reaction. *Disc. and Cont. Dyn. Sys.* 2:807–827, 2009.

[25] M. Desroches, J. Guckenheimer, B. Krauskopf, C. Kuehn, H. Osinga, and M. Wechselberger, Mixed-mode oscillations with multiple time scales. *To appear.* SIAM Review, 2011.

[26] E.J. Doedel, R.C. Paffenroth, A.R. Champneys, T.F. Fairgrieve, Yu.A. Kuznetsov, B.E. Oldeman, B. Sandstede, and X.J. Wang. AUTO: Software for continuation and bifurcation problems in ordinary differential equations, Auto07p, v.0.6, available online at http://indy.cs.concordia.ca/auto/.

[27] W. Eckhaus. Relaxation oscillations including a standard chase on french ducks. *Lecture Notes in Mathematics*, 985:449–494, 1983.

[28] J. Farey *Philos. Mag. J.* London. No. 47, pp. 385. 1816.

[29] N. Fenichel. Geometric singular perturbation theory for ordinary differential equations. *J. Diff. Eq*, 31:53–98, 1979.

[30] R.J. Field. Limit cycle oscillations in the reversible Oregonator. *J. Chem. Phys.* Vol. 63, No. 6. pp. 2289–2296, 1975.

[31] R.J. Field. In *Oscillations and travelling waves in chemical systems.* Edited by R.J. Field and M. Burger. Wiley, New York. pp. 55. 1985.

[32] R.J. Field. Personal communication. 2010–11.

[33] R.J. Field and H.D. Försterling. On the oxybromine chemistry rate constants with Cerium ion in the Field-Körös-Noyes mechanism of the Belousov-Zhabotinskii reaction: the equilibrium $HBrO_2 + BrO_3^- + H^+ \leftrightharpoons 2BrO_2^{\cdot} + H_2O$. *J. Phys. Chem.* Vol. 90, pp. 5400–5407. 1986.

[34] R.J. Field, E. Körös and R.M. Noyes. Oscillations in Chemical Systems. II. Thorough analysis of temporal oscillation in the Bromate–Cerium–Malong Acid system. *J. Am. Chem. Soc.* Vol. 94, No. 25, 8649–8664. 1972.

[35] R.J. Field and R.M. Noyes. Oscillation in chemical systems. IV. Limit cycle behavior in a model of a real chemical reaction. *J. Chem. Phys.* Vol. 60, No. 5, pp. 1877–1884. 1974.

[36] A.M. Fraser and H.L. Swinney. Independent coordinates for strange attractors from mutual information. *Phys. Rev. A.* Vol. 33, pp. 1134. 1986.

[37] N. Ganapathisubramanian and R.M. Noyes. A discrepancy between experimental and computational evidence for chemical chaos. *J. Chem. Phys.* Vol. 76, No. 4, pp 1770–1774. 1982.

[38] P. Gaspard and G. Nicolis. What can we learn from homoclinic orbits in chaotic dynamics? *J. Stat. Phys.* Vol. 31, No. 3, pp. 499–518. 1983.

[39] W. Govaerts, Y.A. Kuznetsov. Matcont.

[40] K.R. Graziani, J.L. Hudson, and R.A. Schmitz. The Belousov-Zhabotinskii reaction in a continuous flow reactor. *Chem. Eng. J.* Vol. 12, pp. 9–21. 1976.

[41] C. Grebogi, E. Ott and J.A. Yorke. Chaotic Attractors in Crisis. *Phys. Rev. Lett.*, 48:1507–1510, 1982.

[42] J. Guckenheimer. Bifurcations of dynamical systems. In *Dynamical Systems*, number 8 in Progress in Mathematics. C.I.M.E. Lectures, Birkhäuser, 1978.

[43] J. Guckenheimer. Singular Hopf bifurcation in systems with two slow variables. *SIAM J. Appl. Dyn. Syst.*, 7(4):1355–1377, October 2008.

[44] J. Guckenheimer. Return maps of folded nodes and folded saddle-nodes. *Chaos*, 18, 2008.

[45] J. Guckenheimer, R. Haiduc. Canards at folded nodes. *Moscow Math. J.*, 5(1):91–103, 2005.

[46] J. Guckenheimer, K. Hoffman, W. Weckesser. The forced van der Pol equation I: The slow flow and its bifurcations. *SIAM J. App. Dyn. Sys.* 2(1):1–35, 2003

[47] J. Guckenheimer, P. Holmes. *Nonlinear oscillations, dynamical systems, and bifurcations of vector fields.* Number 42 in Applied Mathematical Sciences Series, Springer, Berlin, 1983.

[48] J. Guckenheimer, P. Meerkamp. *Unfoldings of singular Hopf bifurcation. Submitted. SIAM J. Appl. Dyn. Sys.* 2011.

[49] J. Guckenheimer and C. Scheper. A geometric model for mixed-mode oscillation in a chemical system. *SIAM J. Appl. Dyn. Sys.* 10:91–128, 2011.

[50] J. Guckenheimer, John; M. Wechselberger, L-S. Young. Chaotic attractors of relaxation oscillators. Nonlinearity 19 (2006), no. 3, 701–720.

[51] J. Guckenheimer and A.R. Willms. Asymptotic analysis of subcritical Hopf-homoclinic bifurcation. *Physica D.* 139:195–216, 2000.

[52] I. Gucwa, P. Szmolyan. Geometric singular perturbation analysis of an autocatalator model. *Disc. and Cont. Dyn. Syst., Ser. S.*, 4:783–806, September 2008.

[53] L. Györgyi and R.J. Field. Simple Models of Deterministic Chaos in the Belousov-Zhabotinsky Reaction. *J. Phys. Chem.* Vol. 95, pp. 6594–6602. 1991.

[54] L. Györgyi and R.J. Field. Modeling and interpretation of chaos in the Belousov-Zhabotinsky reaction. In *Chaos in Chemistry and Biochemistry.* Eds. L. Györgyi and R.J. Field. pp. 47–85. 1993.

[55] L. Györgyi, S. Rempe, and R.J. Field. A novel model for the simulation of chaos in low-flow-rate CSTR experiments with the Belousov-Zhabotinskii reaction: a chemical mechanism for two-frequency oscillations. *J. Phys. Chem.* 95:3159–3165, 1991.

[56] L. Györgyi, R.J. Field, Z. Noszticzius, W.D. McCormick, and H.L. Swinney. Confirmation of high flow rate chaos in the Belousov-Zhabotinsky reaction. *J. Phys. Chem.* Vol. 96, pp. 1228–1233. 1992.

[57] L. Gyögyi, T. Turányi, and R.J. Field. Mechanistic Details of the Oscillatory Belousov-Zhabotinskii Reaction. *J. Phys. Chem.* Vol. 94, pp. 7162–7170. 1990.

[58] R. Haiduc. Horseshoes in the forced van der Pol system. *Nonlinearity.* 22:213–237. 2009.

[59] E. Hairer, G. Wanner. *Solving Ordinary Differential Equations II: Stiff and Differential-Algebraic Problems.*, Number 14 in Springer Series in Computational Mathematics Springer, Berlin, 1993.

[60] B.-L. Hao Elementary Symbolic Dynamics and Chaos in Dissipative Systems. World Scientific, Singapore, 1989.

[61] M. Hourai, Y. Kotake, and K. Kuwata. Experimental Evidence of chatotic states in the BZ reaction. *J. Phys. Chem.* Vol. 89, pp. 1760–1764. 1985.

[62] J.L. Hudson, M. Hart, and D. Marinko. An experimental study of multiple peak periodic and nonperiodic oscillations in the BZ reaction. *J. Chem. Phys.* Vol. 71, No. 4, pp. 1601–1606. 1979.

[63] J.L. Hudson and J.C. Mankin Chaos in the BZ reaction. *J. Chem. Phys.* Vol. 74, No. 11, pp. 6171–6177. 1981.

[64] P. Ibison and S.K. Scott. Detailed Bifurcation Structure and New Mixed-mode Oscillations of the Belousov-Zhabotinskii Reaction in a Stirred Flow Reactor. *J. Chem. Soc. Faraday Trans.* Vol. 86, No. 22. pp. 3695–3700. 1990.

[65] P. Ibison and S.K. Scott. Phenomenological study of a new flow model of the Belousov-Zhabotinskii reaction. *J. Chem. Soc. Faraday Trans.* Vol. 87, No. 2, pp. 223–228. 1991.

[66] R.D. Janz, D.J. Vanecek, and R.J. Field. Composite double oscillation in a modified version of the oregonator model of the Belousov-Zhabotinskii reaction. *J. Chem. Phys.* Vol. 73, No. 3, pp. 3132–3138. 1980.

[67] C.K.R.T. Jones. Geometric singular perturbation theory. In *Dynamical Systems*, number 1609 in Springer Lecture Notes in Math., pages 44–120. Springer-Verlag, New York, 1995.

[68] M. Krupa, N. Popovic, and N. Kopell. Mixed-mode oscillations in three time-scale systems: A prototypical example. *SIAM J. Applied Dynamical Systems*, 7(2), 2008.

[69] M. Krupa and P. Szmolyan. Extending slow manifolds near transcritical and pitchfork singularities. *Nonlinearity*. Vol. 14, pp. 1473–1491, 2001.

[70] R. Larter, C.G. Steinmetz. Chaos via mixed-mode oscillations. *Phil. Trans. R. Soc. Lond. A*, 337:291–298, 1991.

[71] R. Larter, C.G. Steinmetz, and Aguda. Fast-slow variable analysis of the transition to mixed-mode oscillations and chaos in the peroxidase reaction. *J. Chem. Phys.*, 89(10):6506–6514, 1988.

[72] D. Lindberg, J.S. Turner, and D. Barkley. Chaos in the Showalter-Noyes-

Bar-Eli model of the Belousov-Zhabotinskii reaction. *J. Chem. Phys.* Vol. 95, No. 5. pp. 3238–3239. 1990.

[73] J.E. Littlewood On non-linear differential equations of the second order. III. The equation $\ddot{y}-k(1-y^2)\dot{y}+y = bk\cos(t+\alpha)$ for large k, and its generalizations. *Acta Math.* 97: 267–308, 1957.

[74] M. Marek. Modelling of Patterns in space and time. Lecture Notes in Biomathematics, Vol. 55, pp. 214. Springer-Verlag, Berlin. 1984.

[75] M. Marek and E. Svobodova. Nonlinear phenomena in oscillatory systems of homogeneous reactions – experimental observations. *Biophys. Chem.* Vol. 3, pp. 263–273. 1975.

[76] J. Masełko and H.L. Swinney A complex transition sequence in the Belousov-Zhabotinskii reaction. *Physica Scripta.* Vol. T9, pp. 35–39. 1985.

[77] J. Masełko and H.L. Swinney. Complex periodic oscillation and Farey arithmetic in the BZ reaction. *J. Chem. Phys.* Vol. 85, No. 11, pp. 6430–6441. 1986.

[78] N. Metropolis, M.L. Stein, and P.R. Stein. On finite limit sets for transformations on the unit interval. *J. Comb. Alg.* A15, pp. 25–44. 1973.

[79] A. Milik, P. Szmolyan, H. Loeffelmann, and E. Groeller. Geometry of mixed-mode oscillations in the 3d autocatalator. *Int. J. of Bifurcation and Chaos*, 8:505–519, 1998.

[80] A. Milik, P. Szmolyan. *Multiple time scales and canards in a chemical oscillator*, in Multiple Time-Scale Dynamical Systems, C.K.R.T Johnes and A. Khibnik, eds. IMA Vol. Math. Appl. 122. Springer, New York, 2001. pp 117–140.

[81] J. Milnor, W. Thurston. *On iterated maps of the interval*, pages 465–563. Number 1342 in Dynamical Systems, Lecture Notes in Mathematics. Springer, Berlin, 1988.

[82] E. F. Mishchenko, N. K. Rozov. Di?erential Equations with Small Parameters and Relaxation Oscil lations (translated from Russian). Plenum Press, 1980.

[83] A.I. Neishtadt. On delayed stability loss under dynamic bifurcations I. *Diff. Equ.* 23:2060–2067, 1987.

[84] A.I. Neishtadt. On delayed stability loss under dynamic bifurcations II. *Diff. Equ.* 24:226–233, 1988.

[85] A.I. Neishtadt. On stability loss delay for dynamical bifurcations. *Disc. and Cont. Dyn. Sys.* 2:897–909, 2009.

[86] Z. Noszticzius, W.D. McCormick, and H.L. Swinney. Effect of Trace Impurities on a bifurcation structure in the Belousov-Zhabotinsky reaction and preparation of high-purity malonic acid. *J. Phys. Chem.* 91:5129–5134, 1987.

[87] Z. Noszticzius, W.D. McCormick, and H.L. Swinney. Use of bifurcation diagrams as fingerprints of chemical mechanisms. *J. Phys. Chem.* 93:2796–2800, 1989.

[88] V. Petrov, S. Scott, and K. Showalter. Mixed-mode oscillations in chemical systems. *J. Chem. Phys.*, 97(9):6191–6198, November 1992.

[89] Y. Pomeau and P. Manneville. Intermittent transition to turbulence in dissipative dynamical systems. *Commun. Math. Phys*. Vol. 74, pp. 189–197. 1980.

[90] Y. Pomeau, J.-C. Roux, A. Rossi, S. Bachelart, and C. Vidal. Intermittent behaviour in the Belousov-Zhabotinsky reaction. *J. Physique Lett. A.* Vol. 77. pp. 391. 1981.

[91] P. Richetti and A. Arneodo. The periodic-chaotic sequences in chemical reactions: A scenario close to homoclinic conditions? *Phys. Lett. A.* Vol. 109A, No. 8. pp. 359–366. 1985.

[92] P. Richetti, P. De Kepper, J.-C. Roux, and H.L. Swinney. A crisis in the Belousov-Zhabotinskii reaction: experiment and simulation. *J. Stat. Phys.* Vol. 48, No. 5/6. pp. 977–990. 1987.

[93] P. Richetti, J.-C. Roux, F. Argoul, and A. Arneodo. From quasiperiodicity to chaos in the Belousov-Zhabotinskii reaction. II. Modeling and theory. *J. Chem. Phys.* Vol. 86, No. 6. 3339–3356. 1987.

[94] J. Ringland, N. Issa, and M. Schell. From U sequence to Farey sequence: A unification of one-parameter scenarios. *Phys. Rev. A.* Vol. 41, No. 8, pp. 4223–4235. 1990.

[95] E.B. Robertson and H.B. Dunford. The State of the Proton in Aqueous Sulfuric Acid. *J. Am. Chem. Soc.* Vol. 86, pp. 5080–5089. 1964.

[96] O.E. Rössler. Chaos in abtract kinetics: two prototypes. *Bull. Math. Biol.* Vol. 39, pp. 275–289. 1977.

[97] H.G. Rotstein, M. Wechselberger, and N. Kopell. Canard induced mixed-mode oscillations in a medial entorhinal cortex layer II stellate cell model. *SIAM J. Applied Dynamical Systems*, 7(4):1582–1611, 2008.

[98] J.-C. Roux, A. Rossi, S. Bachelart, and C. Vidal. Representation of a strange attractor from an experimental study of chemical turbulence. *Phys. Lett. A.* Vol. 77A, No. 6, pp. 391–393. 1980.

[99] J.-C. Roux, R.H. Simoyi, and H.L. Swinney. Observation of a strange attractor. *Physica D.* Vol. 8, pp. 257–266. North-Holland Publishing Company. 1982.

[100] J.-C. Roux, J.S. Turner, W.D. McCormick, and H.L. Swinney. Experimental observations of complex dynamics in a chemical reaction. In *Nonlinear problems: present and future.* (eds. A.R. Bishop, D.K. Campbell, and B. Nicolaenko) North-Holland, Amsterdam, 1982.

[101] P. Ruoff and R.M. Noyes. An amplified oregonator model simulating alternative excitabilities, transitions In types of oscillations, and temporary bistablllty In a closed system. *J. Chem. Phys.* Vol. 84, No. 3, pp. 1413–1423. 1986.

[102] S. Schmidt and P. Ortoleva. Electric field effects on propagating BZ waves: Predictions of an Oregonator and new pulse supporting models. *J. Chem. Phys.* Vol. 74, No. 8, pp. 4488–4500. 1980.

[103] R.A. Schmitz, K.R. Graziani, and J.L. Hudson. Experimental Evidence of chaotic states in the Belousov-Zhabotinskii reaction. *J. Chem. Phys.* Vol. 67, No. 7, pp. 3040–44. 1977.

[104] F.W. Schneider and A.F. Münster. Chemical oscillations, chaos, and fluctuations in flow reactors. *J. Phys. Chem.* Vol. 95, pp. 2130–2138. 1991.

[105] S.K. Scott. Chemical Chaos. Vol. 24 in *International Series of Monographs on Chemistry.* Clarendon Press, Oxford, UK. 1991.

[106] K. Showalter, R.M. Noyes, and K. Bar-Eli. A modified Oregonator model exhibiting complicated limit cycle behavior in a flow system. *J. Chem. Phys.* Vol. 69, No. 6, pp. 2514–2524. 1978.

[107] R.H. Simoyi, A. Wolf, and H.L. Swinney. One-dimensional dynamics in a multicomponent chemical reaction. *Phys. Rev. Lett.* Vol. 49, No. 4. pp. 245–248. 1982.

[108] S. Smale Differentiable dynamical systems. *Bull. Amer. Math. Soc.* 73: 747–817, 1967.

[109] P. Szmolyan, M. Wechselberger. Canards in $\mathbb{R}^3$. *J. Diff. Eq.*, 177:419–453, 2001.

[110] P.G. Sørenson. Comment. *Faraday Symp. Chem. Soc.* Vol. 9:88, 1974.

[111] P.G. Sørenson. Experimental investigations of behavior and stability properties of attractors corresponding to burst phenomena in the open Belousov reaction. *Ann. New York Acad. Sci*. Vol. 316, pp. 667. 1979.

[112] F. Takens. Detecting strange attractors in turbulence. In *Lecture Notes in Mathematics.* Vol. 898, pp. 361–388. 1980.

[113] K. Tomita, A. Akira, and T. Ohta. Simplified model for Belousov-Zhabotinsky reaction. *J. Theor. Biol.* Vol. 68, pp. 459–481. 1977.

[114] J.S. Turner, J.-C. Roux, W.D. McCormick, and H.L. Swinney. Alternating periodic and chaotic regimes in a chemical reaction – experiment and theory. *Phys. Lett.* Vol. 85A, No. 1. pp. 9–12. 1981.

[115] J.J. Tyson. Oscillations, bistability and echo wave in models of the Belousov-Zhabotinskii reaction. *Ann. New York Acad. Sci*. Vol. 316, pp. 279. 1979.

[116] J.J. Tyson. Scaling and reduclng the Field-Köros-Noyes mechanism of the Belousov-Zhabotinskii reaction. *J. Phys. Chem.* Vol. 86, pp. 3006–3012. 1982.

[117] J.J. Tyson. In *Oscillations and travelling waves in chemical systems.* Edited by R.J. Field and M. Burger. Wiley, New York. pp. 93. 1985.

[118] B. van der Pol. The nonlinear theory of electric oscillations. *Proc. IRE*, 22:1051–1086, 1934.

[119] C. Vidal, J.-C. Roux, S. Bachelart, and A. Rossi. Experimental study of the transition to turbulence in the Belousov-Zhabotinskii reaction. *Ann. New York Acad. Sci*. Vol. 357, pp. 377. 1980.

[120] G. Wallet. Entrée-sorite dans un tourbillon. *Ann. Inst. Fourier (Grenoble)*, 36: 157–184, 1986.

[121] Q. Wang, L-S. Young. Toward a theory of rank one attractors. *Ann. of Math.* (2) 167 (2008), no. 2, 349–480.

[122] M. Wechselberger. Existence and bifurcation of canards in $\mathbb{R}^3$ in the case of a folded node. *SIAM J. Appl. Dyn. Syst.*, 4(1):101–139, February 2005.

[123] M. Wechselberger, W. Weckesser. Homoclinic clusters and chaos associated with a folded node in a stellate cell model. *Disc. and Cont. Dyn. Sys., Ser. S.*, 2(4):829–850, December 2009.

[124] A.M. Zhabotinsky. *Biofizika.* Vol 9, pp. 306. 1964.

[125] A.M. Zhabotinskii. *Oscillations and Traveling Waves in Chemical Systems*, pages 1–6. Wiley-Interscience, New York, 1985.

[126] D. Zhang, L. Györgyi, and W.R. Peltier. Deterministic chaos in the Belousov-Zhabotinsky reaction: Experiments and simulations. *Chaos.* Vol. 3, No. 4, pp. 723–745. 1993.